Vegetated dunes and barchan dune fields

Orencio Durán

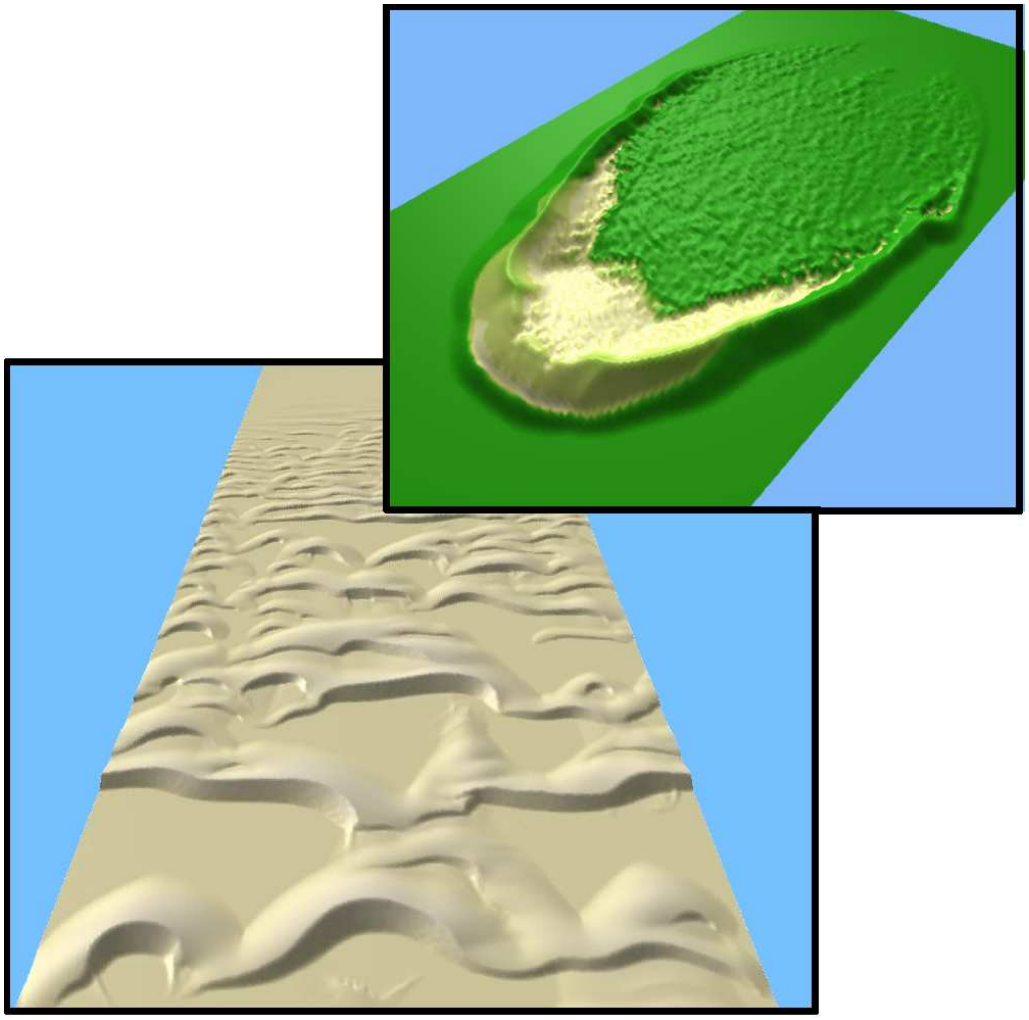

Vegetated dunes and barchan dune fields

Von der Fakultät Mathematik und Physik der Universität Stuttgart
zur Erlangung der Würde eines Doktors der
Naturwissenschaften (Dr. rer. nat.) genehmigte Abhandlung

vorgelegt von

Orencio Durán

aus Manzanillo, Cuba

Hauptberichter:	Prof. Dr. H. J. Herrmann
Mitberichter:	Prof. Dr. M. Fähnle
Tag der mündlichen Prüfung:	29. January 2007

Institut für Computerphysik der Universität Stuttgart

2006

Contents

Deutsche Zusammenfassung

Der Transport von Sand, verursacht durch effektive Erosion und Deposition, kann zur Bildung von Oberflächenstrukturen auf verschiedenen Skalen führen. Diese Strukturen formen ein hierarchisches System von drei Niveaus von äolischen Gebilden, die sich überlagern. Windrippel erscheinen auf der Zentimeterskala, während sich einfache Dünen auf Längenskalen von einzelnen bis zu hunderten von Metern entwickeln und sich manchmal zu Dünenverbänden, sog. *Draas*, überlagern, mit einer Größenordnung von Kilometern.

Barkan–Dünen kommen häufig vor, wenn der Wind unidirektional ist, und es nicht genügend Sand gibt, die Oberfläche vollständig zu bedecken. Diese hochmobile Dünenform tritt zwar als einzelne Düne auf, kann aber kilometerlange Dünenfelder mit der Struktur eines Korridors in Windrichtung bilden. Barkane repräsentieren die einzigen stabilen Sandgebilde, die bei einfachen Windbedingungen auftreten, d.h. bei unidirektionalem Wind. Damit sind sie das ideale Objekt, um zu untersuchen, in welcher Weise sich die kollektive Bewegung von Millionen von Sandkörnern auf festem Grund mit solch einer beeindruckenden Struktur organisiert.

Diese Dissertation konzentriert sich auf die Lösung von drei Hauptfragestellungen, die mit Barkanen zu tun haben. Erstens werden die phänomenologischen Parameter eines Modells zum Transport von Sand auf der Längenskala von Sandkörnern anhand von Windtunnel–Experimenten bestimmt. Dies geschieht in Abhängigkeit des grundlegenden Flusses und der Eigenschaften der Sandkörner (Durán and Herrmann, 2006a). Dieses Modell bildet den Kernstück des Dünenmodells, das wir benutzen werden. Es ist nicht nur wichtig, um die Präzision der Vorhersagen des Gesamtmodells zu verbessern, sondern auch, um das Gesamtmodell in geeigneter Weise zu erweitern. Damit können z.B. auch äußere Bedingungen simuliert werden, unter welchen Dünen unter Wasser oder auf dem Mars und der Venus enstehen (Parteli et al., 2006). Die zweite Fragestellung besteht darin, die Faktoren zu erforschen, die die Verteilung der Größen und der Entfernungen zwischen den Dünen in einem Dünenfeld verursachen (Duran et al., 2005; Durán et al., 2006a; Durán et al., 2006b). Dies ist von großer Bedeutung, da die Dünengrößen und ihre Dichte in einem Feld die zwei wichtigsten Größen darstellen. Somit wird es erleichtert, eine geeignete Strategie zu entwerfen, um Dünen zu demobilisieren. In der dritten Fragestellung werden die Prozesse untersucht, die zur Stabilisierung einer Düne führen können. Diese können dabei helfen, die Verwüstung von Landstrichen zu stoppen oder zu vermeiden (Durán and Herrmann, 2006b). Auf welche Weise werden Barkan–Dünen von Vegetation deaktiviert? Welche Faktoren bestimmen die Bedingungen, die diese durch Pflanzen verursachte Deaktivierung initiieren?

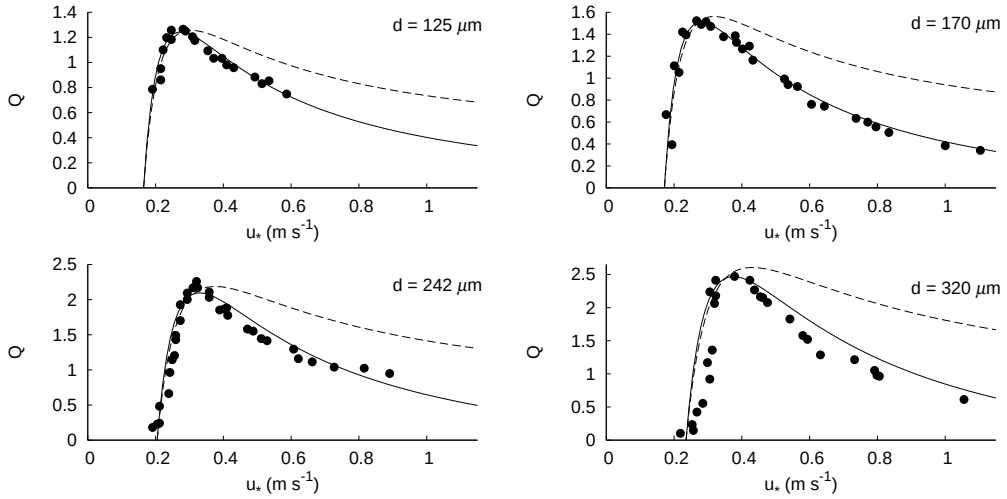

Abbildung 1: Dimensionsloser saturierter Fluss $Q \equiv q_s(u_*)/(q_t(u_*/u_{*t})^3)$ als Funktion der Schergeschwindigkeit u_* für verschiedene Durchmesser, berechnet aus Windtunnel–Experimenten (Punkte). Modell des saturierten Flusses mit (durchgezogene Linien) und ohne (gestrichelte Linie) der Annahme einer effektiven Höhe. In allen Fällen ergibt das Modell mit einer effektiven Höhe bessere Resultate.

Kapitel 1: Auf der Sandkorn– und Dünenskala

In diesem Kapitel wird eine neue Gleichung vorgeschlagen, die den saturierten Sandfluss als eine Funktion der Scherspannung des Windes beschreibt. Dies geschieht durch die Einführung eines Windprofils, welches den Feedback–Effekt der Saltation der Sandkörner und einen Ausdruck für die Rauheitslänge berücksichtigt, der die Saltationsschicht mit einbezieht. Diese Gleichung für den Sandfluss wird durch Windtunnel–Experimente bestätigt (Abb. 1). Spezielle Fälle dieser Gleichung ergeben Transportgleichungen, die von der Relation zwischen den zwei charakteristischen Längen des Modells abhängen: die Höhe des gestörten Windprofils und die Höhe, auf der der Winddruck den Impuls ersetzt, der durch die Wechselwirkungen zwischen fliegenden Sandkörnern und dem Grund verloren geht.

Zusätzlich wurden zum ersten Mal die phänomenologischen Parameter des Modells zum Sandtransport bestimmt, indem deren Skalenverhältnisse mit der Dichte und der Viskosität des Fluids, der Gravitationsbeschleunigung und dem Korndurchmesser verwendet wurden. Einige dieser Parameter konnten durch Windtunnel–Experimente bestätigt werden (Durán and Herrmann, 2006a). Diese Abhängigkeiten sind notwendig, um die Modellierung von Dünen unter verschiedenen physikalischen Bedingungen, wie z.B. in der Marsatmosphäre oder unter Wasser, zu ermöglichen. Dies konnte durch die erfolgreiche Anwendung des Dünenmodells auf das Skalierungsproblem von Marsdünen (Parteli et al., 2006) bestätigt werden. Das Modell ist natürlich auch dazu geeignet, um z.B. den Effekt der Sandkorngröße auf die Morphologie von normalen Dünen zu studieren.

Die hier bisher vorgestellten Arbeiten werden benutzt, um ein Gesamtmodell zur Modellierung von Dünen zu vervollständigen, das wir im Folgenden DUNE–Modell nennen

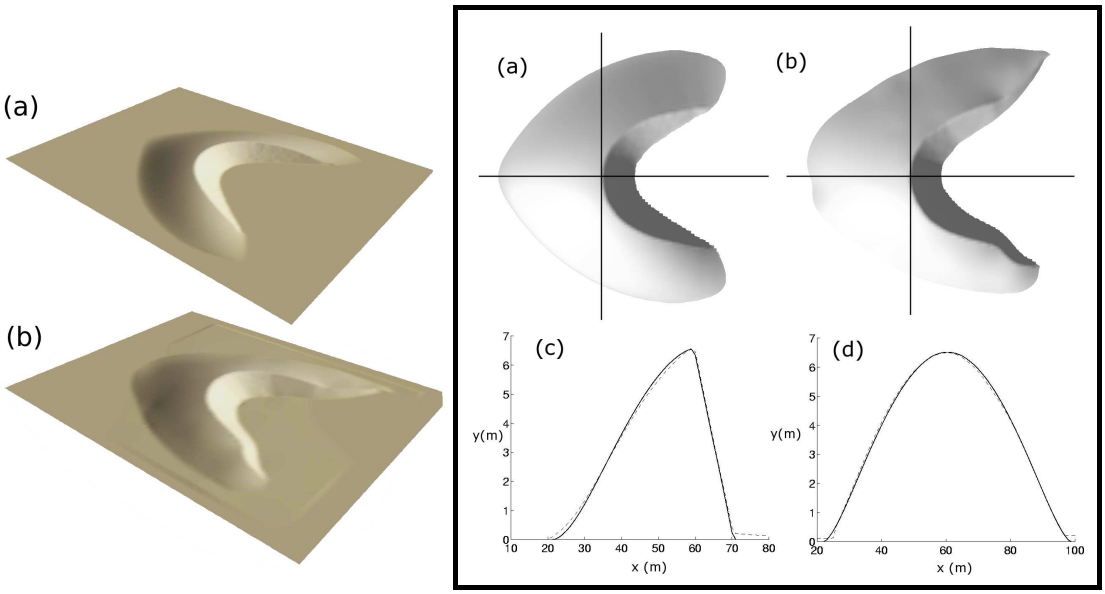

Abbildung 2: Vergleich einer sechs Meter hohen Barkane (a: Simulation, b: Messung). Die mittigen Längs– und Querschnitte beider Dünen werden in (c) und (d) verglichen. Dabei stellt die durchgezogene Linie die simulierte Düne und die gestrichelte Linie die gemessene dar. Beide Dünen sind von gleicher Größenordnung.

werden. Die Modellierung von Sanddünen bringt die Aufteilung in drei Hauptteile mit sich: (i) die Berechnung des Einflusses der Topographie auf die Windströmung, (ii) die Berechnung des Sandflusses in Abhängigkeit des gestörten Winds, und (iii) die Entwicklung der Sandoberfläche durch Erosion, Deposition und Lawinen.

Das Studium von Barkan–Dünen erfolgt durch numerische Simulationen. Es werden mehrere Skalengesetze vorgestellt, unter anderem zwischen dem Volumen, der Geschwindigkeit und der Bilanz des Sandflusses einer Barkane. Der Vergleich dieser Gesetze mit Daten aus Messungen ermöglicht das Bestätigen der Ergebnisse des neuen DUNE–Modells, das das neue Sandtransport–Modell und seine Parameter enthält. Abb. 2 vergleicht die charakteristische dreidimensionale “C”–Form einer simulierten und einer in Marokko gemessenen Düne. Beide Dünen ähneln sich sehr mit Ausnahme der Hörner.

Eines der erhaltenen Gesetze, das eine lineare Abhängigkeit zwischen Zustrom und Ausfluss des Sandes einer Barkane voraussagt, führt zu der Interpretation, dass diese Dünenform von sich aus instabil ist, d.h. ihr Volumen wächst oder nimmt ab, je nach Zustrom. Daraus folgt, dass die Dynamik auf der Skala eines Dünenfelds einen fundamentalen Einfluss auf die Entwicklung einer einzelnen Düne hat.

Kapitel 2: Auf der Skala von Dünenfeldern

Dieses Kapitel beschreibt verschiedene Methoden, ein gesamtes Dünenfeld zu modellieren. Diese Modelle basieren auf Gesetzen, die aus Simulationen des viel komplexeren

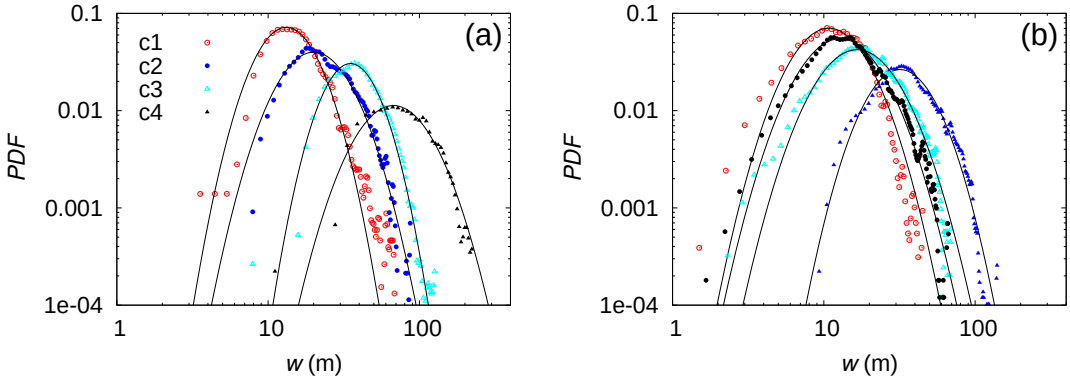

Abbildung 3: (a) Lognormaler Fit (Linie) einer gemessenen Wahrscheinlichkeitsverteilungsfunktion PDF der Dünengrößen (Punkte). Es werden vier verschiedene gemessene Dünenfelder gezeigt. (b) Lognormaler Fit (Linie) der Größenverteilung simulierter Dünenfelder (Punkte). Dabei wurde ein “effektives” Modell zur Beschreibung von Dünenfeldern benutzt. Beide Abbildungen werden in doppel–logarithmischer Skala gezeigt, auf welcher eine Lognormalverteilung eine Parabel darstellt.

DUNE–Modells, welches im vorangehenden Kapitel vorgestellt wurde, hergeleitet werden. Es wird untersucht, welches die prinzipiellen Prozesse in solch einem Feld sind, die zu einer Selektion der Dünengrößen führen.

Durch die Messung der Breite w der Dünen und ihrer gegenseitigen Entfernungen in vier realen Dünenfeldern in Marokko wurde entdeckt, dass die Dünengrößen einer Lognormalverteilung folgen (Abb. 3) und sich die Entfernungen zwischen den Dünen homogen entlang des Feldes verteilen. Eine Lognormalverteilung setzt in der Regel einen multiplikativen Prozess voraus, auf dem sich das System aufbaut, während die homogene Verteilung der Entfernungen zwischen den Dünen einen wichtigen Hinweis darauf gibt, dass Kollisionen zwischen den Dünen einen sehr wichtigen dynamischen Prozess darstellen.

Es werden Simulationen mit dem DUNE–Modell ausgeführt, um die Morphologie von Dünenfeldern zu studieren. Dadurch erhalten wir realistische Ergebnisse. Jedoch ist ein Vergleich der Ergebnisse mit realen Dünenfeldern aufgrund schlechter Statistiken unmöglich. Dies liegt an den langen Laufzeiten der Simulationen. Trotzdem helfen diese Simulationen dabei, zu bestätigen, dass Kollisionen von Dünen für die Entwicklung eines gesamten Dünenfelds relevant sind.

Um besser zu verstehen, was passiert, wenn zwei Dünen miteinander kollidieren, werden Simulationen mit dem DUNE–Modell ausgeführt. Die drei verschiedenen Endzustände Vereinigung, Solitonwellen–Verhalten und Erzeugung (Duran et al., 2005) bieten einen Mechanismus, der das kontinuierliche Anwachsen der Dünen in einem Feld unterdrücken kann. Die Untersuchung der Daten von Kollisionen zwischen lateral versetzten Dünen liefert ein allgemeines Gesetz, mit welchem die Volumina und die Positionen der Dünen nach der Kollision gefittet werden kann. Diese phänomenologischen Gesetze werden angewandt, um ein einfaches Modell zu konstruieren, mit dem der Effekt der Kollisionen in einem Dünenfeld erforscht werden kann. Dabei wirde der Sandfluss zwischen den Dünen

vernachlässigt. Es wirde gefunden, dass die Verteilung der eindimensionalen Ausdehnung der Dünen eine Gauss–Glocke bildet, d.h. in bezug auf die Höhe, Breite und Länge der Dünen, aber nicht in bezug auf ihr Volumen, wie erwartet wurde. Somit können die Kollisionen statistisch als ein additiver Zufallsprozess interpretiert werden, der eine charakteristische Dünengröße erzeugt (Durán et al., 2006a).

Wir erhalten eine bessere Approximation der Größenverteilung in einem Dünenfeld, wenn zusätzlich zu den Kollisionen der Austausch von Sand zwischen den Dünen und außerdem ihre räumliche Verteilung betrachtet werden. Diese Prozesse wurden in ein "effektives" Modell implementiert, das Dünen als Einheiten betrachtet, was die Einsparung von viel Rechenzeit auf dem Computer erlaubt. Die Simulationen von Dünenfeldern mit diesem "effektiven" Modell liefern eine lognormale Verteilung der Dünengrößen (siehe Abb. 3). Die Verteilung ist das Resultat der Konkurrenz zwischen Kollisionen und dem Austausch von Sand durch Sandfluss, der den multiplikativen Prozess bildet. Der Austausch durch Sandfluss führt zu einer Anhäufung von Sand in großen Dünen und somit zu einem Ansteigen deren Größe, während Kollisionen in den meisten Fällen eine Neuverteilung des Sandes verursachen, weshalb diese Dünen durch Kollisionen wieder an Größe verlieren.

Die Konkurrenz dieser beiden Prozesse wird mit einem analytischen Mean field Ansatz modelliert, wobei eine Master–Gleichung die Entwicklung der Verteilung der Dünengrößen beschreibt. Das Ergebnis für die Verteilung dieses Ansatzes entspricht zwar keiner exakten Lognormalverteilung, kann aber gut durch diese genähert werden. Folglich können wir die ersten beiden Momente der Verteilung, der Mittelwert $\langle w \rangle$ und die Standardabweichung S, die die Lognormalfunktion beschreiben, mit physikalischen Größen verbinden.

Somit resultiert die Standardabweichung der lognormalen Größenverteilung aus der Balance zwischen Dünenkollisionen und Austausch durch Sandfluss. Kollisionen hängen von der räumlichen Verteilung der Dünen ab. Also bekommt man eine Gleichung, die die drei statistischen und topologischen Hauptgrößen von Dünenfeldern miteinander verbindet: der Mittelwert und die Standardabweichung der Verteilung der Dünengrößen und die charakteristische räumliche Entfernung $\bar{L}$ zwischen benachbarten Dünen (Abb. 4, links (b))

$$S^3 \approx A\bar{L}\langle w \rangle^2. \tag{1}$$

$\bar{L}$ bestimmt auch die Dichte der Dünen im Feld (Abb. 4, links (a)). Folglich ist die Standardabweichung in Feldern von Barkanen vollständig durch die Dünendichte bestimmt, was z.B. erklärt, warum ein spärlich besetztes Feld eine breite Verteilung besitzt.

Die Simulationen mit dem "effektiven" Modell zeigen, dass die statistischen Größen eines Dünenfelds nur von den Bedingungen am Rand des Feldes, an welchem die Dünen einströmen, abhängen. Diese Bedingungen sind durch die Dichte ρ_0 und die Breite w_0 der einströmenden Dünen festgelegt. Die Dichte ρ der Dünen im Feld steigt mit der Dichte der einströmenden Dünen linear an

$$\rho = \rho_0 - \rho_c. \tag{2}$$

Es existiert aber eine kritische Dichte ρ_c, die überschritten werden muss, damit die einströmenden Dünen ein Feld generieren können (Abb. 4, rechts (b)). Bei kleineren Dichten

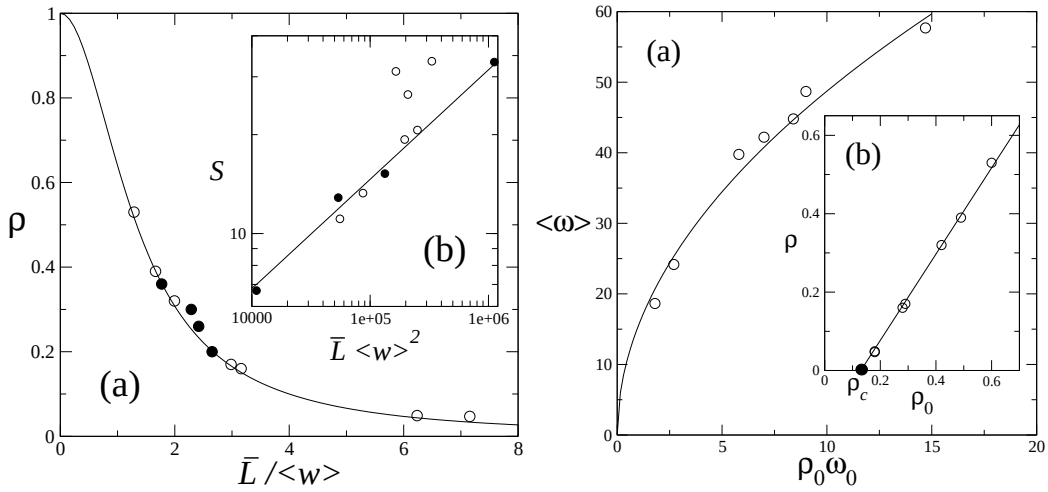

Abbildung 4: **Links: (a)** Die Dünendichte ρ als Funktion der relativen Entfernung zwischen den Dünen $\bar{L}/\langle w\rangle$. **(b)** zeigt die Abhängigkeit zwischen S und $\bar{L}\langle w\rangle^2$ durch ein Potenzgesetz $x^{1/3}$. Man erhält in diesem Fit eine Proportionalitätskonstante von $A = 0.03$. In beiden Teilen entsprechen die gefüllten Punkte realen Dünenfeldern und die nicht gefüllten simulierten Feldern. Der Fit der Daten wird durch eine durchgezogene Linie dargestellt. Die Abweichungen von drei simulierten Feldern von dem Fit in (b) sind das Ergebnis zu hoher Dichten. **Rechts: (a)** Der Mittelwert der Breite w als Funktion des Produkts von der Dichte ρ_0 der in das Feld strömenden Dünen und deren Breite w_0. **(b)** Die stationäre Dichte ρ des Dünenfeldes als Funktion von ρ_0. Beachte, dass sich für Werte $\rho < \rho_c$ (gefüllter Punkt) kein Dünenfeld ausbildet.

werden die Dünen durch den Wind zu sehr zerstreut, was die Bildung eines Feldes verhindert. Dagegen ist der Mittelwert der Breiten $\langle w\rangle$ im Feld von beiden Größen ρ_0 und w_0, die die einströmenden Dünen charakterisieren, abhängig (Abb. 4, rechts (a))

$$\langle w\rangle = \left(\bar{W}\rho_0 w_0\right)^{1/2}, \tag{3}$$

wobei $\bar{W}$ einen Schwellwert mit der Dimension einer Länge darstellt, der bestimmt, ob der Mittelwert der Dünengrößen größer oder kleiner als die Breite der einströmenden Dünen sein wird (Durán et al., 2006b).

Kapitel 3: Vegetationswachstum versus Sandmobilität

Die Stabilisierung von mobilem Sand mit Hilfe von Vegetation ist eine schon seit langem verwendete Technik. Vegetation spielt eine kompetitive Rolle, wobei die Pflanzen versuchen, die Sanddünen zu stabilisieren, den Sandfluss zu unterbinden und die Wiederherstellung eines fruchtbaren Untergrunds zu stimulieren. Der Dünensand wird unter diesem Einfluss stabilisiert, vorausgesetzt dass eine bestimmte Menge an Niederschlag fällt, der Wind nicht zu stürmisch weht und der Eingriff des Menschen vernachlässigt werden kann. Bei der Stabilisierung führt die wachsende Vegetation zu einer Transformation von einer hochmobilen Barkan–Düne zu einer unbeweglichen Paraboldüne.

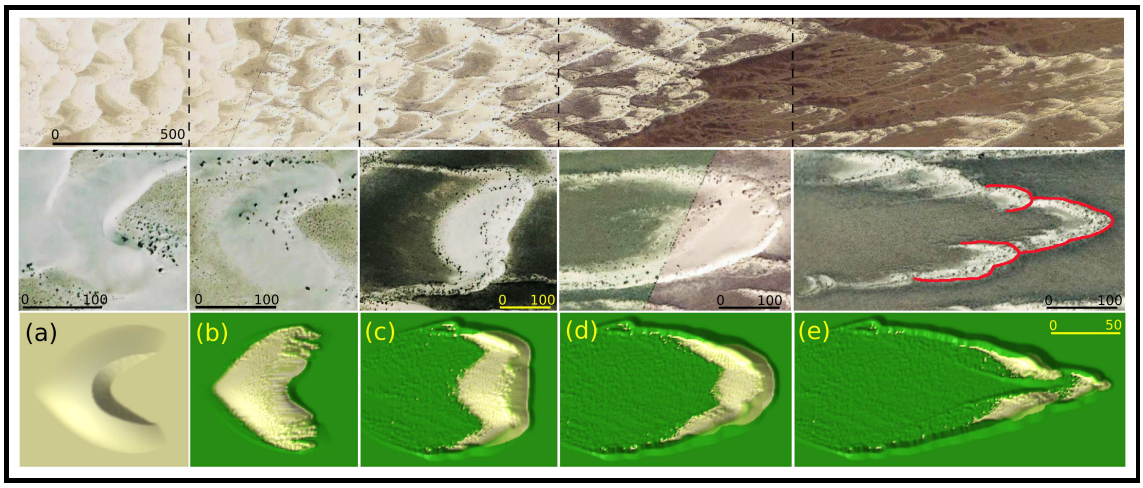

Abbildung 5: Deaktivierung mobiler Dünen mit Hilfe von Vegetation. Oben: Dünenfeld in White Sand, New Mexico. Die Barchanoide auf der linken Seite haben keine Vegetation. Sie entwickeln sich zu einer Mischung von aktiven und inaktiven Paraboldünen auf der rechten Seite (Windrichtung nach rechts). Die dunklen grünen Stellen entsprechen dichter Vegetation. Die Daten suggerieren, dass ein Übergang zwischen diesen beiden Dünenarten stattfindet, wenn die Bedeckung der Oberfläche mit Vegetation zunimmt. Dieser Übergang erscheint bei verschieden Dünen im Dünenfeld von White Sand (Bilder in der Mitte). Unten: Der gleiche Übergang als Ergebnis des numerischen Modells, welches die Wechselwirkung zwischen Sandtransport und Vegetation modelliert, mit einem Fixationsindex von $\theta = 0.22$. Die Vegetation ist in grün dargestellt.

Der Wettstreit zwischen Vegetationswachstum und der Mobilität der äolischen Oberfläche hat einen enormen Einfluss auf die ökonomischen Verhältnisse (z.B. der Landwirtschaft) von semi–ariden Regionen als auch auf globale Ökosysteme. Bisher basierten Methoden, Dünen durch Vegetation zu stabilisieren, auf dem Ausprobieren der zu testenden Methode. Es fehlte sowohl eine mathematische Beschreibung als auch Möglichkeiten einer quantitativen Voraussage. Dieses Problem ist für die Verwaltung von Küstenregionen, in welchen es hohen Sandtransport gibt, aber auch günstige Bedingungen für das Wachstum von Pflanzen existieren, von besonderer Bedeutung.

Es wird ein Satz von Differentialgleichungen vorgeschlagen, um die Konkurrenz zwischen Pflanzenwachstum und Sandmobilität zu beschreiben. Diese Gleichungen bestimmen den äolischen Transport auf granularen, mit Pflanzen bewachsenen Oberflächen, wobei auch das Wachstum und das Absterben der Pflanzen berücksichtigt wird. Anhand dieser Gleichungen wird der morphologische Übergang von aktiven Barkanen zu inaktiven Paraboldünen berechnet (Abb. 5). Dieses Model kann bestätigt werden, indem simulierte mit realen Paraboldünen verglichen werden. Dazu werden sowohl Satellitenfotos von White Sand, New Mexico (Abb. 5) als auch die Messungen von Dünen an der brasilianischen Küste ausgewertet. Die Morphologien der simulierten und der realen Dünen weisen wichtige Ähnlichkeiten auf, wie z.B. die Stellen, an welchen die Pflanzen wachsen, und die räumliche Verteilung der unbewachsenen Sandoberfläche.

Der Übergang von Barkanen in Paraboldünen wird von dem Anfangsvolumen V der Barkane, dem ungestörten saturierten Sandfluss Q, der ein Maß für die Windstärke auf fla-

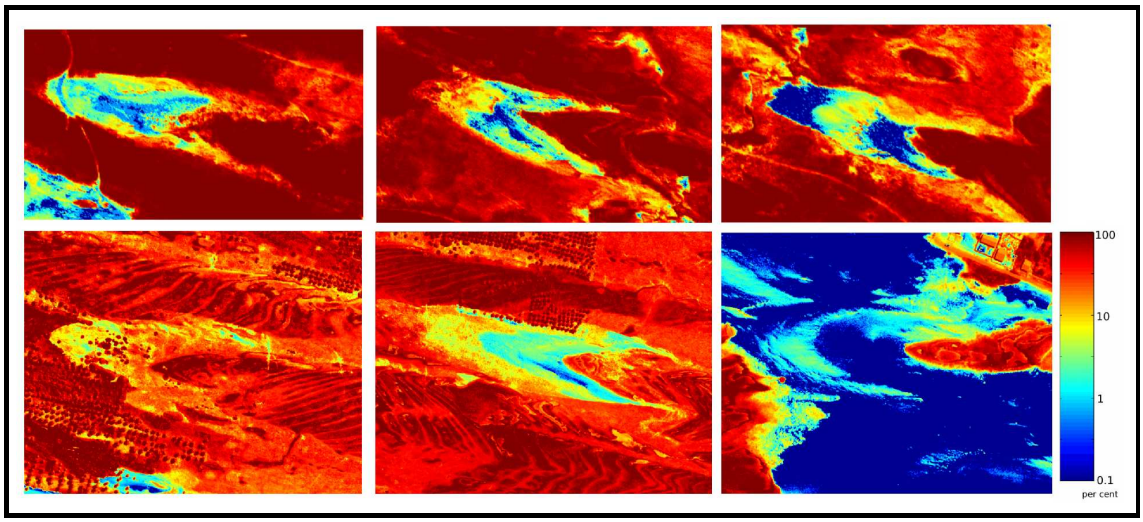

Abbildung 6: Räumliche Verteilung des Anteils an Bedeckung mit Vegetation (Farbskala) für sechs verschiedene Paraboldünen an der brasilianischen Küste. Die Dünen stellen verschiedene Stadien der Deaktivierung dar. Die Farbskala ist logarithmisch. Die Windrichtung ist von links nach rechts.

chem Untergrund ist, und der Zuwachsrate V_v der Vegetation determiniert. Der Wettstreit von Sandtransport und Vegetationswachstum führt in der Tat zu der Stabilisierung einer Barkan–Düne. Dieser Wettstreit kann durch einen dimensionslosen Kontrollparameter θ ausgedrückt werden, den wir Fixationsindex nennen. Er ist durch das Verhältnis zwischen der charakteristischen Erosionsrate auf der initialen Barkan–Düne und der Zuwachsrate der Vegetation definiert. Nachdem die charakteristische Erosionsrate mit dem Verhältnis zwischen Q und der durch das Volumen definierten charakteristischen Länge $V^{1/3}$ skaliert, kann man θ durch

$$\theta \equiv Q/(V^{1/3}V_v) \tag{4}$$

beschreiben.

Es werden für verschiedene Werte von V, Q und V_v Simulationen durchgeführt und ausgewertet. Es wird ein gemeinsamer Fixationsindex $\theta_c \approx 0.5$ gefunden, über dem die Vegetation nicht mehr die Inversion einer Barkane bewirkt. Für $\theta > \theta_c$ bleiben Barkane mobil, ansonsten werden sie durch die Pflanzen deaktiviert.

Der morphologische Übergang bei θ_c kann anhand der zeitlichen Entwicklung der normalisierten Geschwindigkeit v/v_0 der Dünen mit Vegetation für verschiedene Anfangsbedingungen demonstriert werden (siehe Beispiele in Abb. 7), wobei v_0 die Anfangsgeschwindigkeit der Düne darstellt. Bei mittleren und hohen Fixationsindizes kann ein allgemeines Verhalten festgestellt werden: Einem anfänglichen Beschleunigen der Düne folgt eine rasche Abnahme der Dünengeschwindigkeit bei $t = t_s$, wenn Inaktivierung eintritt. Für Zeiten $t < t_s$ entwickelt sich die Barkane zu einer aktiven Paraboldüne (Abb. 5, (a)-(d)), die danach ($t > t_s$) inaktiv wird (Abb. 5, (e)). Dagegen bleiben die Barkane für Werte des Fixationsindexes, die größer als θ_c sind, mobil, so dass t_s divergiert.

Die Untersuchung der Inaktivierungszeit t_s als Funktion der Parameter V, Q und V_v ergibt, dass t_s mit einer charakteristischen Migrationszeit $t_m \equiv V^{2/3}/Q$ der Düne skaliert

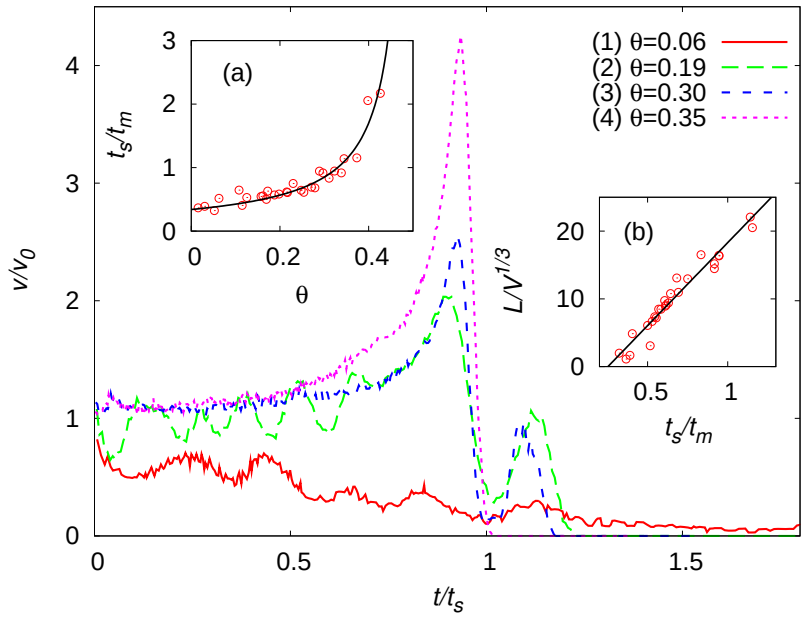

Abbildung 7: Simulationen der Evolution der normalisierten Dünengeschwindigkeit ($v - v_0$) mit Anfangsbedingungen, die durch Werte der Parameter V, Q und V_v, die den Fixationsindizes θ: 0.06 (1), 0.19 (2), 0.30 (3) and 0.35 (4) entsprechen, bestimmt sind. Inset (a): die normalisierte Zeitspanne der Inaktivierung einer Düne t_s/t_m divergiert, falls $\theta \rightarrow \theta_c$ (durchgezogene Linie). Inset (b): die normalisierte Endlänge der Paraboldüne $L/V^{1/3}$ ist proportional zu t_s/t_m. Die Punkte zeigen Simulationsergebnisse.

und einem Potenzgesetz in Abhängigkeit von θ folgt (Abb. 7, inset(a))

$$t_s \approx 0.17\, t_m/(\theta_c - \theta)\,, \tag{5}$$

welches den Übergang zwischen einer Barkan–Düne, die sich in eine inaktive Paraboldüne entwickelt, und einer aktiv bleibenden Barkan–Düne darstellt. Die Distanz L, die eine Düne während ihrer Deaktivierung zurücklegt, divergiert ebensfalls in Abhängigkeit des Fixationsindexes (Abb. 7, Inset (b)). Diese Distanz kann im Fall von Küstendünen als eine Eindringtiefe der Dünen ins Land verstanden werden, und liefert somit eine gute Abschätzung für die Fläche, die durch die Dünenbewegungen während ihrer Desaktivierung betroffen sein wird (Durán and Herrmann, 2006b).

Der Fixationsindex θ hängt ausschließlich von den allgemeinen Bedingungen ab, unter denen sich die bewachsenen Dünen entwickeln und nicht von der zeitlichen Entwicklung selbst. Deshalb erhält man das Endergebnis des Wettstreits zwischen Vegetationswachstum und äolischer Öberflächenmobilität schon aus den Anfangsbedingungen. Diese Voraussagen können direkt getestet werden und haben große Bedeutung in Bezug auf die ökonomischen Verhältnisse in semi–ariden Regionen, wie z.B. die Verwaltung von Küstengebietten und globale Ökosysteme.

Introduction

Background

Deserts are generally defined as areas with less than 250 mm of average annual precipitation. They are subdivided, in terms of the moisture deficit, in hyper arid, arid and semiarid areas and extent over about one third of the earth's land surface, comprising almost half of African continent, all central Asia and about three quarters of Australia (Fig. 1). On average, about 20 per cent of the world arid zones are covered by sand with a varying proportion, from less than 2% in North and South America to more than 30% in Australia and as much as 45% in north Africa and central Asia. Sand dunes emerge in these sand seas as result of thousands of years old aeolian process that has reshaped the whole desert landscape.

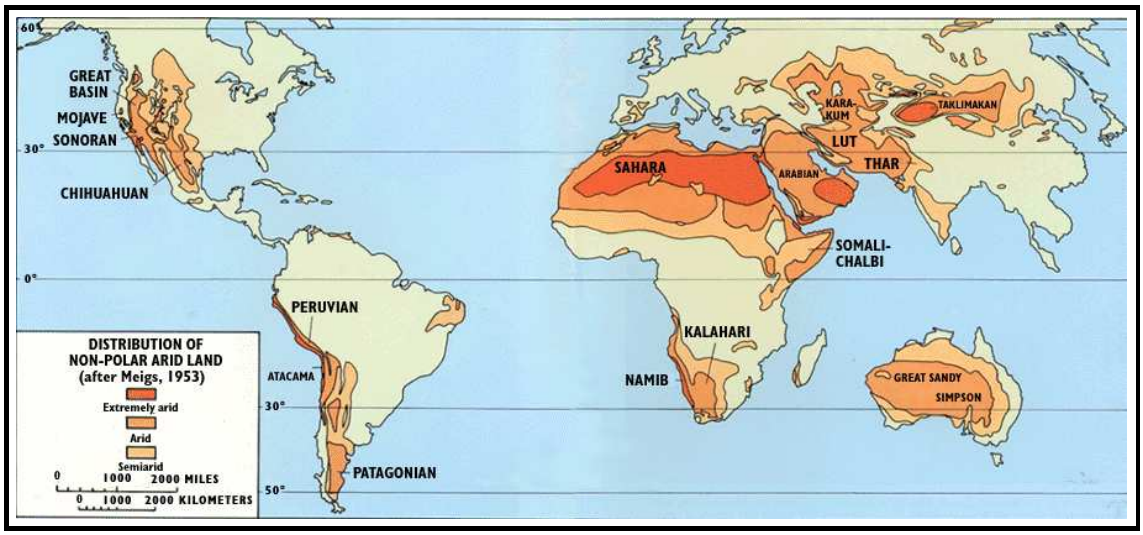

Figure 1: World distribution of arid land. The Sahara desert, the biggest of the world, is clearly seen.

In spite of their beautiful dune landscapes, deserts are among the most inhospitable regions on earth, with temperatures as high as 50^o during the day to negative values at night, and almost no water sources. In some places of the world, they remain isolated from less arid areas by natural topographic accidents like mountains. In other areas however, there is a gradual transition from dry to a more humid environment. These transition zones in

the desert margins have very fragile and delicately balanced ecosystems and therefore are very vulnerable to the phenomena of desertification, a major problem linked to desert.

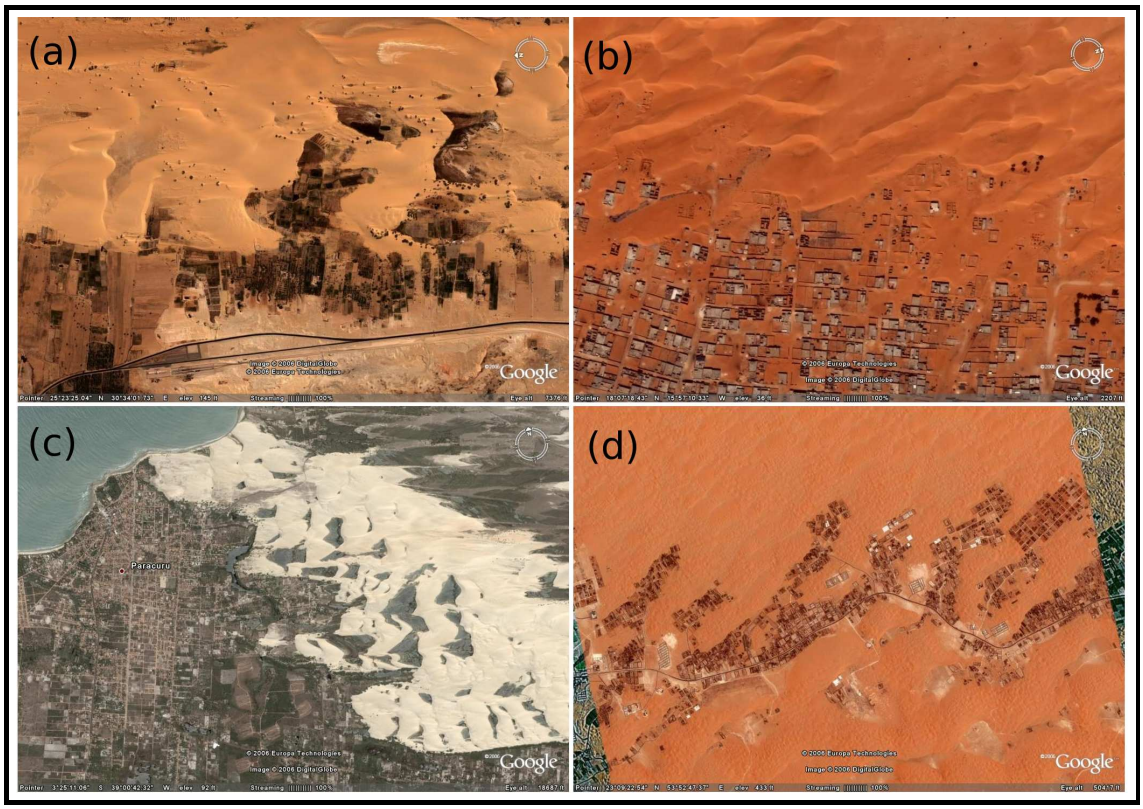

Figure 2: Examples of real threats posed by sand dunes in four places around the world: (a) El kharga, Egypt, (b) Nouakchott, capital of Mauritania, (c) Paracuru, Brasil, and (d) Sha, United Arab Emirates.

Desertification is experienced by about 40 % of global land surface which affects more than one billion people, half of them living in Africa. Desertification is a form of land degradation, occurring particularly in semi-arid areas, and has been a major issue in the international agenda. Land degradation leads to a decline in the land quality with a negative impact on its capacity to function effectively within an ecosystem by accepting, storing and recycling water, energy, and nutrients.

Additionally to desertification, migrating sand dunes also pose a direct threat to human infrastructures placed on their way. Figure 2 shows examples of dune advance toward urban areas in countries like Egypt, Mauritania, Brasil, and United Arab Emirates. Further examples from the coastal area in northeastern Brasil, shown in Fig. 3, locally illustrate desertification (Fig. 3a) and dune invasion (Fig. 3b and c).

The problems posed by dune mobility have been solved in practice using different techniques. Small dunes can be mechanically excavated or dissipated so that sand moves as individual grains rather than as a single body. However, such methods are too expensive for large dunes. Large dunes are usually immobilized using oil or by the erection of sand fences, for instance palm leaves as Fig. 4 shows. These solutions have the drawback of not

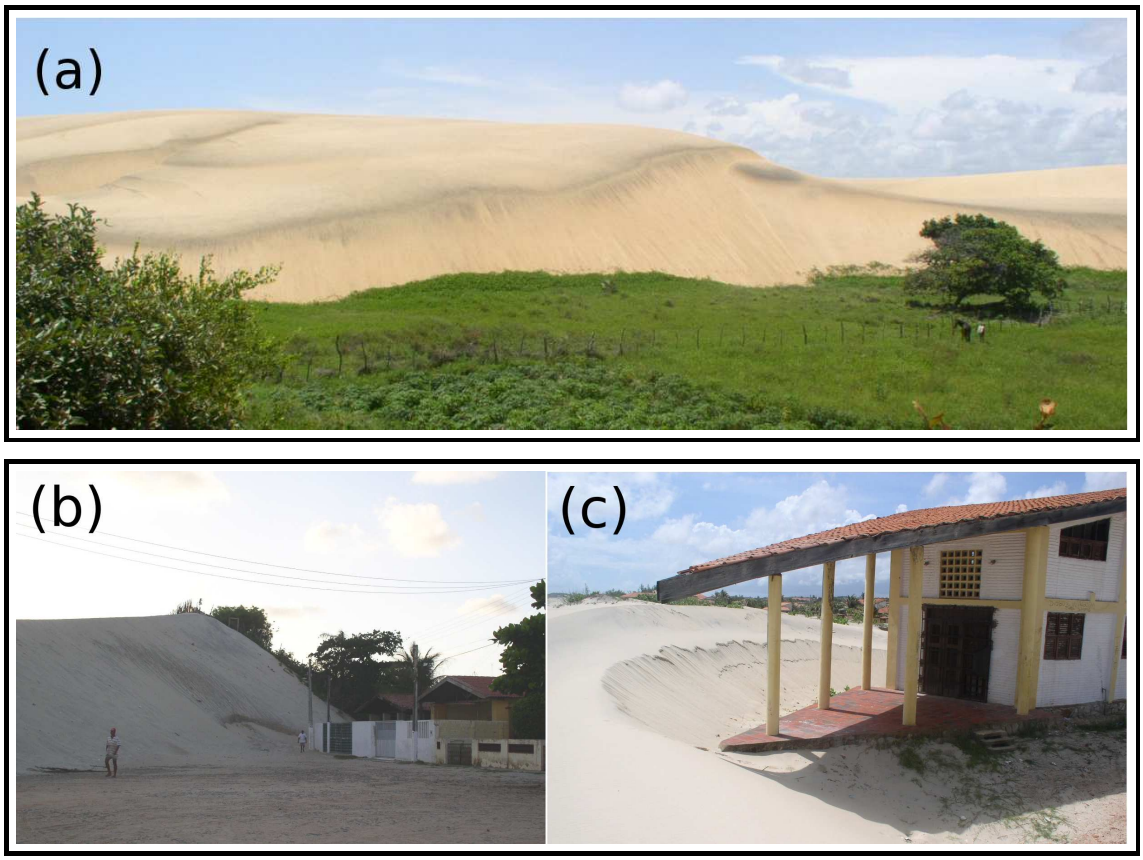

Figure 3: Examples of dune threats: in (a) the fertile soil disappears under the dune, while in (b) and (c) could be the houses.

Figure 4: Traditional method for dunes inactivation using palm leaves as sand fences.

providing a long term protection since the exposed sand remains there. To overcome this shortcoming, a suitable solution is to vegetate the sand covered areas in order to prevent sediment transport and erosion (Pye and Tsoar, 1990).

The stabilization of mobile sand using vegetation is an ancient technique. This method has been used with excellent results in coastal dunes in Algeria, Tunisia, North America, United Kingdom, Western Europe, South Africa, Israel among others (Pye and Tsoar,

1990). Vegetation plays a competing role trying to stabilize sand dunes (Hack, 1941; Pye, 1982; Anthonsen et al., 1996; Muckersie and Shepherd, 1995; Hesp, 1996), preventing sand motion (Lancaster and Baas, 1998) and stimulating soil recovery (Tsoar, 1990; Danin, 1991).

Under the influence of vegetation, dune sand tends to stabilize naturally, provided that there is a certain amount of rainfall, wind is not tempestuous and human interference is weak (Tsoar, 1990; Tsoar, 2005). Figure 5 shows the natural stabilization of active dunes in White Sand, New Mexico. During this process the vegetation cover drives a transformation from highly mobile barchan dunes (Fig. 5 left) into fixed parabolic dunes (Fig. 5 right). Since plants locally slow down the wind, they can inhibit sand erosion, reducing the exposure of moist sand to the process of evaporation, as well as enhancing sand accretion. Vegetation also traps particles of silt and clay suspended in the atmosphere which bind the surface sand grains and form a crust held together by cyanobacteria, algae and lichens (Danin, 1978; Danin, 1987). This algae crust not only becomes an important source of nutrients but enhances the sand moisture capacity, improving soil fertility (Zobeck and Fryrear, 1986). All this provides a feedback mechanism that enhances vegetation growth (Tsoar, 1990; Tsoar, 2005) and counteracts desertification process.

Figure 5: Deactivation of active sand dunes driven by vegetation in White Sand, New Mexico. The active barchan dunes (left) gradually transform into parabolic dunes (right) under the influence of vegetation (in dark). Wind blows from left to right.

Several wind erosion or sand mobility indexes have been developed in order to quantify the degree of activation of a dune when vegetation is present (Ash and Wasson, 1983; Lancaster, 1988). Initially, they were all based on two factors that increase or decrease dune mobility, namely, the degree of windiness that favors dune motion and the rain efficiency, defined as the ratio between the annual average precipitation and the annual potential evaporation, that favors vegetation growth. Recently however, Tsoar (Tsoar, 2005) considered only wind power as a better index for sand mobility, by taking into account that, in areas where the annual average rainfall is above 50 mm, the limiting factor for vegetation growth on sand dunes is wind erosion and not rain efficiency.

The ancient fight between vegetation growth and aeolian surface mobility has enormous impact on the economy of semi-arid regions and on global ecosystems. However, most approaches are just based on trial and error and there is still a lack of mathematical description and of quantitative predictability. This problem is particularly important on

coastal management where a strong sand transport coexists with favorable conditions for vegetation growth (Fig. 6). One of the central points of this thesis is to develop the mathematical description of this competition between vegetation growth and sand transport. Since numerical simulations are orders of magnitude faster than the real evolution, we would be able to study the dune inactivation process and to forecast thousands of years of real evolution. The application of these predictions to real situations of coastal management, like those depicted in Fig. 6, represents the main goal of our work.

Figure 6: Vegetation can be an extremely important tool in the control of dune migration in the coasts. In the figure, examples of active dunes along the Brazil coast.

Another central questions for dune management are related with dune stability, with the factors that determine the dune size and dune spacing in dune fields, and with the extention of the current understanding on terrestrial dunes to Marian or Venusian ones, among other.

Since the pioneer work of Bagnold during the first half of the 20 century (Bagnold, 1941), sand dunes and the underlying sand transport had been subject of a large amount of research. At the grain scale, many attempts have been made to obtain a precise description of aeolian sand transport either numerically (Anderson and Haff, 1988; Anderson, 1991; Werner, 1990; McEwan and Willetts, 1991; McEwan and Willetts, 1994; Andreotti, 2004), experimentally (Bagnold, 1941; Zingg, 1953; White, 1979; Iversen and Rasmussen, 1999) and theoretically (Andreotti, 2004; Bagnold, 1941; Kawamura, 1951; Owen, 1964; Kind, 1976; Lettau and Lettau, 1978; Ungar and Haff, 1987; Sørensen, 1991; Sørensen, 2004; Sauermann et al., 2001). However, there is still no simple analytical expression for the sand transport rate consistent with recently measurements (Iversen and Rasmussen, 1999). Further, to model sand dunes under different atmospheric and soil conditions, like in Mars or Venus, one needs to understand how the sand transport rate changes with fluid density, gravity and grain diameter.

At the dune scale, through direct measurements it was possible to uncover the morphological regularities of sand dunes shape and its relation with flow conditions (Bagnold, 1941; Finkel, 1959; Hastenrath, 1967; Hastenrath, 1987; Coursin, 1964; Lettau and Lettau, 1969; Jäkel, 1980; Slattery, 1990; Oulehri, 1992; Hesp and Hastings, 1998; Jimenez et al., 1999; Sauermann et al., 2000; Sauermann et al., 2003). It was also established that

there is a minimal dune size of ~ 10 m long (Andreotti et al., 2002a; Andreotti et al., 2002b). These size threshold led to the correct understanding of the impossibility of experimental approaches to the study of dunes using wind tunnel measurements and opened the way to numerical simulations as the only way to get insight to the mechanisms behind dune formation and evolution (Howard and Morton, 1978; Wippermann and Gross, 1986; Zeman and Jensen, 1988; Fisher and Galdies, 1988; Stam, 1997; Nishimori et al., 1999; van Boxel et al., 1999; van Dijk et al., 1999; Momiji and Warren, 2000; Sauermann et al., 2001; Kroy et al., 2002; Andreotti et al., 2002b; Hersen et al., 2002; Hersen, 2004; Hersen et al., 2004; Schwämmle and Herrmann, 2005a). In this turn, the better understanding of dune origin and scaling properties led to the identification of few centimeters long aquatic dunes as equivalent to the hundred meters long aeolian ones, reopening the way to small scale laboratory experiments (Hersen et al., 2002; Endo and Taniguchi, 2004; Hersen and Douady, 2005).

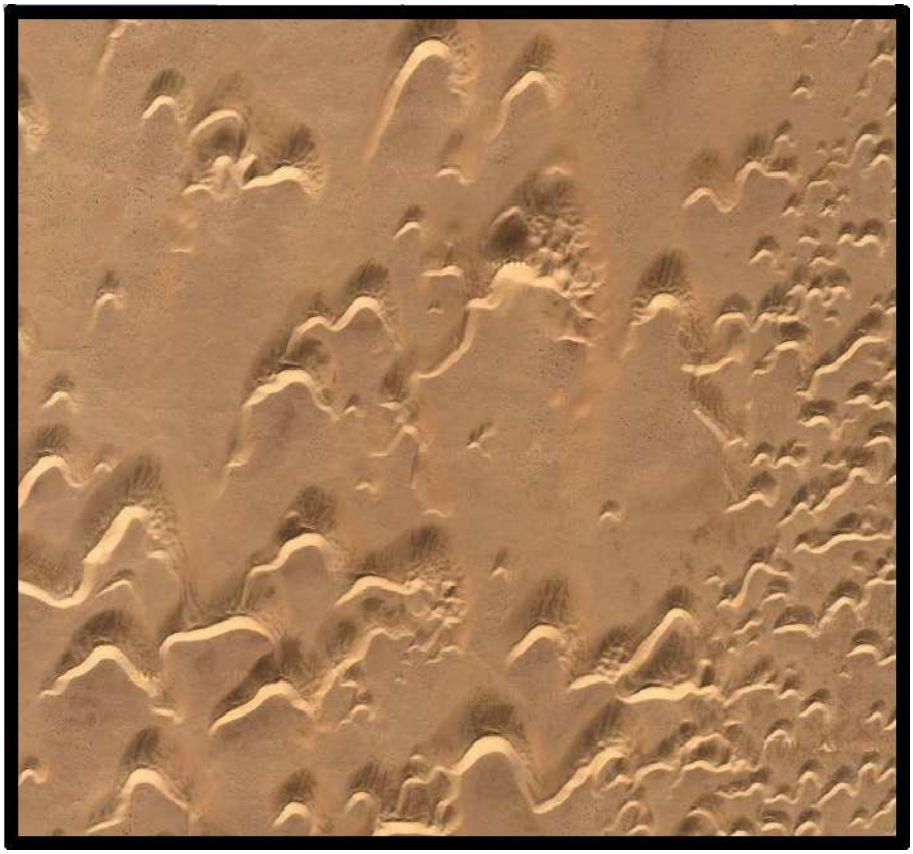

Figure 7: Example of a barchan dune field in Morocco, West Sahara. Dune fields are divided in areas where the dune size is roughly uniform.

Recently it has been shown that isolated dunes, called barchan dunes, are unstable and they can shrink until dissappear or experience unlimited growth (Sauermann, 2001; Hersen et al., 2004). However, sand seas around the world show a quite stable dunes landscape with a well selected dune size and spacing (Fig. 7), far from the collapse picture predicted by dune instability. Therefore, dune's research have shifted to consider the interaction of isolated dunes with their neighbor ones which is apparentely keen in the determination of the dune size and spacing, and consequently in the total sand carry

capacity of a migrating dune field (Lima et al., 2002; Hersen et al., 2004; Hersen and Douady, 2005; Schwämmle and Herrmann, 2003; Katsuki et al., 2005; Elbelrhiti et al., 2005). However, the precise mechanism underlying dune size and spacing selection remains unknown (Elbelrhiti and Claudin, 2006).

Scope

In this thesis we focus on the solution of three main problems breefly introduced above

First, we determine, through wind tunnel data, the phenomenological parameters of the sand transport rate model along with their dependence with basic flow and grain properties (Durán and Herrmann, 2006a). Since the sand transport model at the grain scale represents the core of the dune model we use, its validation is not only important to increase the accuracy of model predictions, but it is also keen to the extention of the model to dunes in water or in Mars and Venus conditions (Parteli et al., 2006).

The second problem is to uncover the factors that determine the size and spacing distribution of barchan dunes in dune fields (Duran et al., 2005; Durán et al., 2006a; Durán et al., 2006b). This is particularly important since the dune size and dune density are two of the most important variables to eventually chose the proper strategy for dune inactivation.

Finally, the third problem concerning the processes underlying dune stabilization in order to overcome desertification (Durán and Herrmann, 2006b). How are barchan dunes deactivated by vegetation? Which factors determine the conditions at which this vegetation driven inactivation occurs?

Overview

In Chapter 1 we describe our new model for sand transport and use experimental data in order to validate the proposed equations for the roughness length and wind velocity profile, the expression for sand transport rate and the phenomenological parameters inside them. For selfconsistency, we first provide an introductory overview about dunes and the physics of wind blown sand. We further describe the full model for sand dunes separated in four parts: (i) the model for the wind field perturbed by the topography, (ii) the sand transport rate given by the local wind strength, and (iii) the changes in sand topography determined by sand erosion or (iv) deposition processes or by the occurrences of avalanches. Finally, we also present numerical simulations of sand dunes along with some scaling relations for their shape, volume, velocity and sand flux balance, leading to a final investigation of their stability.

Chapter 2 is entirely devoted to study barchan dune fields. Here, we begin by presenting the empirical size distribution and dune spacing measurements in real dune fields. After pointing out and motivating the main problems, we address each one following three different approaches. First we perform a numerical simulation of a dune field using the dune model described in Chapter 1 which is based on sand transport at the grains scale. Later, we focus on a simplified model that consider dunes in a dune field as elementary objects

instead of taking into account their sand grains composition. This ‘coarse grain’ model includes the result of simulation of collisions between two dunes. Based on this results, we then develop an analytical ‘mean-field’ approach for the evolution of the dune size distribution of a dune field. Finally, from the combination of these approaches we derive the scaling relations that uncover the connection between the properties determining dune field evolution.

Chapter 3 is devoted to the problem of inactivation of dunes driven by vegetation. Here, we introduce our model for vegetation growth and its interaction with sand transport. This model is coupled with the dune model, fully described in Chapter 1 , in order to investigate the evolution of sand dunes when vegetation grows over. Using such improved model, we then study the conditions for dune inactivation, the time the inactivation last, the evolution of dune velocity during the inactivation process and the evolution of sand transport rate. Finally, we derive an index that determines the degree of dune inactivation and the relevant scaling relations behind this process.

In Chapter 4 the main results and achievements of this thesis are discussed as well as conclusions and remarks for future work on the new open questions risen throughout the text.

Chapter 1

Dune model and Barchan dunes

In this chapter we introduce and describe in detail the model for simulating sand dunes. Section 1.1 gives an introductory overview of the physics of sand transport and provides a handfull set of concepts for the understanding of the rest of the chapter. In section 1.2 we present a new model of sand transport (Durán and Herrmann, 2006a) along with a detailed study of the constants involved on it and their validation using experimental data. With such new developments we address in section 1.3, the full model for sand dunes including the wind, the sand carried by it, the evolution of the sand surface and the avalanches process. This model, we call 'DUNE', is used in section 1.4 to simulate numerically a special and well known kind of dune: the barchan dune.

1.1 Introduction

1.1.1 Dunes

The sand transport process through net sand erosion and deposition is capable of generating surface patterns at different scales. These patterns form a hierarchical system of three levels of aeolian bedforms superimposed to one another (Wilson, 1972). Wind ripples appear at the scale of centimeters and cover nearly 80% of the sand surface in all dune areas, while simple dunes develop at the scale of meters and hundreds of meters and are sometimes superimposed on compound dunes, called *Draa*, with sizes in the order of kilometers.

A common feature of sand dunes is the presence of one or more faces where avalanches occur. This face is called *slip face* (see Fig. 1.3 below). Since the slip face is oriented against the actual wind direction, it is conventionally used as the simplest criteria for classificating dunes. Therefore, according to their shape and orientation of their slip faces dunes can be classified into barchan dunes, transversal dunes or ridges, linear or longitudinal dunes and star dunes (Fig. 1.1). Dune's shape mainly depends on the wind direction and sand supply as Fig. 1.2 sketches (Bagnold, 1941; Fryberger, 1979; Brookfield and

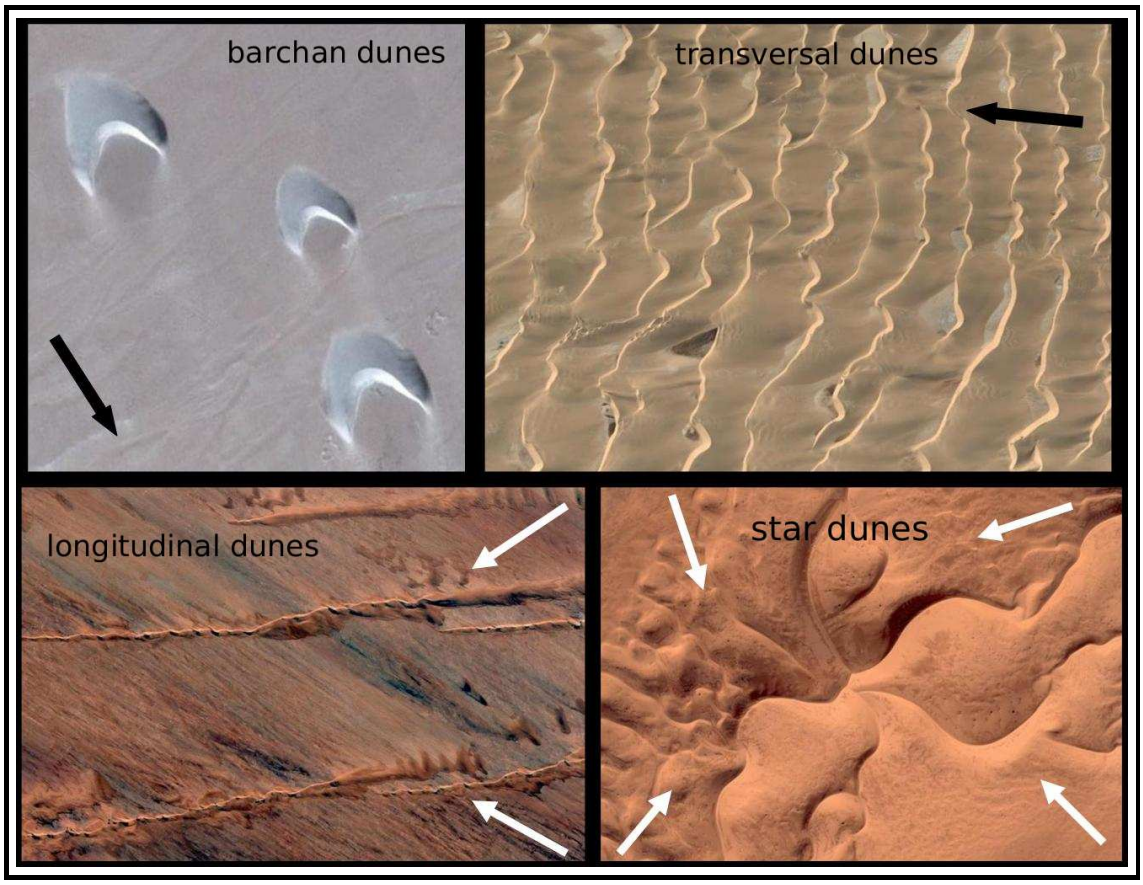

Figure 1.1: Characteristic sand dune types. Arrows indicate the prevailing wind directions during the year.

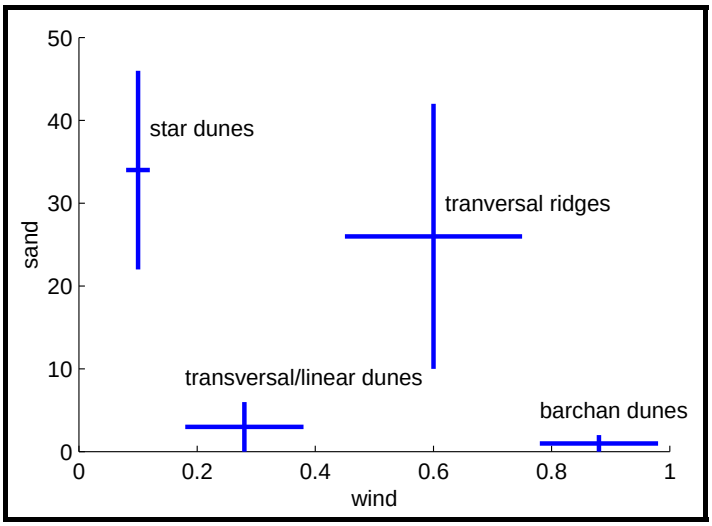

Figure 1.2: Different dune shapes according to the amount of available sand and the variability of the prevailing wind directions over the year (1: unidirectional winds, 0: wind from all directions).

Ahlbrandt, 1983; Wasson and Hyde, 1983; Nickling, 1986; Pye and Tsoar, 1990; Besler, 1992; Lancaster, 1995; Kocurek, 1996).

Barchan dunes are abundant when wind is unidirectional and there is not enough sand to cover the surface. They are isolated and high mobile dunes. Transversal ridges also form under unidirectional wind but when sand supply is abundant, and are oriented transversal to the wind direction. On the other hand, longitudinal or linear dunes appear under a prevailing bi-directional wind regime and sparce sand and are oriented along the resultant wind direction (Fig. 1.1), while star dunes result from multi-directional wind regime and abundant sand supply.

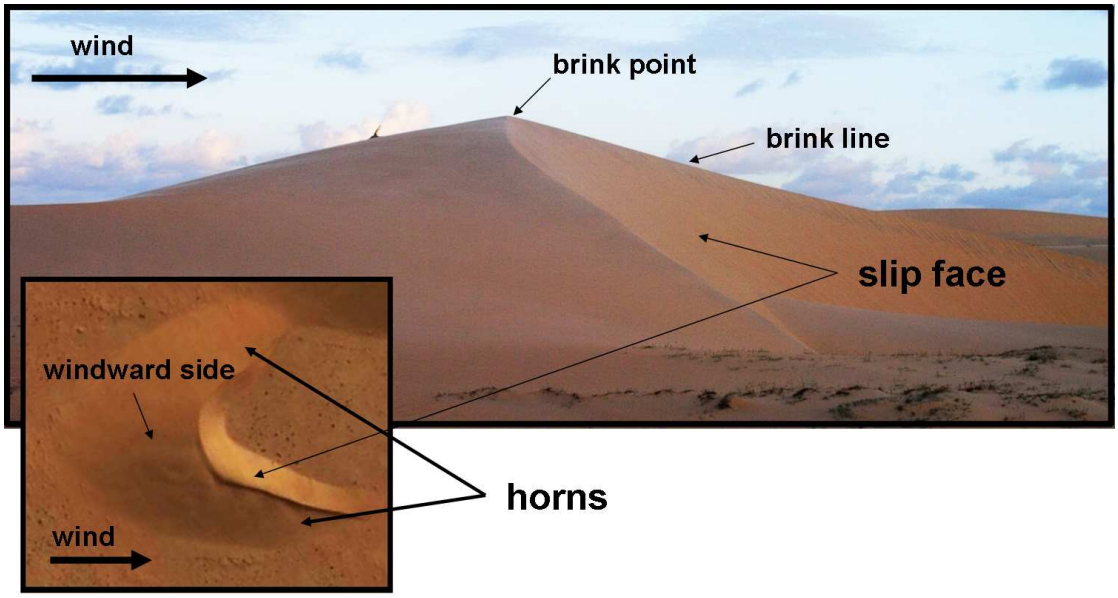

Figure 1.3: Lateral and top view of a barchan dune with some of its most characteristic features namely the slip face, the brink line and the horns.

Barchan dunes

Figure 1.3 shows a photo of a typical barchan dune. These dunes are the most studied ones, either making measurements (Bagnold, 1941; Finkel, 1959; Hastenrath, 1967; Hastenrath, 1987; Coursin, 1964; Lettau and Lettau, 1969; Jäkel, 1980; Slattery, 1990; Oulehri, 1992; Hesp and Hastings, 1998; Jimenez et al., 1999; Sauermann et al., 2000; Sauermann et al., 2003) or with numerical simulations (Howard and Morton, 1978; Wippermann and Gross, 1986; Zeman and Jensen, 1988; Fisher and Galdies, 1988; Stam, 1997; Nishimori et al., 1999; van Boxel et al., 1999; van Dijk et al., 1999; Momiji and Warren, 2000; Sauermann et al., 2001; Kroy et al., 2002; Andreotti et al., 2002b; Hersen et al., 2002; Hersen, 2004; Hersen et al., 2004; Schwämmle and Herrmann, 2005a). Their importance arise from their huge mobility ($20 - 100$ m/yr) compared to the other dunes, which leads to a direct impact onto their surroundings. Furthermore, since aeolian barchan dunes have a minimal size of about 5 to 10 m long (Sauermann et al., 2001; Andreotti

et al., 2002a; Andreotti et al., 2002b), it is virtually impossible to study them experimentally. This is an important reason why numerical simualtions has been a very important tool to get some insight into them. However, recently findings in rescaled underwater barchan dunes have reopen the way to experimental research (Hersen et al., 2002; Endo and Taniguchi, 2004; Hersen, 2005; Hersen and Douady, 2005).

Barchan dunes have a typical 'C' shape with horns pointing downwind and with a slip face in between, as illustrated in Fig. 1.3. The brink line is defined as the separating line between the face where avalanches occurs (slip face) and the rest of the dune, while its highest point is called *brink point*.

Barchan dunes, as we will see in the rest of the chapter, represent the only stable sand shape that can arise under the simplest wind conditions, namely, unidirectional wind. This fact transforms barchan dunes into the ideal object to understand how the collective motion of millions of sand grains on a solid ground can organize itself into such a beautiful structure.

1.1.2 Physics of wind blown sand

Atmospheric boundary layer

The sediment transport is one of most important processes behind geomorphological changes. In the aeolian case, the wind in the atmospheric boundary layer provides the energy necessary to sand transport.

The atmospheric boundary layer is defined as the lowest planetary layer where wind is influenced by surface friction from vegetation and topography. At the boundary layer, wind is turbulent and vertical mixing is strong while far from it the wind is approximately geostrophic and there is a weak coupling between surface and atmosphere (Peixoto and Oort, 1992).

Within the atmospheric boundary layer the vertical wind profile $v(z)$ is determined using the Prandlt turbulent closure that gives an expression for the shear stress τ in terms of the vertical velocity gradient (Peixoto and Oort, 1992)

$$\tau = \rho(\kappa z)^2 \left(\frac{\partial v}{\partial z}\right)^2 \tag{1.1}$$

where ρ is the fluid density and $\kappa \approx 0.4$ is the von Kármán universal constant for turbulent flow. Integrating Eq.(1.1) one obtains the well known logarithmic velocity profile

$$v(z) = \frac{u_*}{\kappa} \ln \frac{z}{z_0} \tag{1.2}$$

where z_0 denotes the roughness length of the surface and $u_* = \sqrt{\tau/\rho}$ the wind shear velocity. The roughness length z_0 is the layer of zero flow velocity defined by the size of the surface perturbations. The shear velocity u_* is a measure of the shear stress characterizing the flow and, as we will see later on, its ability to carry sediments. In this sense the shear velocity represents the most important quantity of the fluid as sediment carrier.

Sand

Sediments are classified according to its grain diameter d from large ($d = 2$ m) to small ($d = 2\,\mu$ m) diameters into the categories “boulders”, “pebbles”, “sand”, “silt” and “clay” (Friedman and Sanders, 1978). Sand consist mostly of quartz (SiO_2) with density $\rho_g = 2650$ kg/m^3 and has a diameter ranging from $d \approx 2$ mm for very coarse sand, to $d \approx 0.06$ mm for very fine sand. Figure1.4 depicts the grain size distribution of different aeolian sediments.

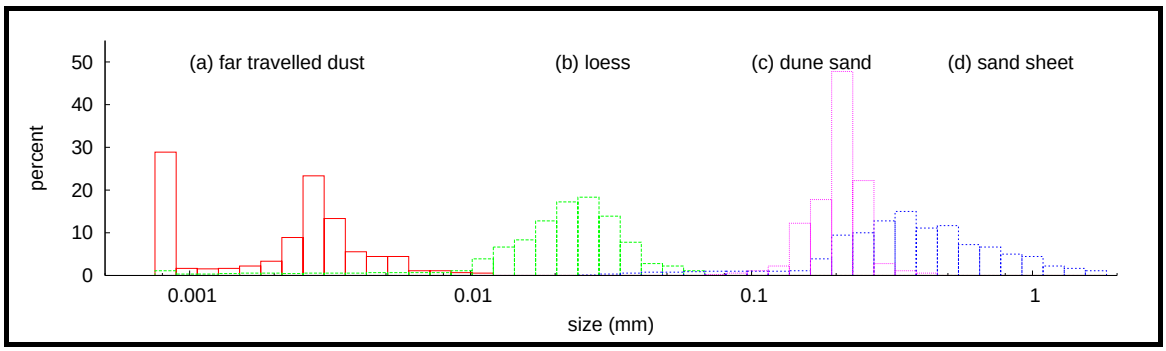

Figure 1.4: Grain size histograms from (a) dust, (b) loess, (c) sand dune and (d) sand sheet. After Pye and Tsoar (Pye and Tsoar, 1990)

The threshold for entrainment

Sediments lying in a fluid bed are subjected to three main types of forces responsibles for their movement. Namely, the drag force F_d due to fluid motion, directed in the flow direction, the lift force F_d which arise from the static pressure difference between the bottom and top of a grain caused by the strong velocity gradient near the ground, and the gravity force F_g that directly counteracts the lift force. The force balance in a grain of diameter d that is about to rotate around its pivot point p as depicted in Fig. 1.5 is given by

$$F_d \frac{d}{2} \cos\phi = (F_g - F_l) \frac{d}{2} \sin\phi \tag{1.3}$$

For a turbulent flow the drag force is the Newton drag and scales with the square of the fluid velocity, while the lift force is approximately proportional to the fluid drag (Chepil, 1958). Since fluid velocity at a given height scales with the shear velocity u_* Eq. (1.2), the force balance Eq.(1.3) defines the minimal shear velocity for grain movement which is called *fluid threshold* or *aerodynamic entrainment threshold shear velocity* u_{*ta}

$$u_{*ta} = A_a \sqrt{dg(s-1)} \tag{1.4}$$

where d is the grain diameter, $s \equiv \rho_g/\rho$ is the grain-fluid density ratio and g is the gravity acceleration. The coefficient A_a is called the Shields-Bagnold parameter ((Shields, 1936)). This expression neglects cohesive and adhesive forces and thus it is only valid for grain diameters larger than 0.2 mm.

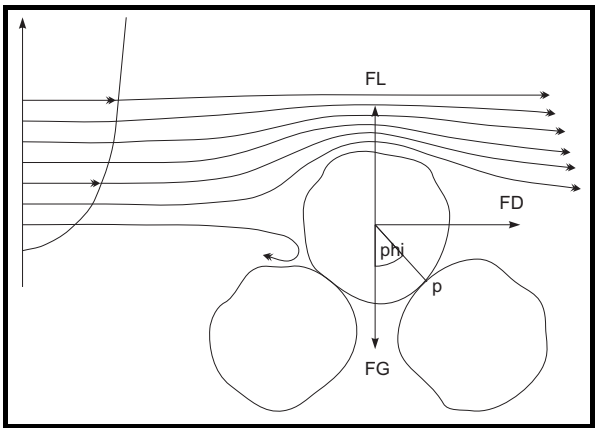

Figure 1.5: Grains start to role when the applied tangential forces are larger than the resisting grain movement.

Saltation, grain splash and feedback effect

Aeolian sand transport is generally classified into suspension and bed-load according to the degree of detachment of the grain from the ground. Bed-load can further be divided into saltation, reptation and creep (Pye and Tsoar, 1990). Grain are suspended in air when the vertical component of the turbulent velocity fluctuations exceeds the settling velocity. In typical sand storms, when shear velocities are in the range 0.2 to 0.6 m/s (Pye and Tsoar, 1990) particles with a maximum diameter of $0.04 - 0.06$ mm can be transported in suspension (Fig. 1.6). Typical sand dune grains have a diameter of about 0.25 mm (Fig. 1.4) and are transported via bed-load and mainly saltation.

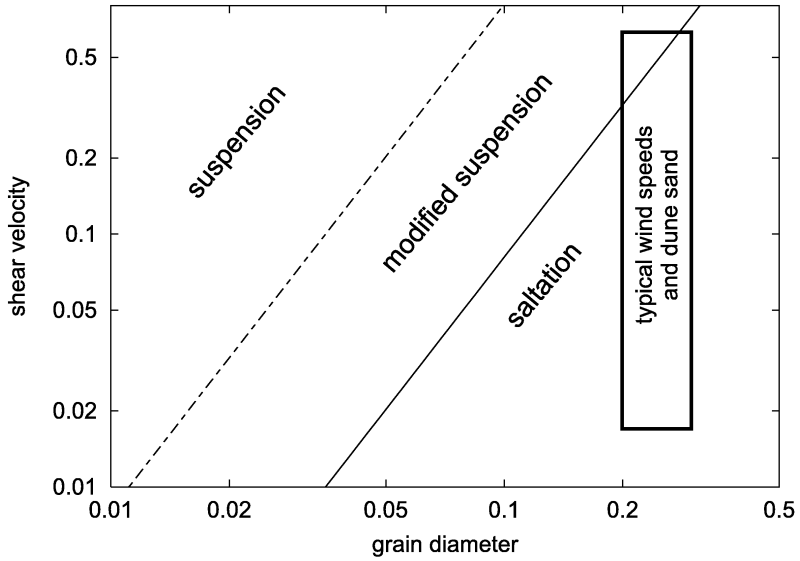

Figure 1.6: Surface wind shear velocity perturbation.

Saltation occurs when an ejected grain experiences a ballistic flight determined by the balance between the wind drag and gravity. This sand transport mechanism is conceptually

divided into sub-processes. Once the air shear velocity exceeds the entrainment threshold u_{*ta} Eq.(1.4) some grains at the surface are lifted by the wind and accelerated during their flight before they impact onto the bed again. The interaction between an impacting grain and the bed is called splash process (Nalpanis et al., 1993; Rioual et al., 2000; Anderson, 1991).

The splash process is the main source of new grains into the fluid. Since for each impacting grain more than one are splashed into the fluid, a cascade process occurs which leads to an exponential increase of sand flux (Anderson, 1991). However, the momentum transferred from the air to the grains gives rise to a desacceleration of the air itself. Therefore, sand flux cannot continuously increasing. This negative feedback mechanism in saltation leads to an equilibrium transport rate called saturation at which no more grains enter to the flow. This occurs when the shear velocity of the wind inside the saltation layer reach the minimum value for saltation to takes place, i.e. the saltation threshold value u_{*t}. Notes that this is a different threshold from the aerodynamic entrainment threshold shear velocity u_{*ta} previously defined. In general the shear velocity needed to sustain saltation is smaller than those needed to start it, and satisfies the relation

$$u_{*t} = 0.8\, u_{*ta} = A\sqrt{dg(s-1)} \tag{1.5}$$

where $A \equiv 0.8A_a$ (Pye and Tsoar, 1990).

1.2 Sand transport model

The evolution of a sand surface is determined by changes in the amount of sand transported by the wind. Initially, the grains at the surface are lifted by the wind and accelerated during their flight. After they impact the surface, the splashed grains are accelerated too, increasing the sand flux. However, since the amount of sand carried by the wind has a maximum value, a stationary state, called saturated state, is reached at which no more grains can enter to the flow. The sand flux q in this state is called the saturated flux q_s and increases with the wind strength u_*.

In this section we develop a new model for the saturated sand flux based on the previous models (Sørensen, 2004; Sauermann et al., 2001), and assuming the presence of a focal point in the velocity profile (Sørensen, 1991). We also show that depending on the focal point height the saturated flux increases as u_*^2 as in Ungar and Haff and Andreotti models (Ungar and Haff, 1987; Andreotti, 2004; Almeida et al., 2006), or increases faster than u_*^2 (in the limit as u_*^3) as in Bagnold, Owen, Sørensen and Sauermann models (Bagnold, 1941; Owen, 1964; Sørensen, 1991; Sauermann et al., 2001), or finally, increases slower than u_*^2 as in some of the Iversen and Rasmussen wind tunnel data (Iversen and Rasmussen, 1999). Although in the natural environment the saturated sand flux will inevitably create a bed with sand ripples, we assume an uniform flat bed, thus omitting influences from form drag.

Next we derive a model for the wind velocity profile including the saltation feedback, and calculate its parameters using wind tunnel data. Afterwards we use this wind velocity model to derive a sand flux expression $q_s(u_*)$, which is calibrated using existing wind tunnel data.

1.2.1 The wind velocity profile including grains movement

During saltation the grains extract momentum from the air. A fraction of this momentum is dissipated by bed collisions, and the rest accelerates the grain flow itself. Thus, in the saltation layer the total shear stress τ is divided in the air-borne shear stress τ_a and the shear stress carried by the grains, the grain-borne shear stress τ_g. Hence,

$$\tau = \tau_a(z) + \tau_g(z), \tag{1.6}$$

or, in terms of the related shear velocities

$$u_{*a}(z) = u_* \sqrt{1 - \tau_g(z)/\tau}, \tag{1.7}$$

where u_* is the wind shear velocity above the saltation layer and u_{*a} is the wind shear velocity in the saltation layer.

Once the saturated regime is reached, the wind is not strong enough to accelerate new grains. Thus, the air-borne shear stress at the surface τ_{a0} is reduced to a minimal value, just sufficient to maintain a stationary grain flow. From now on subscript 0 means surface values.

Following (Sørensen, 2004), we define

$$a(z) = \tau_g(z)/\tau_{g0}. \tag{1.8}$$

Using Eqs. (1.6), (1.7) and (1.8) the wind shear velocity in the saltation layer is given by

$$u_{*a}(z) = u_* \sqrt{1 - (1 - u_{*a0}^2/u_*^2)\ a(z)}, \tag{1.9}$$

that satisfies the boundary conditions $u_{*a} = u_{*a0}$ at the surface, where $a(z) = 1$, and $u_{*a} = u_*$ above the saltation layer, where $a(z) = 0$.

This expression can be simplified by approximating the square root by a linear function. However, the direct substitution $\sqrt{1-x}$ by $1 - x$ (Sørensen, 2004), does not satisfy the boundary condition $u_{*a} = u_{*a0}$ at the surface and, hence, leads to an inconsistency. Instead, we replace $\sqrt{1 - (1 - u_{*a0}^2/u_*^2)\ a(z)}$ by $1-(1 - u_{*a0}/u_*)\ a(z)$, which reproduces the boundary conditions and the monotony of the original square root expression.

The new wind velocity profile $v(z)$ is again calculated using the Prandlt turbulent closure (1.1) and gives

$$v(z) = \kappa^{-1} u_* \left(\ln(z/z_0) - (1 - u_{*a0}/u_*)\ b(z)\right), \tag{1.10}$$

where z_0 is the grain based roughness length and

$$b(z) = \int_{z_0}^{z} dz'\, a(z')/z'. \tag{1.11}$$

Near the bed, where $a(z) \sim 1$, the wind velocity recovers its usual logarithmic profile Eq.(1.2) with a reduced shear velocity $u_{*a0} < u_*$,

$$v(z) \approx \kappa^{-1} u_{*a0}\ \ln(z/z_0), \tag{1.12}$$

whereas, above the saltation layer $a(z) = 0$ and the wind profile is logarithmic with an unperturbed shear velocity u_* and a saltation based roughness length z_0'

$$v(z) = \kappa^{-1} u_*\ \ln(z/z_0'). \tag{1.13}$$

This roughness length z_0' takes into account the apparent rugosity of the saltation

$$z_0' \approx z_0\ \exp\left((1 - u_{*a0}/u_*)\ b_\infty\right), \tag{1.14}$$

with $b_\infty = b(z \to \infty)$.

The wind profile in Eq. (1.10) depends on the minimal surface air shear velocity u_{*a0} and on the vertical distribution of the grain-borne shear stress $a(z)$. Owen (Owen, 1964) assumed that the former equals the saltation threshold shear velocity u_{*t} Eq. (1.5), i.e. the smallest shear velocity above the saltation layer in order for sand transport to occur. However, in numerical simulations (Anderson and Haff, 1988; Anderson, 1991; Andreotti, 2004) and in Bagnold measurements, the air shear velocity inside the saltation layer can be below this threshold. This can also be regarded as a consequence of the presence of a focal point in the velocity profile, as was claimed by Bagnold (Bagnold, 1941) and

Andreotti (Andreotti, 2004). Following this idea, there is a height $\bar{z}$ at which the wind velocity is almost constant for all shear velocities, namely

$$\begin{aligned} v(\bar{z}) &= \kappa^{-1} u_* \left(\ln(\bar{z}/z_0) - (1 - u_{*a0}/u_*)\, b(\bar{z})\right), \\ &= \kappa^{-1} u_{*t} \ln(\bar{z}/z_0). \end{aligned} \tag{1.15}$$

The last equality holds because if the shear velocity equals its threshold value, as there is no sand transport, it follows that $u_{*a} = u_{*t}$.

From Eq. (1.15)

$$u_{*a0}(u_*) = u_{*t} - (\mu - 1)(u_* - u_{*t}), \tag{1.16}$$

where the constant μ is defined as

$$\mu \equiv \ln(\bar{z}/z_0)/b(\bar{z}). \tag{1.17}$$

Since in the saturated regime the grain-borne shear stress decreases with height, one has $\mu \geq 1$, which implies that the surface air shear velocity, given by Eq. (1.16), decreases with u_*. However, since u_{*a0} must be positive there is a limit value for the wind shear velocity ($\mu u_{*t}/(\mu - 1)$) beyond which Eq. (1.16) is no longer valid. On the other hand, if we eliminate the focal point assumption ($\bar{z} = z_0$) then $\mu = 1$ and u_{*a0} equals the threshold value u_{*t}.

Combining Eqs. (1.10 and (1.16), we obtain the wind profile

$$v(z) = \kappa^{-1} u_* \left(\ln(z/z_0) - \mu\,(1 - u_{*t}/u_*)\, b(z)\right). \tag{1.18}$$

In order to determine an explicit expression for $b(z)$, Sauermann (Sauermann et al., 2001) assumed an exponential profile for the grain-borne shear stress, as was found numerically by Anderson and Haff (Anderson, 1991). In that case $a(z) = \exp(-z/z_m)$, and $b(z)$ is given by

$$b(z) = E_i(z_0/z_m) - E_i(z/z_m), \tag{1.19}$$

where z_m is the characteristic height of the saltation layer and $E_i(x)$ is the exponential integral defined as

$$E_i(x) = \int_x^\infty dx' \, \exp(-x')/x'. \tag{1.20}$$

Equation (1.10) together with Eqs. (1.16) and (1.19) determines the wind velocity profile using three parameters, the grain based roughness length z_0, the focal height $\bar{z}$ and z_m. Since both, $\bar{z}$ and z_m are related to the height of the saltation layer, we assume that they are proportional to each other. Hence, we introduce the ratio

$$r \equiv \bar{z}/z_m, \tag{1.21}$$

as a constant. Consequently, the wind velocity profile reads

$$v(z) = \kappa^{-1} u_* \left[\ln(z/z_0) - \mu\,(1 - u_{*t}/u_*)\, \left(E_i(z_0/z_m) - E_i(z/z_m)\right)\right], \tag{1.22}$$

where μ is given by

$$\mu = \ln(r\, z_m/z_0)/(E_i(z_0/z_m) - E_i(r)). \tag{1.23}$$

when taking Eqs. (1.19), (1.21) and (1.17) into account.

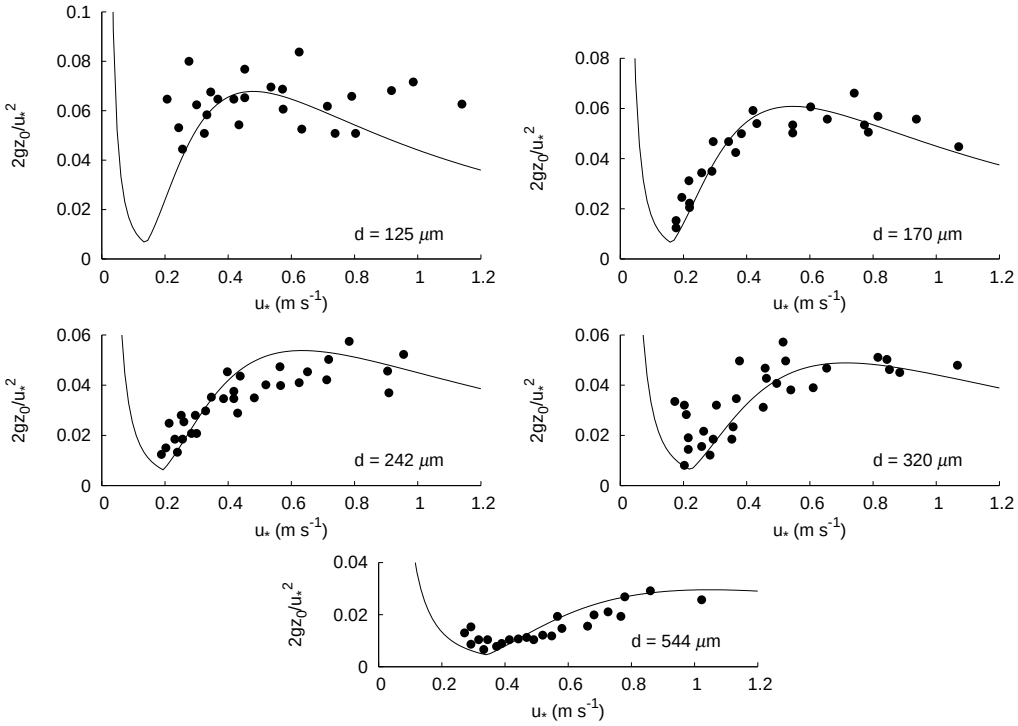

Figure 1.7: Rescaled roughness as a function of the shear velocity for different grain diameters. Points are measurements (Rasmussen and Rautahemio, 1996) and lines the analytical approximation Eq. (1.24) when considering Eqs. (1.27) and (1.29), for an arbitrary r between 0 and 10. The value of r is the same for all plots while z_m and z_0 only change with the grain diameter d.

Experimental verification of the roughness length formula

Substituting Eqs. (1.16) and (1.19) into Eq. (1.14), the apparent roughness length of the saltation layer is

$$z_0'(u_*) = z_0 \, \exp\left(\mu \left(1 - u_{*t}/u_*\right) \, E_i(z_0/z_m)\right) \tag{1.24}$$

where, for small values of the fraction z_0/z_m, the exponential integral can be approximated by

$$E_i(z_0/z_m) \approx -\gamma - \ln(z_0/z_m) + (z_0/z_m). \tag{1.25}$$

where $\gamma \approx 0.5772$ is the Euler-Mascheroni constant.

In order to find an approximate expression for z_m, z_0 and r, we fit roughness length data for different grain diameters and shear velocities (Rasmussen and Rautahemio, 1996) using the Eq. (1.24) (Fig. 1.7). This is sufficient to determine z_0. However, r and z_m cannot be determined in this way because for any $0 < r \leq 10$, there is always a value of z_m that fits all the data. This value of z_m scales with $\sqrt{d}$ and is given by

$$z_m(r) \propto \sqrt{d}/(1 + 1.4r). \tag{1.26}$$

The scaling of z_m with $\sqrt{d}$ instead of d, also found by Andreotti (Andreotti, 2004), contradicts the dimensional analysis suggesting that gravity and fluid viscosity ν are important

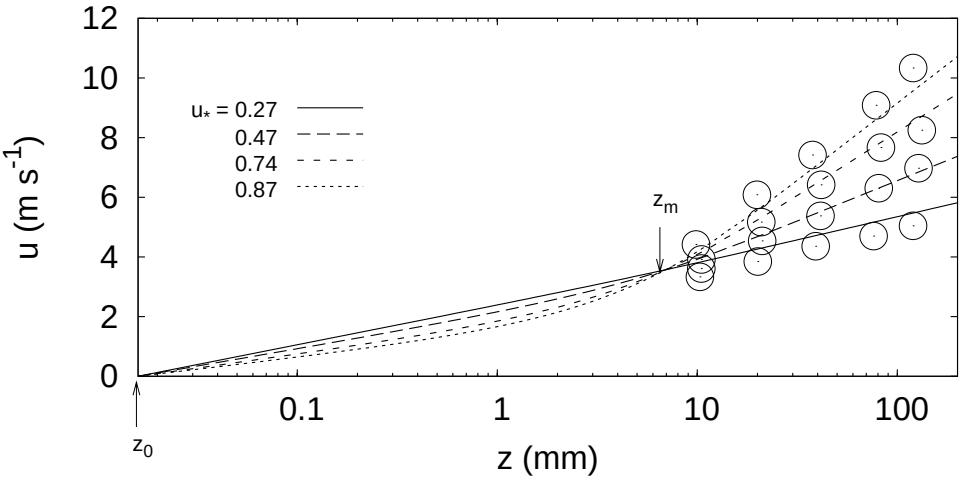

Figure 1.8: Wind velocity profile over an active sand bed for $u_* = 0.27$, 0.47, 0.74 and 0.87 m/s. Lines are the analytical approximation given in the text using $r = 1$ and circles wind tunnel data (Rasmussen and Sørensen, 2005). Note the focal height $\bar{z} = z_m$ at which all velocities are equal, along with the saltation region for $z < 10mm$, where the shear velocity is strongly reduced underneath the threshold value $u_{*t} \approx 0.24$, and the outer unperturbed region for $z > 10mm$.

extra parameters (Andreotti, 2004). Since the threshold shear velocity u_{*t} scales with $\sqrt{d}$, z_m can be rewritten as

$$z_m(r) = c(r)\, u_{*t}\, t_v. \tag{1.27}$$

where $c(r) \approx 14/(1+1.4r)$, $t_v \approx 5.38$ ms is a timescale defined using the fluid kinematic viscosity ν (Andreotti, 2004)

$$t_v = \left(\nu/g^2\right)^{1/3}, \tag{1.28}$$

and the threshold shear velocity $u_{*t} = A\sqrt{dg(s-1)}$, where $A \approx 0.1$ is the Shield-Bagnold parameter and $s = \rho_g/\rho \approx 2162$ is the grain-fluid density ratio.

The grain based roughness length was fitted using the minimum of the curves in 1.7 as

$$z_0 = d/20, \tag{1.29}$$

where d is the grain diameter.

For the small grain diameter ($d = 125\,\mu$ m) and shear velocities over 0.8 m/s, the analytical approximation Eq. (1.24) is well below the measurements (Fig. 1.7), because we select a constant z_m for all u_*. Based on the scaling of z_m with u_{*t} we found that a linear dependence with u_* remarkably improves the fit. Nevertheless, in the normal range of normalized shear velocities $u_*/u_{*t} < 5$ a constant z_m is good enough and keeps the model simple.

Experimental verification of the wind velocity profile with feedback effect

Using the above expressions for z_m and z_0 we compare the predicted wind velocity profile in Eq. (1.10), assuming $r = 1$, i.e. the focal height $\bar{z}$ equals z_m, with wind velocity data over a sand bed of $d = 320\,\mu$ m (Rasmussen and Sørensen, 2005). The data was taken for the shear velocities 0.27, 0.47, 0.74 and 0.87 m/s, as Fig. 1.8 shows. It is also clear from the figure the reduction of the minimal shear velocity inside the saltation layer as u_* increases. Note that the unperturbed logarithmic profile above the saltation ayer extends down to ~ 6 mm, in accordance with (Rasmussen and Rautahemio, 1996).

1.2.2 Saturated flux

The saturated flux is calculated by (Sørensen, 2004)

$$q_s = \Phi\, l/\rho_{\text{sand}} \tag{1.30}$$

where Φ denotes the volume flux of grain impacting the surface, and l is the mean saltation length. The volume flux Φ can be obtained from the surface grain-borne shear stress τ_{g0} and the mean horizontal velocity difference between the impacting and ejected grains $(u_x^{imp} - u_x^{eje})$

$$\Phi = \frac{\tau_{g0}}{\rho_{\text{sand}}(u_x^{imp} - u_x^{eje})} = \frac{\rho}{\rho_{\text{sand}}}\frac{(u_*^2 - u_{*a0}^2)}{(u_x^{imp} - u_x^{eje})}. \tag{1.31}$$

where the sand density ρ_{sand} is introduced to obtain a volume sand flux instead of the mass sand flux.

On the other hand, the mean saltation length can be approximated by the length of a ballistic trajectory (Sauermann et al., 2001)

$$l = u_s \frac{2u_z^{eje}}{g}, \tag{1.32}$$

where u_z^{eje} is the mean vertical component of the grain ejection velocity and u_s is the mean horizontal velocity of the grains in the saturated state.

In the saturated state the loss of momentum by collisions is balanced by the mean fluid drag on the grains. Assuming that the mean fluid drag f_{drag} on the grains at the saltation layer can be written as a Newton fluid drag at a reference height z_1 acting on an effective grain layer with horizontal velocity u_s, and that the loss of momentum by collisions represents a bed friction that compensates the grain borne shear stress at the surface τ_{g0}, the momentum balance is simply $f_{drag} = \tau_{g0}$. Moreover, the grain borne shear stress is $\tau_{g0} = \rho_s\, g/(2\alpha)$ and the mean fluid drag $f_{drag} = \rho_s g(|v(z_1) - u_s|/u_f)^2$, where ρ_s is the mean density of grains at the saltation layer. Thus, the momentum balance in the whole saltation layer becomes (Sauermann et al., 2001)

$$|v(z_1) - u_s| = u_f/\sqrt{2\alpha}, \tag{1.33}$$

which yields a mean horizontal grain velocity

$$u_s = v(z_1) - u_f/\sqrt{2\alpha}. \tag{1.34}$$

In the above expressions, the constant α is defined as the ratio

$$\alpha = u_z^{eje}/(u_x^{imp} - u_x^{eje}), \tag{1.35}$$

$v(z_1)$ is the wind velocity at the reference height z_1 in the saltation layer, and u_f is the grain settling velocity given by (Jimenez and Madsen, 2003)

$$u_f = \sqrt{\frac{4}{3\,C_d}\,(s-1)\,gd}, \tag{1.36}$$

where C_d is the grain drag coefficient, d is the grain diameter and $s = \rho_g/\rho$ is the grain-fluid density ratio. Both z_1 and α are model parameters: z_1 represents the height at which the wind drag replaces the momentum lost by the grains in the bed collision, whereas α contains information about this momentum loss and represents an effective restitution coefficient.

Inserting Eqs. (1.31), (1.32) and (1.34) into Eq. (1.30) one obtains the saturated flux

$$\begin{aligned} q_s(u_*) &= \frac{2\alpha}{g}\frac{\rho}{\rho_{\text{sand}}}(u_*^2 - u_{*a0}^2)\,u_s, \\ &= \frac{2\alpha}{g}\frac{\rho}{\rho_{\text{sand}}}(u_*^2 - u_{*a0}^2)(v(z_1) - u_f/\sqrt{2\alpha}), \end{aligned} \tag{1.37}$$

which, after substituting explicitely u_{*a0} and v (Eqs. (1.16) and (1.22)), becomes

$$q_s(U) = 2\alpha\mu q_t\,(U-1)((2-\mu)U + \mu)(\beta_0 - \alpha_0 U), \tag{1.38}$$

as a function of the dimensionless shear velocity $U = u_*/u_{*t}$, where

$$q_t \equiv \frac{\rho}{\rho_{\text{sand}}}\frac{u_{*t}^3}{g}, \tag{1.39}$$

and the constants α_0 and β_0 are defined as

$$\alpha_0 = \kappa^{-1}\left[\mu(E_i(z_0/z_m) - E_i(z_1/z_m)) - \ln(z_1/z_0)\right], \tag{1.40}$$

$$\beta_0 = \kappa^{-1}\mu(E_i(z_0/z_m) - E_i(z_1/z_m)) - u_f/(u_{*t}\sqrt{2\alpha}). \tag{1.41}$$

and $\mu = \ln(r\,z_m/z_0)/(E_i(z_0/z_m) - E_i(r))$.

A further simplification is achieved when $\mu \sim 1$, in which case Eq. (1.38) becomes

$$q_s(U) = 2\alpha\mu q_t\,(U^2 - 1)\,f(U), \tag{1.42}$$

with $f(U) \equiv (\beta_0 - \alpha_0\,U)$. The function $f(U)$ assumes other forms in several sand transport works, as sketched in table 1.1. Later we will return to the comparison between the different saturated flux expressions.

Table 1.1: Forms of the function $f(U)$ for different sand flux models (after Sørensen (Sørensen, 2004))

this work	$\beta - \alpha U$
Owen(1964)	$\beta + \alpha U$
Sauermann *et al*(2001)	$\beta + \alpha\sqrt{U^2 + C}$
Ungar and Haff(1987)	β
Kind(1976)	CU

the parameters α, β and C are arbitrary constants.

Estimation of α for rebound grains

The saturated flux defined in Eq. (1.37) has two parameters, z_1 and α, both related with the momentum balance of the grain flow Eq. (1.33). The parameter α acts as an effective restitution coefficient and relates the vertical component of the ejection velocity (u_z^{eje}) with the horizontal velocity difference between the impact and ejection ($u_x^{imp} - u_x^{eje}$). This parameter can be estimated for rebound grains.

Similarly as in Eq. (1.35), for rebound grains α reads

$$\begin{aligned} \alpha &= u_z^{reb}/(u_x^{imp} - u_x^{reb}) \\ &= \gamma \sin\theta_{reb}/(\cos\theta_{imp} - \gamma\cos\theta_{reb}), \end{aligned} \tag{1.43}$$

where $\gamma \approx 0.4$ is the restitution coefficient (Rioual et al., 2000), $\theta_{imp} \approx 10^o$ is the impact angle and $\theta_{reb} \approx 45^o$ is the rebound angle, for grains of diameter $d \approx 250\mu m$ (Anderson and Haff, 1988; Anderson, 1991), yielding $\alpha \approx 0.4$.

Drag coefficient

Before fitting the saturated flux data we need to fix the drag coefficient C_d. In general, C_d is a function of Re. Using for the characteristic velocity the relative velocity $u_f/\sqrt{2\alpha}$ resulting from the momentum balance in Eq. (1.33), the drag coefficient is given by (Jimenez and Madsen, 2003)

$$C_d = \frac{4}{3}\left(A + \sqrt{2\alpha}B/S_*\right)^2, \tag{1.44}$$

where $S_* \equiv \frac{d}{4\nu}\sqrt{gd(s-1)}$ is the fluid-sediment parameter, $A = 0.95$ and $B = 5.12$ for natural sand (Jimenez and Madsen, 2003), and s is the grain-fluid density ratio.

Experimental verification of the saturated flux formula

Above, we obtained the parameters z_0 and $z_m(r)$ (Eq. (1.29) and (1.27)) from the comparison of the roughness length in Eq. (1.24) with experimental data. The remained unknown flux parameters z_1 and α can be then estimated by fitting the saturated flux in Eq. (1.38) with the Iversen and Rasmussen flux data for different grain sizes (Iversen and

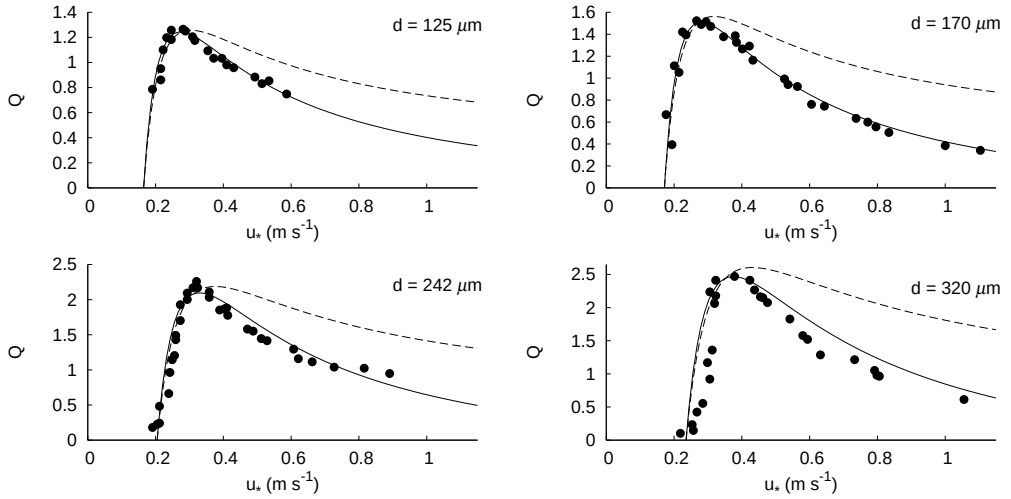

Figure 1.9: Dimensionless saturated flux $Q \equiv q_s(u_*)/(q_t U^3)$ as a function of the shear velocity u_* for different grain diameters, using the data of Iversen and Rasmussen (1999). The lines represent the saturated flux (Eq. (1.38)), with the focal point assumption $r = 1$ (full lines) and without it $r = 0$ (dashed lines). In all cases the best fit was achieved when a focal point is assumed.

Rasmussen, 1999), plotted in Fig. 1.9. For the fitting we use two characteristic values of r, namely 0 and 1.

From the fit we found that $z_1 \approx 3.5$ mm does not depend on the grain diameter, which is the characteristic length of the sand transport, hence it should be written in terms of another lengthscale l_v. By using the particle Reynolds number $R_e = u_{*t} d/\nu$ with the threshold shear velocity $u_{*t} = A\sqrt{dg(s-1)}$, the lengthscale l_v can be defined from $R_e = (d/l_v)^{3/2}$ as

$$l_v \equiv \left(\frac{\nu^2}{A^2\, g(s-1)} \right)^{1/3}. \tag{1.45}$$

The typical value of l_v is about $100\,\mu$ m, therefore

$$z_1 = 35\, l_v. \tag{1.46}$$

The definition of l_v is dimensionally equivalent to the lengthscale $(\nu^2/g)^{1/3}$ defined by Andreotti (Andreotti, 2004) using the air viscosity ν. This lengthscale, together with the timescale t_v in Eq. (1.27), are introduced for two reasons. First, to satisfy the dimensional analysis. Second, to give some insight to the dependences on gravity, and the air viscosity and density, that cannot be checked by direct measurements, but that are central for other planetary physical conditions.

Figure 1.10 shows the best fit values of α for different grain diameters, and also includes the linear fit $\alpha = 1700 m^{-1}\, d$, which can be expressed in terms of the lengthscale l_v as

$$\alpha = 0.17 d/l_v, \tag{1.47}$$

which gives $\alpha = 0.42$ for $d = 250\mu$ m, a very similar value to that estimated for rebound grains in Eq. (1.43).

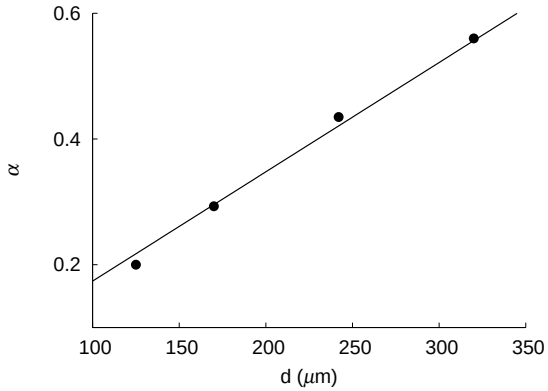

Figure 1.10: The values of α estimated from the flux data (Iversen and Rasmussen, 1999). Solid line shows the linear regression.

Surprisingly, both parameters z_1 and α seem to be independent on the ratio $r \equiv \bar{z}/z_m$, whose main effect is to change the scaling exponent in the saturation flux $q_s(u_*)$ at large u_*. In fact, the value of this exponent depends on the relation between the two characteristic heights of the model, z_1 and $\bar{z}$. When $\bar{z} = z_1$ then $\alpha_0 = 0$ in Eq. (1.40 and q_s scales as u_*^2, as in the Ungar and Half model (Ungar and Haff, 1987; Almeida et al., 2006). On the other hand, for $\bar{z} < z_1$ then $\alpha_0 < 0$ and q_s increases faster than u_*^2, as in the other models (Owen, 1964; Sauermann et al., 2001). Finally, for $\bar{z} > z_1$, q_s increases slower than u_*^2, as in the Iversen and Rasmussen data (Iversen and Rasmussen, 1999), with an exponent between 1.8 and 2.0 (figure 1.9: full lines).

1.3 Modeling of sand dunes: the DUNE model

In this section we describe the full model for sand dunes, including previous achivement (Sauermann et al., 2001; Kroy et al., 2002; Schwämmle and Herrmann, 2005a) and the new sand transport model presented in the previous section.

The modeling of dunes involves three main stages: (i) a calculation of the wind considering the influence of the topography, (ii) a calculation of the sand flux carry by the perturbed wind, and finally (iii) the evolution of the sand surface due to sand erosion, deposition and avalanches. Once the wind starts to blow, it is deformed by the surface topography experiencing a speedup on positives slopes and a slowdown on negatives ones. This spatial perturbation of the wind velocity leads to an inhomogeneous sand flux. Therefore, based on erosion and deposition processes driven by the increase or decrease of the sand flux in the transport direction, the sand surface changes. This topographic change in turn induces a new perturbation on the wind field and the whole cycle repeats again.

The coupling sand surface evolution and aeolian sand transport involves two different time scales related, on one hand, to erosion and deposition processes that change the surface, and, on the other hand, to sand transport and wind flow. A significant change in sand surface can happen within some hours or even days. In contrast, the time scale of wind flow changes and saltation process is much faster, of the order of seconds. This separation of time scales leads to an enormous simplification because it decouples the different processes. Therefore, we can use stationary solutions for the wind surface shear velocity u_* and for the resulting sand flux $\mathbf{q}$, and later use them for the time evolution of the sand surface $h(x, y)$.

1.3.1 Wind model

As was shown in the previous section, the sand transport rate is determined not by wind velocity, which change with the height, but rather by the shear velocity which encodes the friction forces at the surface. The surface shear velocity not only changes with the sediment transport via the feedback effect, but also with the terrain topography. It is well known that a uphill induces a wind speedup while a downhill produces a wind slowdown. This change in the wind velocity is crucial for the understanding of dune formation and migration.

We consider a low and smooth topographic accident $h_s(x, y)$, like a hill or a sand dune, which induces a small perturbation $\delta\mathbf{v}(x, y, z)$ in the wind velocity profile, namely

$$\mathbf{v}(x, y, z) = \mathbf{v}_0(z) + \delta\mathbf{v}(x, y, z). \tag{1.48}$$

where $\mathbf{v}_0(z)$ is the unperturbed wind velocity profile.

From the Prandlt turbulent closure in Eq. (1.1) a velocity perturbation leads to a modification of the surface shear stress $\boldsymbol{\tau}_0$ over a flat bed given by

$$\boldsymbol{\tau}(x, y) = \boldsymbol{\tau}_0 + |\boldsymbol{\tau}_0|\delta\boldsymbol{\tau}(x, y) \tag{1.49}$$

where $\delta\boldsymbol{\tau}(x,y)$ is the shear stress perturbation at the surface $h_s(x,y)$. From now on subscript '0' means values on a flat bed.

The shear stress perturbation $\delta\boldsymbol{\tau}$ is computed according to an analytical work describing the influence of a low and smooth hill in the wind profile and shear stress (Jackson and Hunt, 1975; Hunt et al., 1988; Weng et al., 1991). In the fourier space this perturbation is given by the functions $\delta\tilde{\tau}_x(\mathbf{k})$ and $\delta\tilde{\tau}_y(\mathbf{k})$ which are the Fourier-transformed components of the shear stress perturbation in the unperturbed wind direction, defined by the direction of the wind velocity $\mathbf{v}_0$ on a flat bed, by definition the x-direction, and in transverse direction y respectively,

$$\begin{aligned}
\delta\tilde{\tau}_x(\mathbf{k}) &= \frac{2\tilde{h}_s(\mathbf{k})}{U^2(l)}\frac{k_x^2}{|\mathbf{k}|}\left\{-1+\left(2\ln\frac{l}{z_0'}+\frac{|k|^2}{k_x^2}\right)\sigma\,\frac{K_1(2\sigma)}{K_0(2\sigma)}\right\},\\
\delta\tilde{\tau}_y(\mathbf{k}) &= \frac{2\tilde{h}_s(\mathbf{k})}{U^2(l)}\frac{k_x\,k_y}{|\mathbf{k}|}\,2\sqrt{2}\,\sigma K_1\big(2\sqrt{2}\,\sigma\big)\,,
\end{aligned} \tag{1.50}$$

where $\sigma=\sqrt{i\,L\,k_x\,z_0'/l}$. Here, K_0 and K_1 are modified Bessel functions, k_x and k_y are the components of the wave vector $\mathbf{k}$ in Fourier space, and $\tilde{h}_s$ is the Fourier transform of the height profile. The constant $U(l)\equiv v(l)/v(h_m)$ is the dimensionless vertical velocity profile at the height l which is the depth of the inner layer of the flow, i.e, the layer at which the change in the shear stress significantly affects the mean flow $\mathbf{v}_0$. Function $U(l)$ is suitably nondimensionalized by the velocity $v(h_m)$ at the middle layer height h_m where the mean flow over the terrain is not affected by changes in the shear stress. Therefore, from the logarithmic velocity profile in the boundary layer

$$U(l)\equiv\frac{\ln\left(l/z_0'\right)}{\ln\left(h_m/z_0'\right)} \tag{1.51}$$

Here both, l and h_m, are computed from the implicit equations

$$l\,\ln\left(l/z_0'\right) = 2\,\kappa^2 L \tag{1.52}$$

$$h_m^2\,\ln\left(h_m/z_0'\right) = L^2 \tag{1.53}$$

where κ is the von Kármán constant, z_0' the apparent roughness length which takes into account saltation (see Eq.(1.14) and L is the typical length scale of the hill. This length is defined as the mean wavelength of the Fourier representation of the height profile

$$L\equiv\frac{1}{\langle k_x\rangle}\equiv\frac{\int_0^\infty d\mathbf{k}|\tilde{h}_s(\mathbf{k})|}{\int_0^\infty d\mathbf{k}k_x|\tilde{h}_s(\mathbf{k})|} \tag{1.54}$$

By inserting the inverse Fourier-transform of Eq. (1.50) into Eq. (1.49) one obtains the modified shear stress, which in terms of the shear velocity reads

$$\mathbf{u}_*(x,y)=u_*(x,y)\,\mathbf{e}_\tau(x,y) \tag{1.55}$$

where the unity vector $\mathbf{e}_\tau\equiv\boldsymbol{\tau}/|\boldsymbol{\tau}|$ defines the actual wind direction and the perturbed shear velocity is

$$u_*(x,y)\approx u_{*0}\sqrt{1+\delta\tau_x(x,y)}. \tag{1.56}$$

Here $u_{*0}=\sqrt{\tau_{*0}/\rho}$ denotes the unperturbed shear velocity in a flat bed.

Separation Bubble

The formalism for computing the surface wind perturbation does not include nonlinear effects like flow separation and, therefore, it is only valid for smooth surfaces. However, in sand dunes the brink line not only divides the face where avalanches occurs from the rest of the dune, but also, since the repose angle of sand ($\sim 34^o$) represents the highest slope in the dune surface, it establishes a limit at which the wind streamlines separate from the surface (see Fig. 1.3). Therefore the above model cannot be used for mature sand dunes with slip faces. One solution for this problem, as was suggested by (Zeman and Jensen, 1988) and fully developed by Sauermann et al. (Sauermann, 2001), is to calculate the wind perturbation (Eq. (1.50)) over an ideal smooth surface $h_s(x, y)$ that comprise the profile $h(x, y)$ of the dune and the so called *separation bubble* $s(x, y)$.

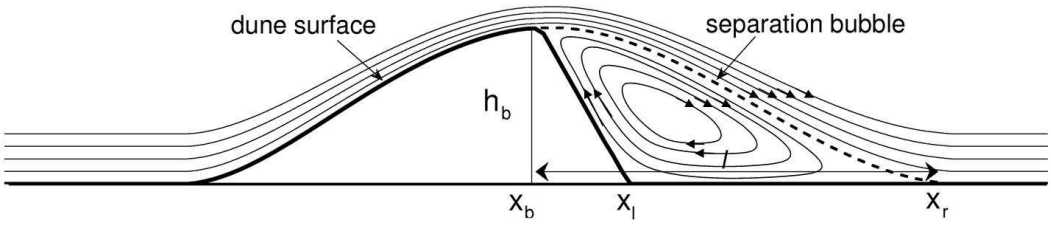

Figure 1.11: Sketch of the central slice of a barchan dune along with its separation bubble. In the ideal case the flow separation generates a rotational flow in the region inside the bubble with a negible sand transport.

The separation bubble is defined as the surface that limits the region of recirculating flow after the brink that results from flow separation (see Fig. 1.11). In this region the flow is strongly depressed and thus sand transport can be neglected in first approximation.

Following the Sauermann approach (Sauermann et al., 2001) each slice of the surface of the bubble should resembles the separating streamline shape and is modelled by a third-order polynomial so that in the case of a barchan the region between the horns is inside the bubble (Fig. 1.12). The coefficients of this polynom arise from the continuity of both surfaces at the brink line $h(x_b(y)) \equiv h_b(y)$, where $x_b(y)$ is the x-position of the brink for each slice y (see Fig. 1.11), $s(x_b(y), y) = h_b(y)$, the continuity of the first derivatives at the brink, $s'(x_b(y), y) = h'(x_b(y)) \equiv h'_b(y)$, and the smooth conditions $h_s(x_r(y)) = 0$ and $h'_s(x_r(y)) = 0$ at the re-attachment line $x_r(y)$, where flow re-attach to the surface again. Therefore, the separation bubble is given by

$$\begin{aligned} s(x,y) &= a_3(y)\,(x - x_b(y))^3 + a_2(y)\,(x - x_b(y))^2 + h'_b(y)(x - x_b(y)) + h_b(y) \\ a_3(y) &= (2h_b(y) + h'_b(y)\,l(y))/l(y)^3 \\ a_2(y) &= -(3h_b(y) + 2h'_b(y)\,l(y))/l(y)^2 \end{aligned} \tag{1.57}$$

Here, the reattachment length $l(y) \equiv x_r(y) - x_b(y)$ for each slice y (Fig. 1.11), is obtained from the assumption that the separation surface has a maximum slope c, thus

$$l(y) \approx \frac{3h_b(y)}{2c}\left(1 + \frac{h'_b(y)}{4c} + 2\left(\frac{h'_b(y)}{4c}\right)^2\right) \tag{1.58}$$

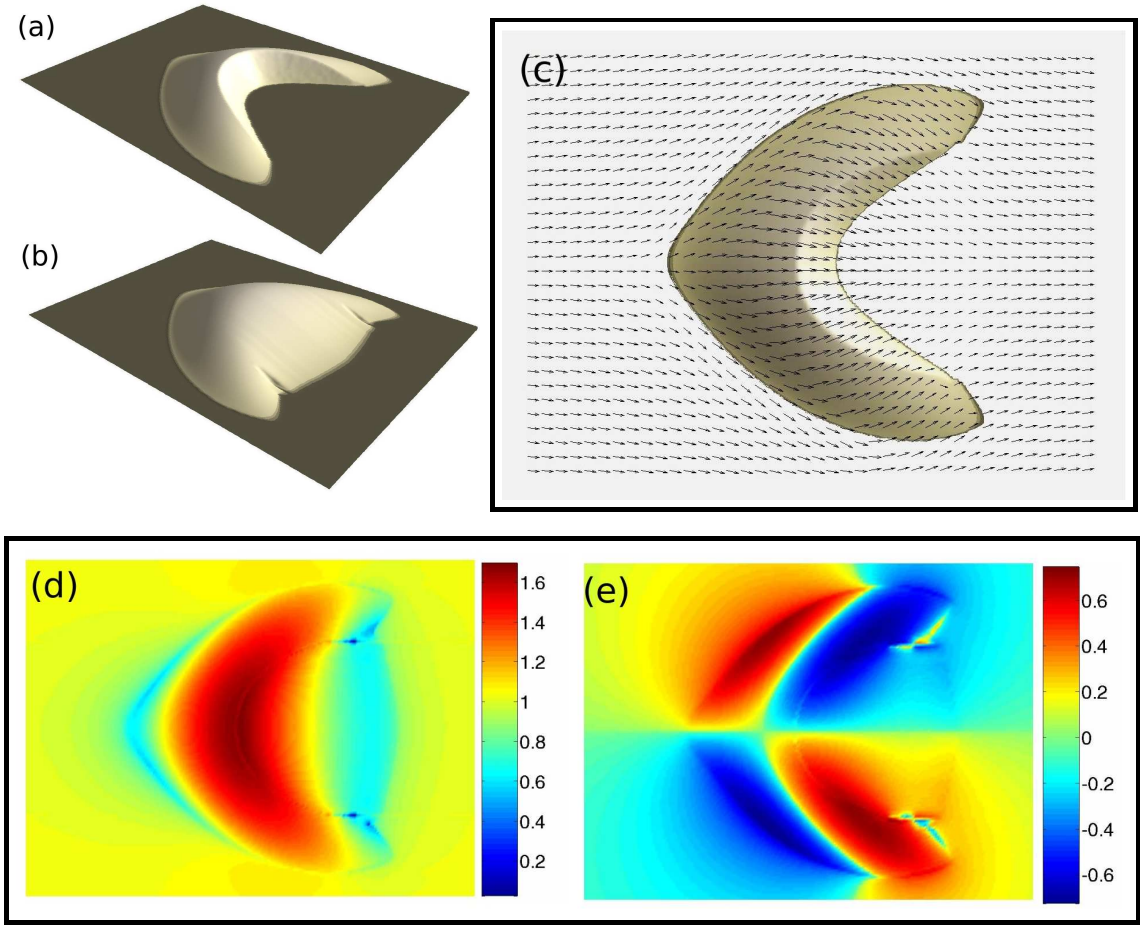

Figure 1.12: Simulated barchan dune (a) and its separation bubble (b). The normalized wind shear velocity $\mathbf{u}_*/u_{*0}$ (Eq. 1.55) over a barchan dune including the separation bubble (b), is plotted in (c). Note that u_* is proportional to the wind velocity field at a fixed height. Both component u_{*x} and u_{*y} are included in (d) and (e) for comparison.

Figure 1.12a and 1.12b show a simulated barchan dune without and with the separation bubble, respectively. The resultant surface $h_s(x,y) \equiv \max(h(x,y), s(x,y))$ is then used to calculate the wind shear velocity perturbation on a barchan dune according to Eqs. (1.55) and (1.50), as depicted in Fig. 1.12c. The dune topography induces two kind of variations on the wind shear. First a variation in the strength: at the dune's foot, wind experiences a slowdown, followed by a speedup at the windward side and later again a slowdown at dune's horns (see the x-component of the wind, Fig. 1.12d). And, second, a variation in wind direction since wind is forced to surround the dune, as shows Fig. 1.12e.

Finally, based on the flow separation at the brink, we set the shear velocity to zero below the separation bubble, i.e. $u_*(x,y) = 0$ for $h(x,y) < h_s(x,y)$.

The corresponding new shear velocity $\mathbf{u}_*(x,y)$ is used afterwards to calculate the sand transport on the surface $h(x,y)$.

1.3.2 Three dimensional sand transport model

In this section we extend the sand transport model derived in section 1.2 for two dimmensions, suitable when sand transport takes place on a flat bed, to three dimmensions, which is the case when sand transport occurs over a dune surface and gravity force is taken into account.

Characteristic velocity of sand grains

From the shear velocity, the modification of the air flow due to the presence of saltating grains is accounted for. From the section 1.2 we know that within the saltation layer the feedback effect of sand transport results in an effective wind velocity driving the grains. This effective wind velocity v_{eff} is given by the wind velocity $v(x, y, z_1)$ (Eq. (1.22)) at a reference height z_1, namely

$$v_{\text{eff}}(x,y) = \frac{u_*(x,y)}{\kappa}\left[\ln\frac{z_1}{z_0} - \mu\left(1 - \frac{u_{*t}}{u_*(x,y)}\right)\left(E_i\left(\frac{z_0}{z_m}\right) - E_i\left(\frac{z_1}{z_m}\right)\right)\right], \quad (1.59)$$

where $E_i(z)$ accounts for the exponential integral Eq. (1.20). We assume as a first approximation no focal point ($\bar{z} = 0$), yielding $r = 0$ and $\mu = 1$. Therefore, taking into account the range of the characteristic height of the saltation layer $z_m \sim 20$ mm (Eq. (1.27)), the grain based roughness length $z_0 \sim 10\,\mu$ m (Eq. (1.29)) and the reference height $z_1 \sim 3$ mm, the effective wind velocity can be approximated as

$$v_{\text{eff}}(x,y) \approx \frac{u_{*t}}{\kappa}\left(\ln\frac{z_1}{z_0} + \frac{z_1}{z_m}\left(\frac{u_*(x,y)}{u_{*t}} - 1\right)\right), \quad (1.60)$$

The collective motion of sand grains in the saltation layer is characterized by their horizontal velocity u_s at the reference height z_1, which for simplicity is called sand grain velocity however it is referred to the total grain horizontal motion and not to individual grains. In the saturated state this velocity is determined from the momentum balance between the drag force acting on the grains, the loss of momentum when they splash on the ground, and the downhill gravity force (Sauermann et al., 2001; Kroy et al., 2002)

$$\frac{(\mathbf{v}_{\text{eff}} - \mathbf{u}_s)|\mathbf{v}_{\text{eff}} - \mathbf{u}_s|}{u_f^2} - \frac{\mathbf{u}_s}{2\alpha|\mathbf{u}_s|} - \boldsymbol{\nabla} h = 0, \quad (1.61)$$

where $\mathbf{v}_{\text{eff}} \equiv v_{\text{eff}}\mathbf{e}_\tau$ and u_f is the grain settling velocity defined by Eq. (1.36). Note that this equation reduces to Eq. (1.33) for a flat surface when $\boldsymbol{\nabla} h = 0$.

For step surfaces Eq. (1.61) must be solve numerically. However, since dunes has not slopes exceeding the repose angle of sand ($\approx 34^o$), the sand transport direction $\mathbf{u}_s/|\mathbf{u}_s|$ in the friction term can be approximated by the wind direction $\mathbf{e}_\tau$. In this case the sand grains velocity is given by

$$\mathbf{u}_s \approx \left(v_{\text{eff}} - \frac{u_f}{\sqrt{2\alpha}A}\right)\mathbf{e}_\tau - \frac{\sqrt{2\alpha}\,u_f}{A}\boldsymbol{\nabla} h \quad (1.62)$$

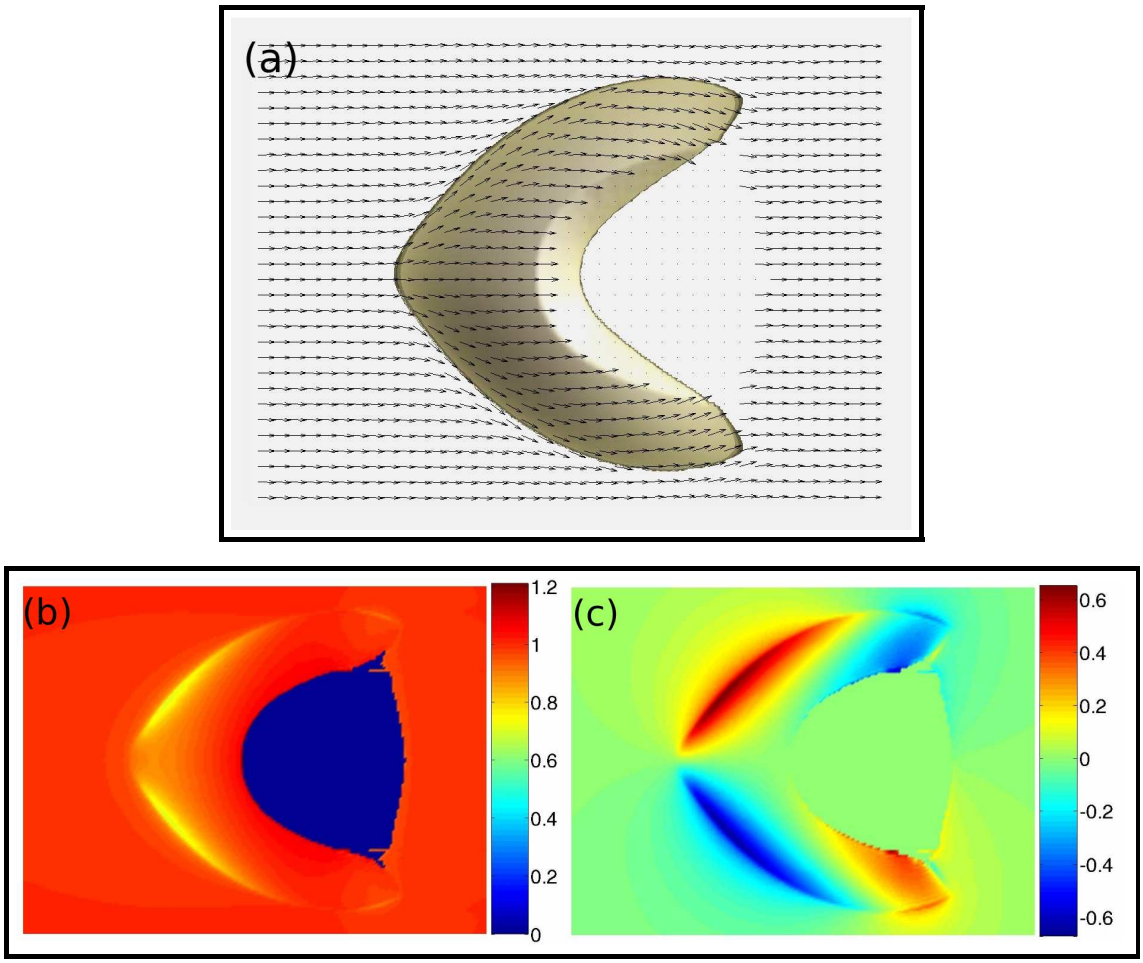

Figure 1.13: (a) Vector diagram of the normalized characteristic sand grains velocity $\mathbf{u}_s/u_{s0}$ (Eq. (1.62)) over a barchan dune. The two components are plotted in (b), x-component, and (c), y-component. Inside the separation bubble, the region after the brink and between the horns, $u_s = 0$ and there is no sand motion. The normalization constant is defined as $u_{s0} \equiv u_s(u_{*0})$ and represents the sand velocity on a flat bed.

where $A \equiv |\mathbf{e}_\tau + 2\alpha\boldsymbol{\nabla}h|$. From this equation, the sand velocity in the saturated state has two terms. The first one points toward the wind direction and represents a small correction of Eq. (1.34), while the second one is directed along the surface gradient. Both terms account for the competing effects of wind blown and gravity on the motion of sand grains. Figure 1.13 shows the characteristic horizontal velocity of sand grains over a barchan dune. Note the strong deviation of the sand flux at the dune's base and the 'trap' effect of the slip face due to flow separation at the brink. The trapped grains accumulate on the top of the slip face before falling down in avalanches.

Saltation flux

From Eq. (1.37) and (1.61) we obtain the saturated sand flux q_s over an irregular sand surface $h(x, y)$, as an extention of Eq. (1.37), which gives the saturated sand flux q_s over

a flat bed. However, how the sand flux reach the saturated state from a given initial or boundary value?

From the first section we know that in one hand the saltation sand flux over a sand bed can increase due to the cascade of splashed grains that enter to the flow, while in the other hand, it cannot unlimited grow due to the feedback effect of the grain motion on the wind shear. Therefore, Sauermann et al. proposed a transport equation that describes the spatial evolution of the saltation sand flux $q \equiv |\mathbf{q}|$ (Sauermann et al., 2001)

$$\nabla \cdot \mathbf{q} = \frac{q}{l_s}\left(1 - \frac{q}{q_s}\right)\begin{cases}\Theta(h) & q < q_s \\ 1 & q \geq q_s\end{cases}, \tag{1.63}$$

where $q_s \equiv |\mathbf{q}_s|$ is the saturated sand flux and l_s is the characteristic length for saturation and thus is called 'saturation length'. From Eq. (1.63) the spatial change of sand flux for small values of q is driven by the exponential growth term q/l_s, with the characteristic length l_s, while for values of q close to the maximum q_s, the second term $1 - q/q_s$ leads to a saturated state. Symbol $\Theta(x)$ represents the Heaviside function, and guarantees that if there is no sand available ($h = 0$) an undersaturated sand flux $q < q_s$ cannot increase.

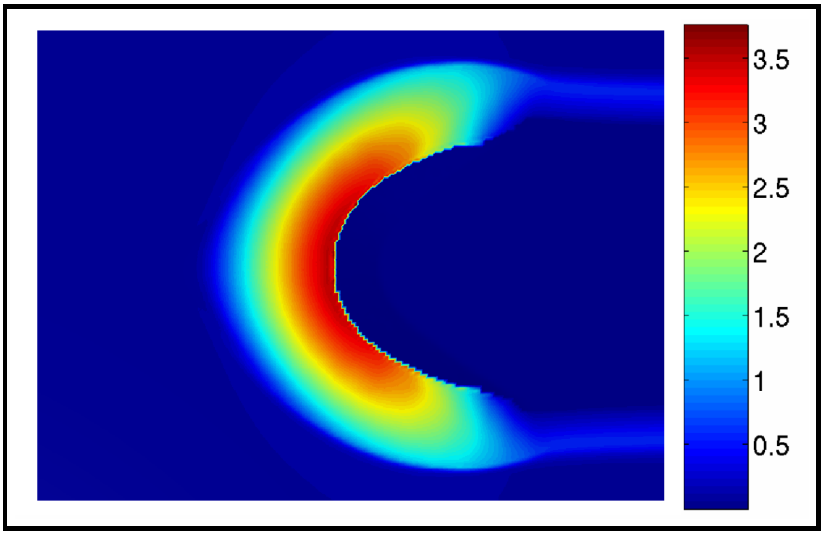

Figure 1.14: Normalized saltation sand flux q/Q over a barchan dune due to the wind field depicted if Fig. 1.12. Wind blown from left to right carrying a normalized influx equal to 0.1.

Both, the saturated sand flux and the saturation length are given by

$$\mathbf{q}_s(u_*) = \frac{2\alpha}{g}\frac{\rho}{\rho_{\text{sand}}}\left(u_*^2 - u_{*t}^2\right)\mathbf{u}_s \tag{1.64}$$

$$l_s(u_*) = \frac{2\alpha|\mathbf{u}_s|^2}{\gamma g}\frac{1}{(u_*/u_{*t})^2 - 1}. \tag{1.65}$$

where α is the effective restitution coefficient given by Eq. (1.47) and γ is a model parameter accounting for the splash process (Sauermann, 2001). From now on we denote the saturated flux over a flat bed as $Q \equiv q_s(u_{*0})$.

Figure 1.14 depicts the normalized saltation sand flux q/Q over a barchan dune that results from solving Eq.(1.63) with an imposed boundary condition. In this case we impose a small influx $q_{in} = 0.1\,Q$. In the figure, the barchan dune is surrounded by a flat rocky surface. Therefore, the sand flux remains constant until it reaches the sand surface. Afterwards, flux increases following the trend of the wind shear velocity u_* (see Fig. 1.12) i.e. the flux increases in the windward side of the dune and decreases in the dune's horns, while in the region covered by the separation bubble (the slip face and between the horns) there is no sand motion and thus no sand flux.

1.3.3 The time evolution of the surface

The spatial change of the sand flux showed in Fig. 1.14 and described by the logistic sand transport Eq. (1.63) defines the temporal change of the sand profile $h(x, y)$. According to the mass conservation

$$\begin{aligned} \frac{\partial h}{\partial t} &= -\nabla \cdot \mathbf{q} \\ &= -\frac{q}{l_s}\left(1 - \frac{q}{q_s}\right) \begin{cases} \Theta(h) & q < q_s \\ 1 & q \geq q_s \end{cases} \end{aligned} \tag{1.66}$$

Therefore, wherever sand flux is undersaturated ($q < q_s$), erosion takes place and by definition $(\partial h/\partial t) < 0$, since wind can still increase the amount of sand it can carry. Otherwise, in the oversaturation ($q > q_s$), the amount of sand wind carry is beyond its limits and deposition occurs ($(\partial h/\partial t) < 0$).

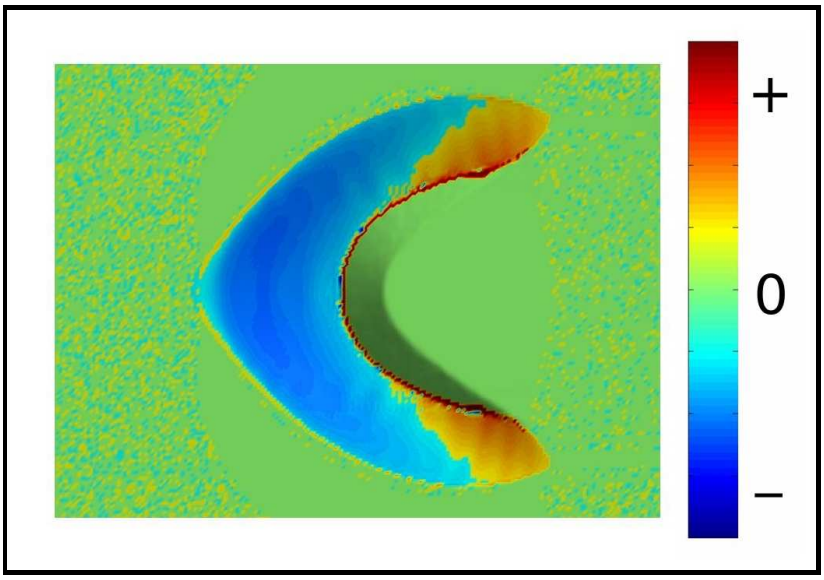

Figure 1.15: Sand erosion (+) and deposition (-) pattern on a barchan dune. Note that sand is eroded from the dune's windward side while it is trapped by the slip face or deposited on the horns.

Figure 1.15 shows the sand erosion-deposition pattern over a barchan dune. This pattern clearly divides the dune into two parts, the windward side where erosion takes place and the dune's lee side, comprising the slip face and the horns, where sand is deposited. Furthermore, through erosion-deposition process given by Eq. (1.66) the dunes are by definition not static but dynamics objects. They are essentially sculpted by the wind on the surface, which takes sand from one place to other following certain rules. This explains how a milimeter scaled process like sand transport by saltation can produce structures like dunes. It is not the transport mechanisms but the wind field in its interdependence with the surface shape, which drives to dunes formation and evolution.

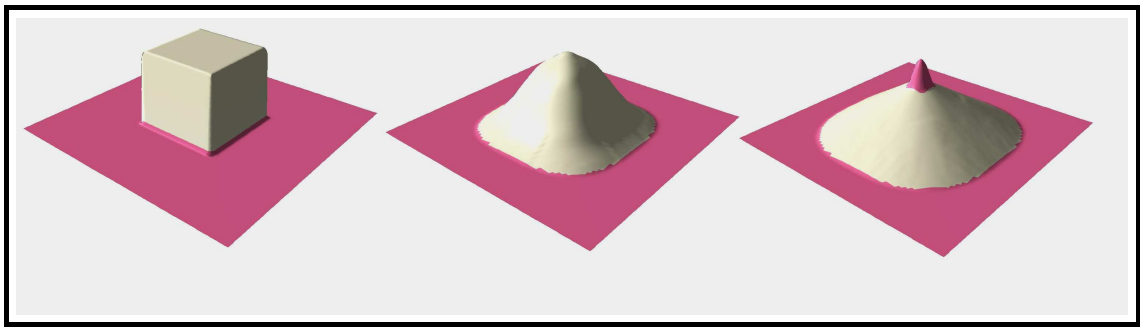

Figure 1.16: A sand cube (yellow) that contains a rocky gaussian inside (red) relax through avalanches toward a conical surface.

1.3.4 Avalanches

The evolution of a sand surface is determined, as was previously shown, by the aeolian erosion-deposition process, as a consequence of the inhomogeneity of the sand flux over the surface. However, in the slip face below the separation bubble there is no sand transport, therefore, sand grains accumulate there, after crossing the brink (this sand accumulation at the brink is shown by the red line in Fig. 1.15). In this region a non-aeolian mechanisms of sand transport takes place, namely, sand avalanches. In modeling the surface relaxing by avalanches we follow the simple approach of Hersen et al.(Hersen, 2004), instead of the model used by Bouchaud and co-workers (Bouchaud et al., 1994; Bouchaud, 1998).

Taking into account that the characteristic time of avalanches events is orders of magnitude smaller than the characteristic time involved in the whole surface evolution, we consider an effective model that instantaneously relax the gradient of the sand surface toward the sand repose angle. If the slope of the sand surface exceeds the static angle of repose, sand is redistributed according to the sand flux

$$\mathbf{q}_{\text{aval}} = E\ (\tanh|\nabla h| - \tanh(\tan\theta_{\text{dyn}})\ \frac{\nabla h}{|\nabla h|} \tag{1.67}$$

Afterwards, using this flux, the surface is repeatedly changed according to Eq. (1.66), until the maximum slope lies below the dynamic angle of repose, θ_{dyn}. We include the hyperbolic tangent function to improve convergence.

Figure 1.16 shows a extreme example of the avalanches model: the evolution of a sand cube due to avalanches.

1.3.5 Model parameters

Wind model

Our wind model, Eqs. (1.50), (1.55) and (1.56), has only two parameters, the apparent roughness length z_0' (Eq. (1.14)) and the shear velocity u_{*0} over a flat bed. The first one is fixed to the value $z_0' = 1$ mm, which coincides with the peak value of the roughness length curve in Fig. 1.7 for the characteristic grain diameter in sand dunes $d \approx 0.25$ mm (Fig. 1.4). The unperturbed shear velocity u_{*0} is defined by the initial condition (see below).

Separation bubble model

The model for the separation bubble, Eqs. (1.57) and (1.58), only has one parameter, the maximum slope c allowed for the separation surface $s(x, y)$, which is fixed to the value $c = 0.2$, smaller than the value assigned by Sauermann ($c = 0.25$) corresponding to an maximum angle of 14^o (Sauermann, 2001). We select $c = 0.2$ after perform calculations of wind profiles over real Maroccan dunes.

Sand transport model

The sand transport model, Eqs. (1.60), (1.61), (1.63) and (1.64), has five parameters. Four of them, z_0, z_m, z_1 and α, are given in section 1.2 in terms of the grain density $\rho_g \approx 2650$ kg/m^3, grain diameter $d \approx 0.25$ mm, air density $\rho \approx 1.225$ kg/m^3, air kinematic viscosity $\nu \approx 1.5\,10^{-5}$ m^2/s, gravity acceleration $g \approx 9.8$ m/s^2 and drag coefficient C_d, and thus they are not free parameters. The last one is $\gamma \approx 0.2$ (Sauermann et al., 2001).

Avalanches model

The only free parameter in the model for avalanches Eq. (1.67) is E which has dimmension of flux. After some test of convergence we select the value $E = 0.9$ kg/ms. Of course, since the avalanches are modelled just as a slope relaxation, the value of E has no physical meaning. The other two parameters are the static $\theta_{\text{stat}} \approx 34^o$ and dynamic angle of repose $\theta_{\text{dyn}} \approx 33^o$ for sand.

1.4 Barchan dune simulations

In this section we study barchan dunes through numerical simulations and present some scaling relations between the barchan volume, velocity and flux balance with their size. Comparing these scaling laws with measured data we validate the predictions of the DUNE model including the new sand transport model and the corresponding parameters.

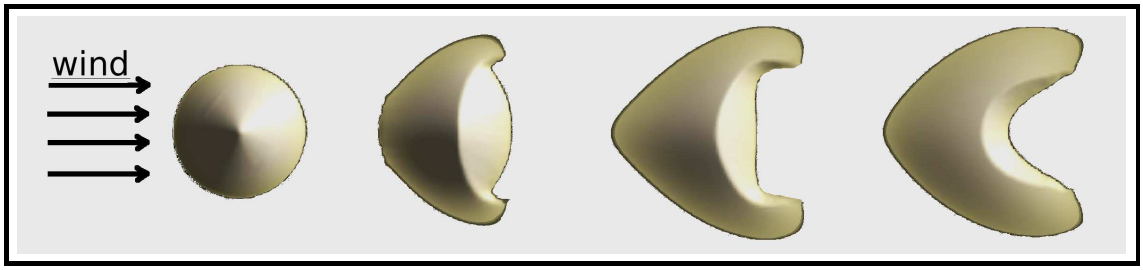

Figure 1.17: Formation of a 6 m high barchan dune from an initial sand pile after ~ 1 year of constant wind blow.

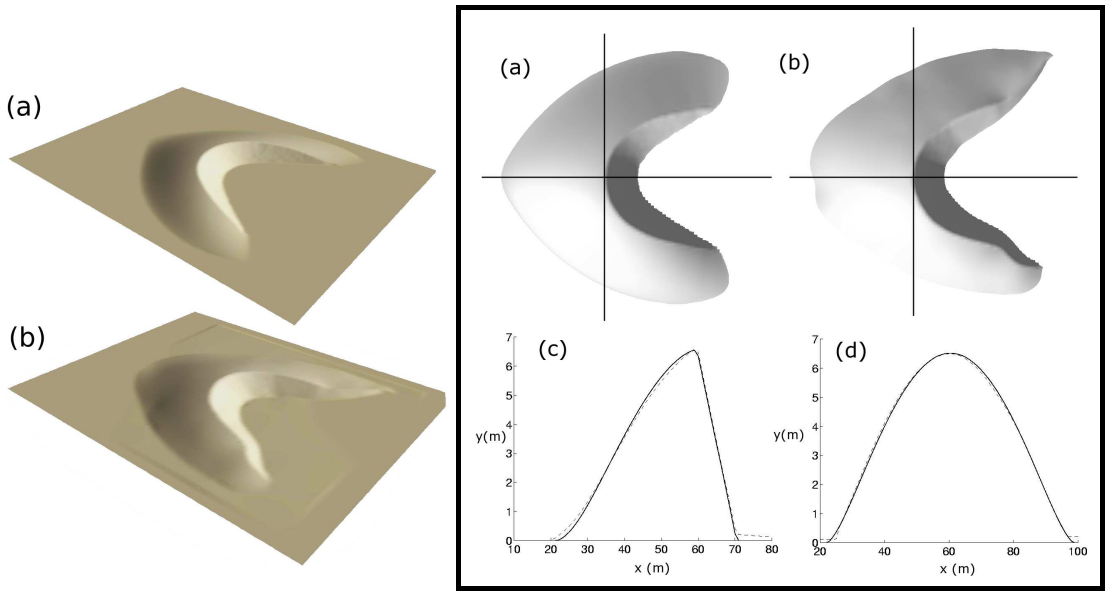

Figure 1.18: Comparison between a 6 m high simulated barchan (a) and a measured one (b). In (c) and (d) are shown the longitudinal (c) and transversal (d) central slides of both, the simulated and the measured dune. Dashed-lines slices correspond to a measured barchan, whereas the full lines to a simulated one. Both dunes have the same scale.

Barchans are isolated sand dunes that emerge when wind is uni-directional and sand is sparce (see Fig. 1.3). Under these conditions the barchan shape represents the equilibrium shape toward which any initial sand surface over a non-erodible substract evolves. They arise from the numerically integration of the equations (1.55), (1.63) and (1.66) for a given initial surface, an unperturbed shear velocity u_{*0}, oriented along the x-direction, and a constant influx q_{in} at the input boundary $x = 0$. Since u_{*0} univocally defines the

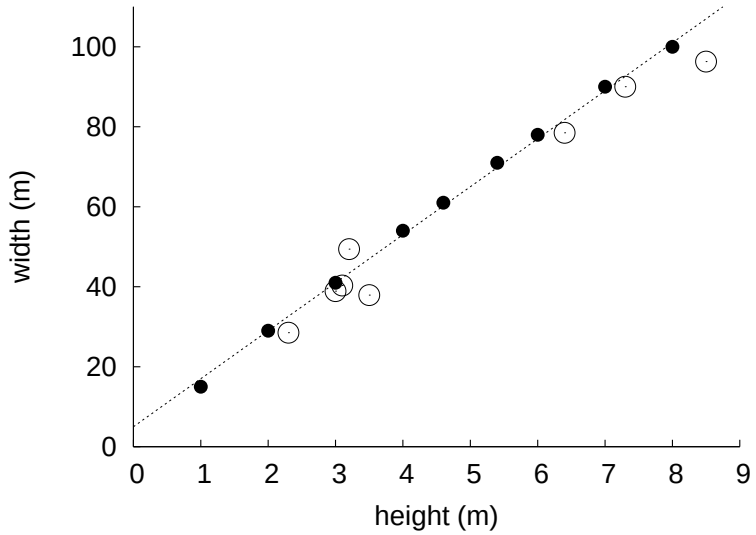

Figure 1.19: Height H and width w relationship of the measured dunes in Morocco by Sauermann (white circles) and of the simulated dunes (black circles) with the linear regression $w = 12\,H + 5$ m.

maximum sand flux Q over a flat bed, we can use either u_{*0} or Q to characterize the unperturbed wind.

Therefore, for simulations one uses only two free parameters, the sand supply, encoded in q_{in}, and the wind strength, encoded in u_{*0} or $Q(u_{*0})$.

Figure 1.17 depicts the evolution of the profile $h(x, y)$ of a sand pile towards a barchan dune, while Fig. 1.18 compares the 3-dimensional characteristic 'C' shape of a simulated and a measured Maroccan barchan (Sauermann et al., 2000). Both dunes are very similar except at the horns. This typical simulation was performed using zero influx $q_{in} = 0$ and a flat bed shear velocity $u_{*0} = 0.4$ m/s, a realistic value for dune fields (Sauermann et al., 2003).

Morphologic relationships

The morphology of a barchan dune is characterized by well known linear scalings between the dune's width W, total length L, windwards side length L_w, mean horns length L_h and the dune's height H (Finkel, 1959; Hastenrath, 1967; Hastenrath, 1987; Lettau and Lettau, 1969; Sauermann et al., 2000; Sauermann et al., 2001; Schwämmle and Herrmann, 2005a).

Figure 1.19 shows one of these scalings, the width-height relationship, which follows the general equation $w = a_w H + b_w$ (Sauermann, 2001). Therefore, the barchan shape is only scale invariant for large sizes, i.e. the ratio $H/w = H/(a_w\,H + b_w)$ tends to the constant $1/a$ at large H. However, for small sizes, $H < 5\,b_w/a_w \sim 2$ m, the barchan shape is size dependent. This rupture of the scale invariance at small sizes is a consequence of the

saturation length l_s given in Eq. (1.64) (Kroy et al., 2002; Andreotti et al., 2002b). The saturation length also determines the minimal size for barchan dunes (Parteli et al., 2006).

Velocity

Since the pioneer work of Bagnold (Bagnold, 1941) it is also well known that the barchan velocity v scales with the inverse of its size and is proportional to the saturated flux Q on a flat bed. However, although the relationship between v with Q is well stablished, there is still a debate about which size one should use. Bagnold showed (Bagnold, 1941), through a simple mass conservation analysis, that v scales with the inverse of the dune's height, namely $v \propto 1/H$. Alternatively, other authors propose a scaling with the dune's length (Sauermann, 2001; Schwämmle and Herrmann, 2005a), or a more complex relation of the type $v \propto 1/(H + H_0)$ to fit dune measurements (Andreotti et al., 2002b; Hersen et al., 2004; Elbelrhiti et al., 2005).

The idea of Bagnold's scaling arises from the travel wave solution $h(x-vt, y)$ of a barchan dune. In fact, by substituting this solution into the mass conservation Eq. (1.66), the dune profile $h(x, y)$ satisfies the travel equation

$$v\frac{\partial h(x,y)}{\partial x} = \nabla \cdot \mathbf{q}(x,y). \tag{1.68}$$

Considering Eq. (1.68) at the central slice of a barchan, namely at $h(x, 0)$, the barchan shows specular symmetry ($h(x, y) = h(x, -y)$) and assuming that $\partial q_y/\partial y \ll \partial q_x/\partial x$, one arrives to the simple balance equation

$$v\frac{\partial h(x,0)}{\partial x} = \frac{\partial q_x(x,0)}{\partial x} \tag{1.69}$$

which implies, after integration, that the x-component of the sand flux obeys h, i.e. $q = q_{in} + v\,h$. Therefore, at dune's crest ($h = H$) it follows that $q_M = q_{in} + v\,H$, from which is obtained the dune velocity scaling

$$v = \frac{q_M - q_{in}}{H} \tag{1.70}$$

$$\propto \frac{Q}{H} \tag{1.71}$$

where one considers that the flux q scales with Q.

Using simulated barchans we find that the velocity v scales with the inverse of their width w, as shown in Fig. 1.20. Therefore, we consider

$$v \approx \alpha\, Q/w \tag{1.72}$$

with the constant $\alpha \approx 50$ in very good agreement with previous studies (Hersen and Douady, 2005). Taking into account the morphological relationship of barchans, both, its length L and width w scale with the height H as $H + H_0$, where H_0 is different in both cases. Therefore, in a certain way all these scalings are equivalent.

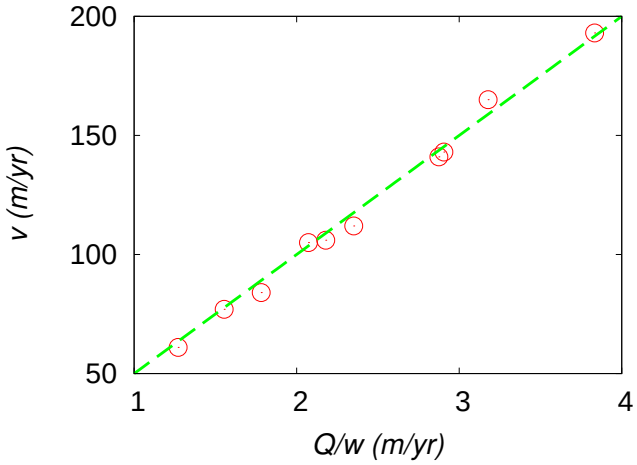

Figure 1.20: Barchan dune velocity as a function of the ratio Q/w.

The propagation velocity given in Eq. (1.72) defines the characteristic time of the barchan motion, called the turnover time t_t, which is defined as the time taken by the dune to travel its own size:

$$t_t \equiv \frac{w}{v} \approx \frac{w^2}{\alpha\, Q}. \tag{1.73}$$

The turnover time t_t is also the typical period of the cycle of motion of a single grain, since it is captured by the slip face until it reappears at the foot of the windward side. In real conditions $t_t \sim 2$ years for the 6 m high barchan showed in Fig. 1.18.

1.4.1 Stability

From the dynamical point of view the stability of barchan dunes is a particular important question. Based on previous simulations it has been predicted that barchan dunes are intrinsically unstable (Sauermann, 2001; Hersen et al., 2004). Here, we describe how this instability arise for barchans simulated with the DUNE model.

Flux balance in a barchan dune

In order to illustrate the dune size instability we analyze the flux balance equation. A barchan dune can be seen as an object that captures some amount of sand from the windward side and releases another amount from the horns while trapping a fraction at the slip face (Fig. 1.21). Therefore, the flux balance in a dune is given by the difference between the net influx Q_{in} and the net outflux Q_{out}. Since both scale with the product $w\,Q$, the volume conservation reads

$$\dot{V} = Q_{in} - Q_{out} = w\,Q\left(\frac{q_{in}}{Q} - \frac{q_{out}}{Q}\right) \tag{1.74}$$

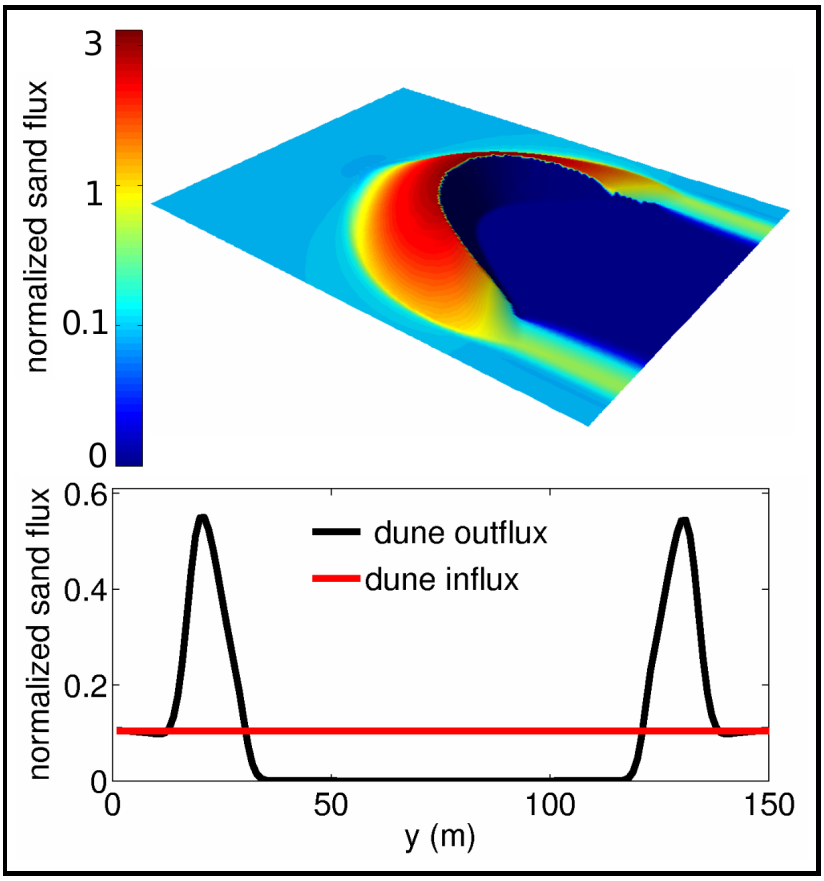

Figure 1.21: Top: color diagram of the normalized sand flux over a sand dune q/Q. The normalized influx is $q_{in}/Q = 0.1$. The sand flux increases at the windward side until it reaches its maximum at the brink ($q/Q \sim 4$). All this sand is trapped at the slip face where there is no flux $q/Q = 0$. Note that the flux scale is not linear. Bottom: dune outflux (red line) and influx (black line) as function of the transversal coordinate y. Although the barchan receives an homogeneous influx, its outflux is strongly localized at the horns.

where q_{in} and q_{out} are the dune influx and outflux per unit length, respectively, and V is the volume of the dune.

Measurements on single simulated barchans with a constant influx show that for small widths $w < w_c$ the outflux is saturated which means that the dune does not have slipface anymore, i.e. it becomes a dome. For higher width however, the outflux relax as $1/w^2$ to a constant value that scales linearly with the influx with a slope smaller that one (Fig. 1.22), namely

$$\frac{q_{out}}{Q} = a\frac{q_{in}}{Q} + b + \left(\frac{w_c}{w}\right)^2, \tag{1.75}$$

where $a \approx 0.45$, $b \approx 0.1$ and w_c are fit parameters. Therefore, there is two different regimes, for $q_{in} < 0.18\,Q$ the outflux is higher that the influx and the dune shrinks, while for $q_{in} > 0.18\,Q$ the influx overcomes the outflux and the dune grows (Fig. 1.22). The dimensionless barchan outflux q_{out}/Q is proportional to the total horns width fraction $2w_h/w$, where w_h denotes the width of one horn (Fig. 1.21). Thus, the flux balance on a

barchan dune is determined by its morphology.

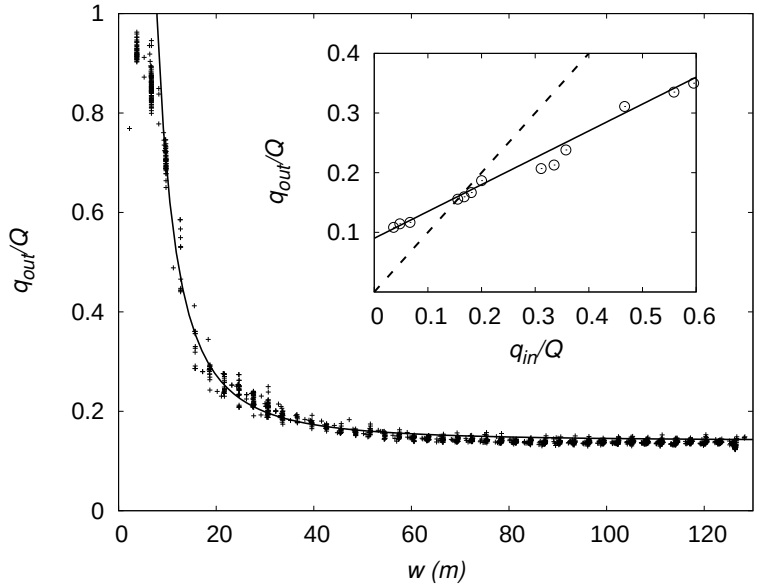

Figure 1.22: Relation between the dune outflux and the dune width w. The solid line represent the scaling with $1/w^2$ given in the text. Inset: the dune outflux is a linear function of the dune influx (solid line) with a slope smaller that one (dashed line).

The deviation from the scale invariance in the dune outflux q_{out} is expressed by the last term of Eq. (1.75), which is a consequence of the non-scale invariance for small dunes. However, since the critical width $w_c \sim 10$ m is of the order of the minimal dune width, the nonlinear term is very small and can be neglected. Therefore, we can consider in first approximation dune horns as scale invariant, in agreement with measurements on barchan dunes in south Morocco and in the Arequipa region, Peru (Elbelrhiti and Claudin, 2006).

In this case, the mass balance becomes

$$\dot{V} = w\,Q\,(1-a)\left(\frac{q_{in}}{Q} - \frac{q_c}{Q}\right) \tag{1.76}$$

where $q_c = b\,Q/(1-a) \approx 0.18\,Q$ denotes the equilibrium influx at which the dune volume does not change. However, this equilibrium is unstable since there is no mechanisms by which barchan dunes can change their outflux to adjust it to a given influx.

Volume

Simulations for different wind strength and influx show that the barchan volume V scales as w^3 independently of both, the sand flux over a flat bed Q and the influx q_{in} (Sauermann, 2001) following the equation

$$V = c\,w^3 \tag{1.77}$$

where $c \approx 0.017$ is obtained from the fit in (Fig. 1.23). This simple scaling was also recently found in field measurements (Hersen et al., 2004; Elbelrhiti and Claudin, 2006).

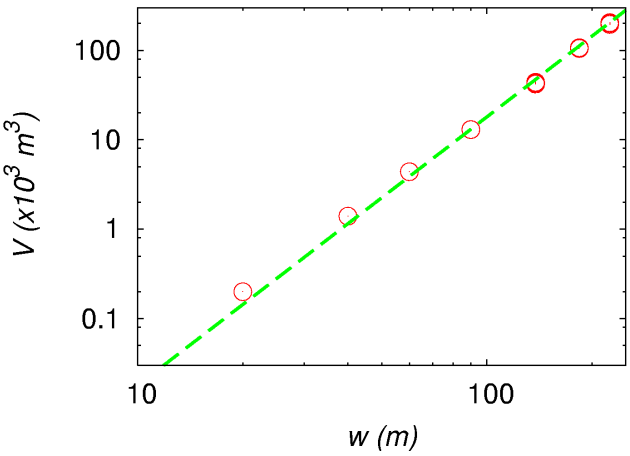

Figure 1.23: Cubic scaling of the volume of simulated barchan dunes with their width.

Time evolution of the dune size

Substituting Eq.(1.77), the mass balance becomes,

$$\dot{w} = \frac{Q\Delta}{3c\,w}, \tag{1.78}$$

where $\Delta \equiv (1-a)(q_{in}-q_c)/Q = (1-a)q_{in}/Q - b$. This equation gives the time evolution of the dune size. After integration,

$$w(t)^2 - w_0^2 = \frac{2\,Q\Delta}{3c}t, \tag{1.79}$$

where w_0 is the initial size at $t = 0$. The dune size evolves in such a way that the dune area $A \propto w^2$ increases linearly with time, and consequently the term Δ determines if it increases ($q_{in} > q_c$) or decreases ($q_{in} < q_c$).

The characteristic time t_s of the dune size change, defined as the period of time for the dune to triple its area ($w(t_s)^2 = 3w_0^2$), is given by

$$t_s \equiv \frac{3c}{|\Delta|}\frac{w_0^2}{Q}. \tag{1.80}$$

This time t_s scales with the dune's turnover time t_t defined in Eq. (1.73), namely

$$t_s \equiv \frac{C}{|\Delta|}\,t_t \tag{1.81}$$

where $C \equiv 3c\alpha \approx 2.5$. In the case of no influx the dune size significantly changes during a period of time of $\sim 20\,t_t$. To give an example, the 6 m high barchan ($w \sim 80$ m) shown in Fig. 1.18, under the Moroccan wind regime with $Q \approx 80\,m^2/yr$ (Elbelrhiti et al., 2005) and without sand influx $q_{in} = 0$, will disappear after a characteristic time $t_s/2$ of the order of 20 years. Although the zero influx is an extreme case, it is clear that within periods of time of the order of hundreds of years this instability should have a huge impact on the dynamics of barchan dune fields.

1.5 Conclusions

A new sand flux model was derived, giving a tentative explanation for the different scalings with u_*, found in previous works. The model leads to a simple linear equation for the sand flux that contains the main features of previous experimental and numerical findings. It also fits well the wind tunnel data of Rasmussen and Iversen (Iversen and Rasmussen, 1999; Rasmussen and Rautahemio, 1996). Using some scaling relations introduced by Andreotti (Andreotti, 2004), we calculated the dependence of the model parameters on the fluid properties such as density, gravity, viscosity and on the diameter of sand grains. It should be adressed that these dependences are crucial for the modeling of dunes in different physical conditions, like in the Mars atmosphere, inside water or simply to study the effect of the grain diameter on the dune morphology (Parteli et al., 2006).

Furthermore, we have presented the DUNE model including the new sand transport model. We also used the DUNE model to simulate barchan dunes and to obtain the scaling relations that characterize their morphology and dynamics. Finally, we studied the stability of barchan dunes showing that they are intrinsically unstables, a result that is in deep contradiction with the widespread existence of barchan dunes all around the world (Hersen et al., 2004; Elbelrhiti et al., 2005). This problem will be treated in details in the next chapter.

Chapter 2

Barchan dune fields

Barchan dunes don't appear isolated, instead, they belong to several kilometers long dune fields forming corridor structures oriented along the wind direction (Fig.2.1). Inside these corridors the dunes show a rather well selected sizes and inter-dune spacing. However, barchans are intrinsically unstable and thus they continously growth or shrink until disappear. This contradiction suggests that, at the statistical level, the behavior and evolution of single dunes result from their interaction with a large part of their entire surroundings, which are typically composed of several thousands dunes (Hersen et al., 2004; Elbelrhiti et al., 2005).

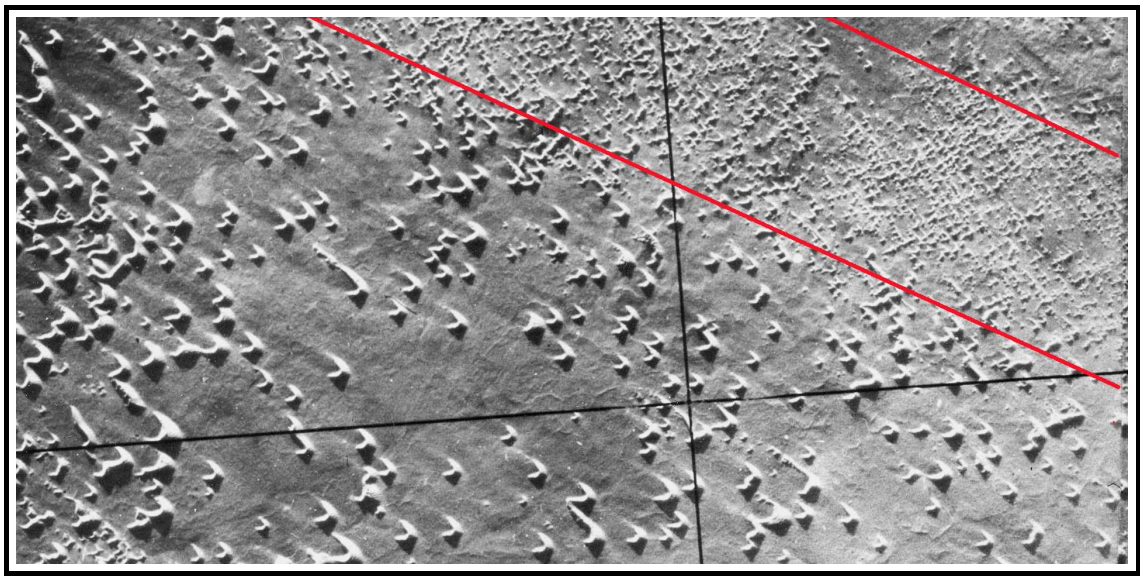

Figure 2.1: Example of a barchan dune field in Morocco, West Sahara. The dune field is divided into corridors along a the wind direction, where the dune size is roughly uniform.

In this chapter we present different approaches to model an entire dune field based on the laws extracted from the simulation with the much complex DUNE model in the previous chapter. The aim is to highlight the underlying process that leads to a size selection into a dune field. In Section 2.1 we present size distributions and inter-dune spacing distributions measured in different dune corridors in the Morocco desert by analysing satellite

images. We show that dune fields not only present a characteristic dune size but it is log-normal distributed. Simulation approach starts in Section 2.2 where we perform a simulation of a whole dune field using the DUNE model. Although they qualitatively reproduce a real dune field, the number of dunes is too small to be statistically relevant. In Section 2.3, simulations are carried out to understand what happens when two dunes collide with each other. The three different final situations of coalescence, solitary wave behavior and breeding (Duran et al., 2005) provide another mechanism to avoid continuous growth of the dunes in a dune field. From dune collisions with lateral shift we extract a general rule and make a fit of the resulting volumes and positions. These new rules and a simplified representation of the sand influx and outflux of a dune, extracted from DUNE analysing of single barchans, form the basis to model a large dune field presented in Section 2.4. In Section 2.5 these laws are used to construct an analytical 'mean-field' approach which provides a size distribution similar to the measured lognormal one. Finally, in Section 2.6 we resume our findings with some scaling relations between the spatial distribution, the size distribution and the boundary conditions.

2.1 Barchan dune field measurements

The Morocco desert in Western Sahara presents the longest barchan dune field on the Earth. There, barchan dunes develop under a strong uni-directional wind in tens of kilometers long corridors with a characteristic dune size and a homogeneous dune distribution (Fig. 2.1). In order to get insight into the statistical properties of the field we measure the dune size and the inter-dune spacing.

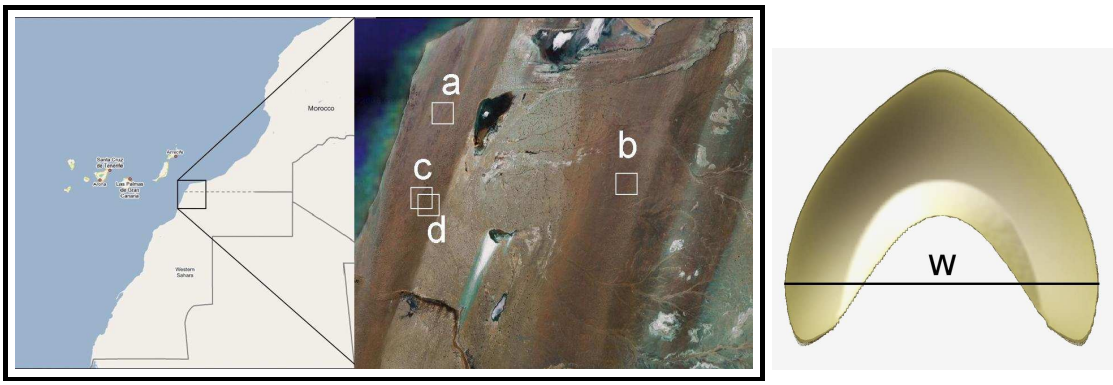

Figure 2.2: The four measured dune field corridors (a), (b), (c) and (d) localized in western Sahara. Right: sketch of a barchan dune showing the 'width line', a line between the two points that define its width.

From chapter 1 we know that width w represents the best characterization of barchan dunes since it fully describes the area, volume and velocity of the barchan. Therefore, we perform digital measurements of the width of more than five thousand dunes in four corridors between Tarfaya and Laayoune using one meter per pixel resolution satellite images (Fig. 2.2). Figures 2.3 and 2.4 show the four measured dune fields downwind oriented, where each barchan is represented by its 'width line' defined in Fig. 2.2. The

dune width w against its downwind distance x, also depicted in the figures, show no clear trend in the spatial distribution at this scale.

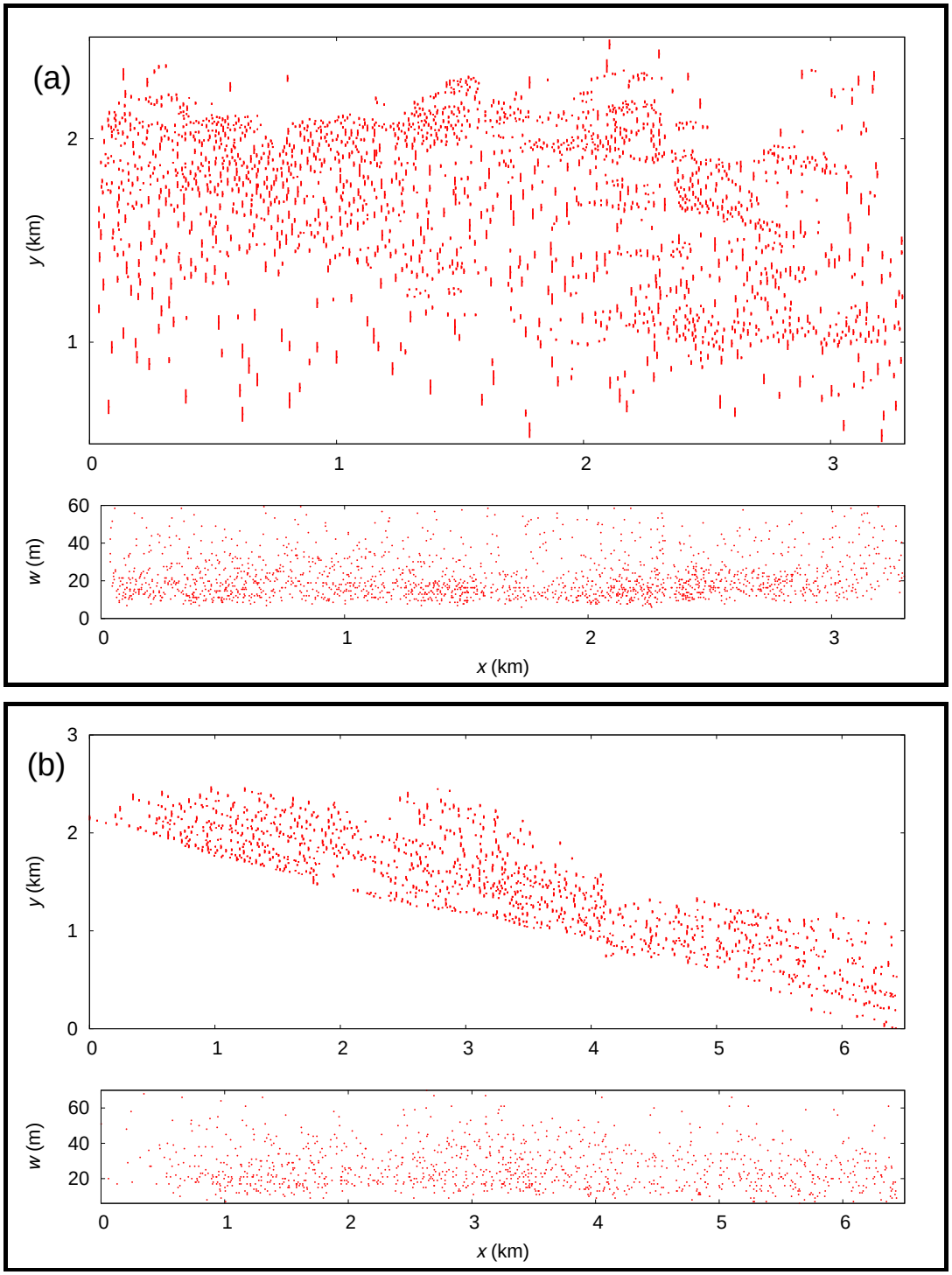

Figure 2.3: Top: measured barchan dunes in corridors (a) and (b) depicted in Fig. 2.2. Dunes are represented by their 'width line'. The x axis is oriented along the wind direction which is also the direction of dune movement. The bottom window in both figures shows the width against the x-position of the dune.

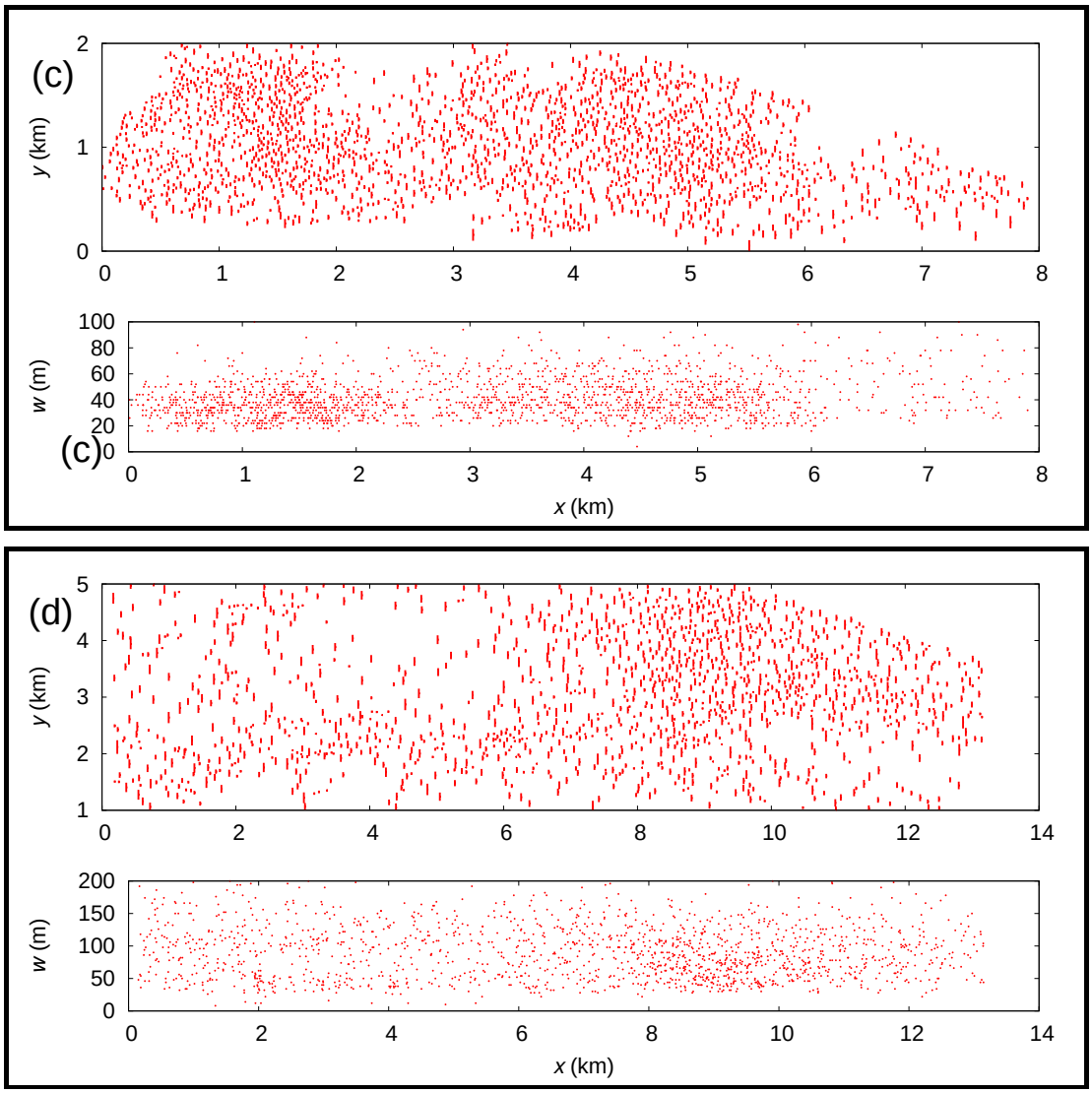

Figure 2.4: Top: measured barchan dunes in corridors (c) and (d) depicted in Fig. 2.2. Bottom: dune width against its downwind distance x.

2.1.1 Dune size distribution

We start by studying the distribution of dune sizes in the real dune fields. Figure 2.5 shows the dune size distribution for the four dune fields shown in Fig. 2.2. In all cases the measured distributions (symbols) are well fitted by lognormal distributions (solid lines) defined as

$$P(w) = \frac{1}{\sqrt{2\pi}\sigma\, w} \exp\left(-\frac{(\ln w - \mu)^2}{2\sigma^2}\right), \tag{2.1}$$

from which the mean width $\langle w \rangle = \exp(\mu + \sigma^2/2)$ and the standard deviation $S^2 = \langle w \rangle^2 (\exp \sigma^2 - 1)$ are determined.

Although the size distribution can be fully described by the two parameters of the lognormal fit, their physical origin is unknown. Furthermore, the lognormality in the size distribution implies an underlying multiplicative process in the evolution of the dune sizes.

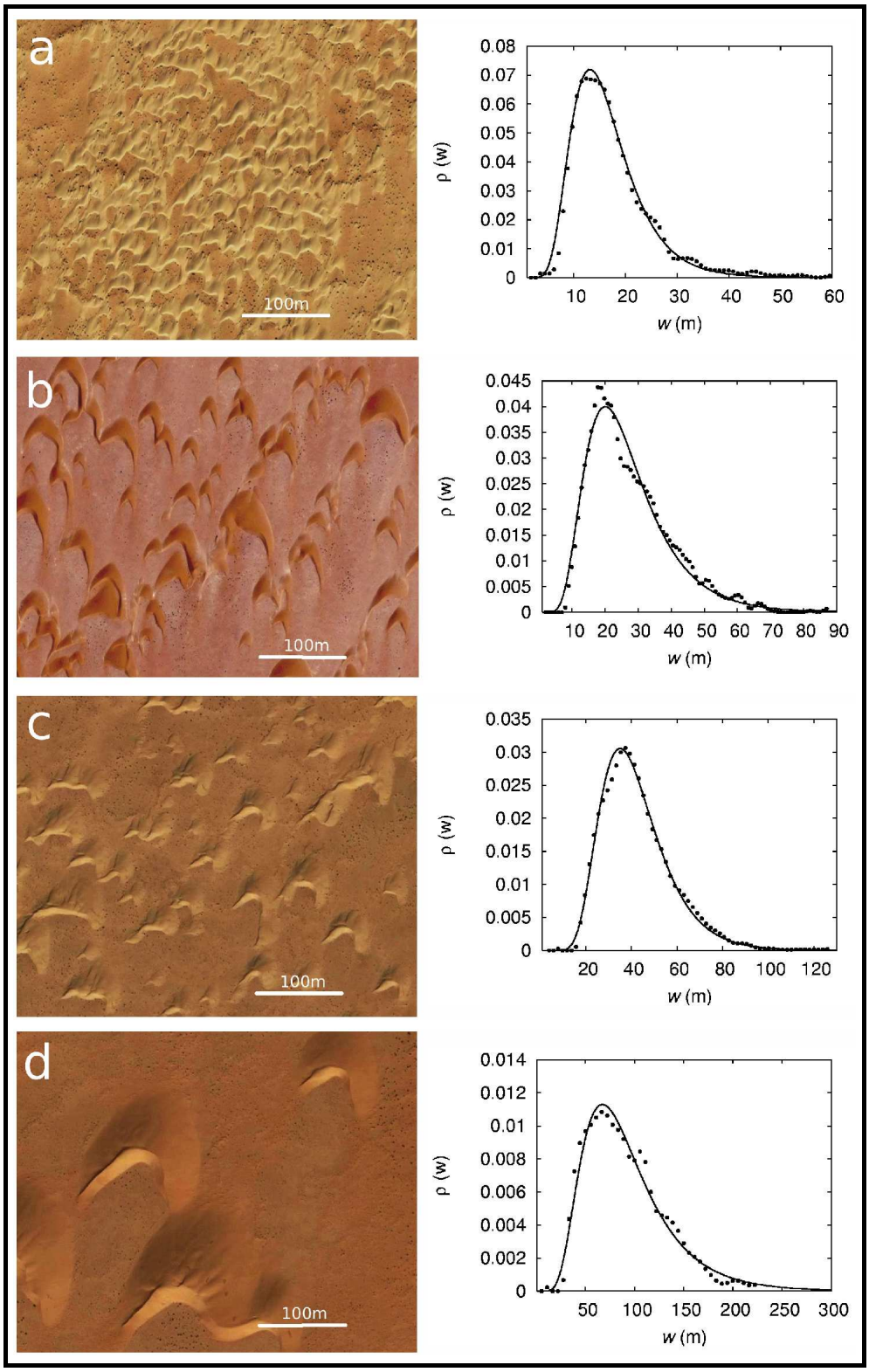

Figure 2.5: Snap shots of four dune field corridors (a), (b), (c) and (d) localized in western Sahara along with their dune width distribution (dots) and the lognormal fit (full line).

This process and the factors that determine the characteristic dune size and the standard deviation of its distribution, will be the central questions for the rest of this chapter.

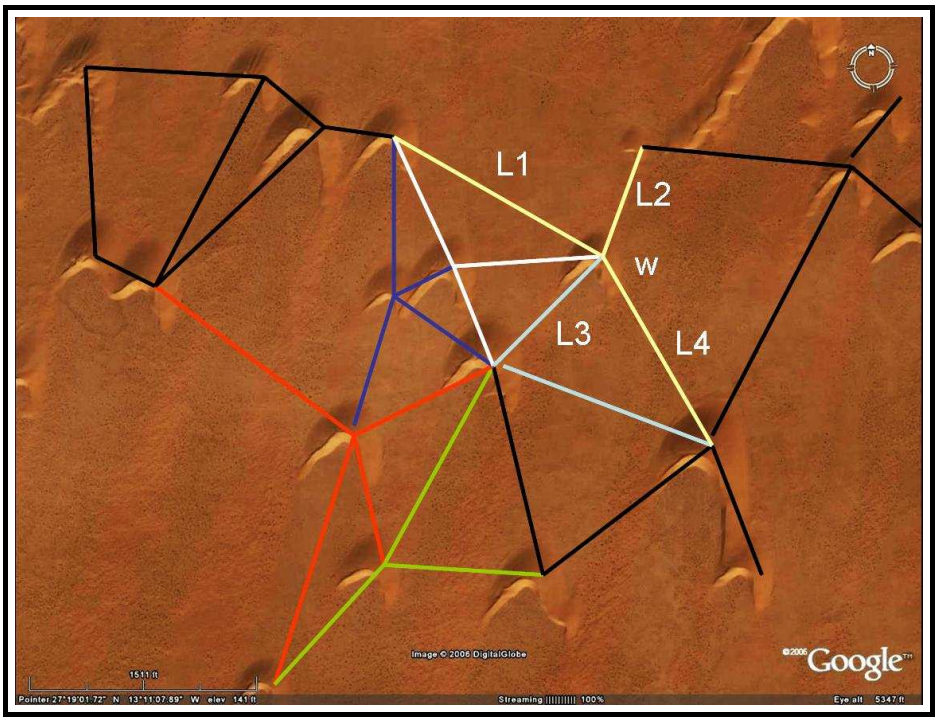

Figure 2.6: Dune field planar network. The neighborhood of a dune of width w is defined by its nearest neighbors in each of the four diagonal directions placed at a distance L_1, L_2, L_3 and L_4 respectively.

2.1.2 Inter-dune spacing

Besides the size distribution, the spatial distribution of dunes is another important property of dune fields. It gives information about the sand distribution along the field and thus, about the total amount of sand transported by it.

We characterize the spatial distribution of dunes by the inter-dune spacing $L(w)$, defined as the characteristic distance between a dune of width w and its neighbors. The spacing $L(w)$ is given by

$$L(w) \equiv \sqrt{A_f(w)} \tag{2.2}$$

where $A_f(w)$ is the sand free area surrounding the dune w. The free area $A_f(w)$ in turn is given by the area $A_p(w)$ of the polygon formed by the neighbors of a given dune after substracting the fraction of their own area inside it. In order to define the neighborhood around a dune and calculate the area A_p, we construct a planar dune network as sketched in Fig. 2.6. In the simplest approach, after selecting a dune w we look for its nearest neighbor in each of the four quadrants defined by the cartesian coordinates system centered at the dune, i.e. $(+x, +y)$, $(-x, +y)$, $(+x, -y)$ and $(-x, -y)$. These four dunes are then linked to the central one w in an iterative process that leads to a planar network of connectivity four. Within this approach, the first neighborhood area $A_p(w)$ of a dune of width w is determined by the first four neighbors and their respective distances L_1, L_2, L_3 and L_4 (Fig. 2.6).

Figure 2.7 shows a histogram of the spacing length $L(w)$ around a dune of width w for

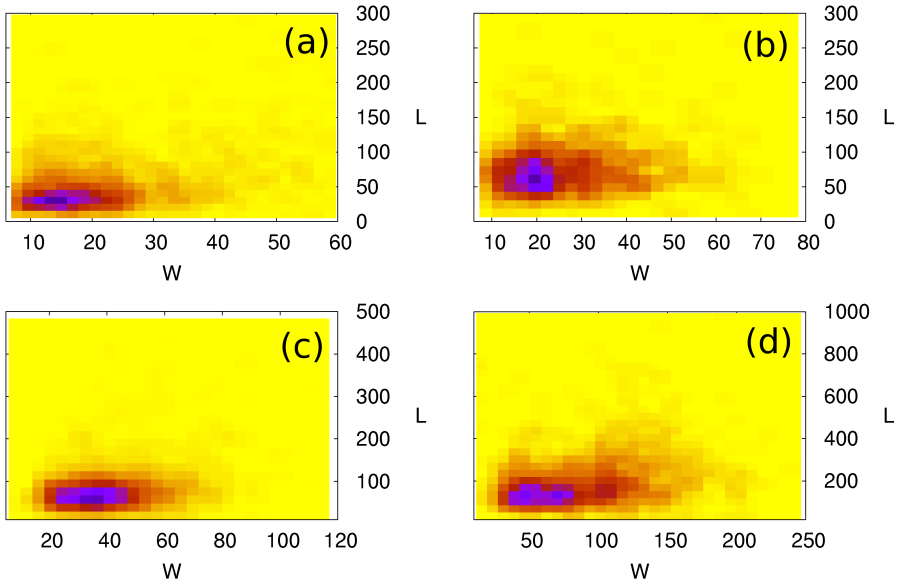

Figure 2.7: Scaling of the inter-dune spacing. Plot of the inter-dune spacing L as a function of the dune width w for each measured dune field. Blue indicates the pairs (w, L) occurring with highest frequencies, where a well-defined $\bar{L}$ can be ascribed independently of w.

each of the four measured fields (Fig 2.5). In agreement with previous statements (Hersen et al., 2004), we found that the spacing between dunes takes well-selected values within the same field. Indeed, the inter-dune spacing L, although scattered, shows no clear trend as a function of dune size and its mean value $\bar{L}$ is nearly constant for the whole size range depending only on the selected dune field.

The independence between dune size and dune spacing is not only a consequence of the uniformity of the spatial distribution of dunes but also a special feature of barchan dune fields deeply rooted in the dynamics behind the dune size selection and their spatial distribution. For instance, in static dune fields (e.g. longitudinal or star dune fields) larger dunes are surrounded by larger empty space. Thus, the inter-dune spacing scales with the dune size. This linear scaling is a consequence of the way sand is redistributed among the dunes. In static dune fields, since the annual average of the relative motion between dunes is almost zero, they change their size only by the balance between the influx and the outflux. Therefore, based on mass conservation, a dune accumulates sand and grows only if its neighboring dunes loose sand and shrink. On the other hand, in barchan dune fields dunes are mobile and they can collide with each other. As we will see, in such a scenario small dunes are continuously emerging from larger ones due to collisions, destroying any simple correlation between dune size and inter-dune distance and leading to a spatial uniformity.

2.2 DUNE simulation of a dune field

In this section we start looking for the answers to the following problem. Since an isolated barchan dune is unstable, which mechanism accounts for its stabilization at dune field scale? Is it the same mechanism behind the lognormal size distribution? Which factors determine the mean size and standard deviation of such a distribution? Is there any relation between the dune size distribution and the inter-dune spacing in a given dune field?

Our search starts with numerical simulations of an entire dune field using the DUNE program introduced in the Chapter 1.

Birth of barchan dune fields: Open boundary conditions

It is already known that most of the barchan dune fields arise from the accumulated sand in the sea shores. Therefore, we select the open boundary and initial conditions to mimic a beach. Since the sea provides a net sand income, we set the field influx to the maximum value Q, which is the saturated flux in a flat bed. Furthermore, taking into account the characteristic sand hill limiting sandy coats, we introduce as initial surface a very small sand gaussian hill upwind the field that acts as a terrain perturbation.

Figure 2.8 shows a barchan dune field emerging from a beach. At the beginning only appears the small sand perturbation upwind (Fig. 2.8a). Later, as the incoming sand accumulates in the lee side, the initial 50 m long hill expands until 200 m, when it becomes unstable and small sand bumps are ejected (Fig. 2.8b). This transversal instability, transversal because it occurs along the wind direction, is the key mechanism underlying the emergence of sand dunes. It was originally obtained for a flat sand surface using a simplified version of the DUNE model equations (Andreotti et al., 2002a). The same explanation accounts for the instability in our case, since the maximum slope of the hill is $\sim 0.6^o$ and it can be considered as a flat plane.

Further in the evolution, the hill becomes broader and ejects sand strips instead of bumps (Fig. 2.8c). These transversal sand strips are in turn unstable along the longitudinal direction, perpendicular to the wind direction, and they split into barchan dunes (Fig. 2.8c and d). This longitudinal instability is key to the emergence of barchan dunes from transversal ones. It was first obtained in our simulations and an analytical study is under progress.

Both instabilities, the transversal and longitudinal one, account for the emergence of a barchan dune field from a near flat bed in conditions of uni-directional wind and scarce sand supply as shown in Fig. 2.9 under real conditions.

The simulations using open boundary conditions, although explain the birth of barchan dune fields, are not adequate (due to the scale) to study their statistical properties. Therefore, we focus on dune field simulations using periodic boundary conditions, by which the dune field reaches a stationary state with a well defined dune size distribution.

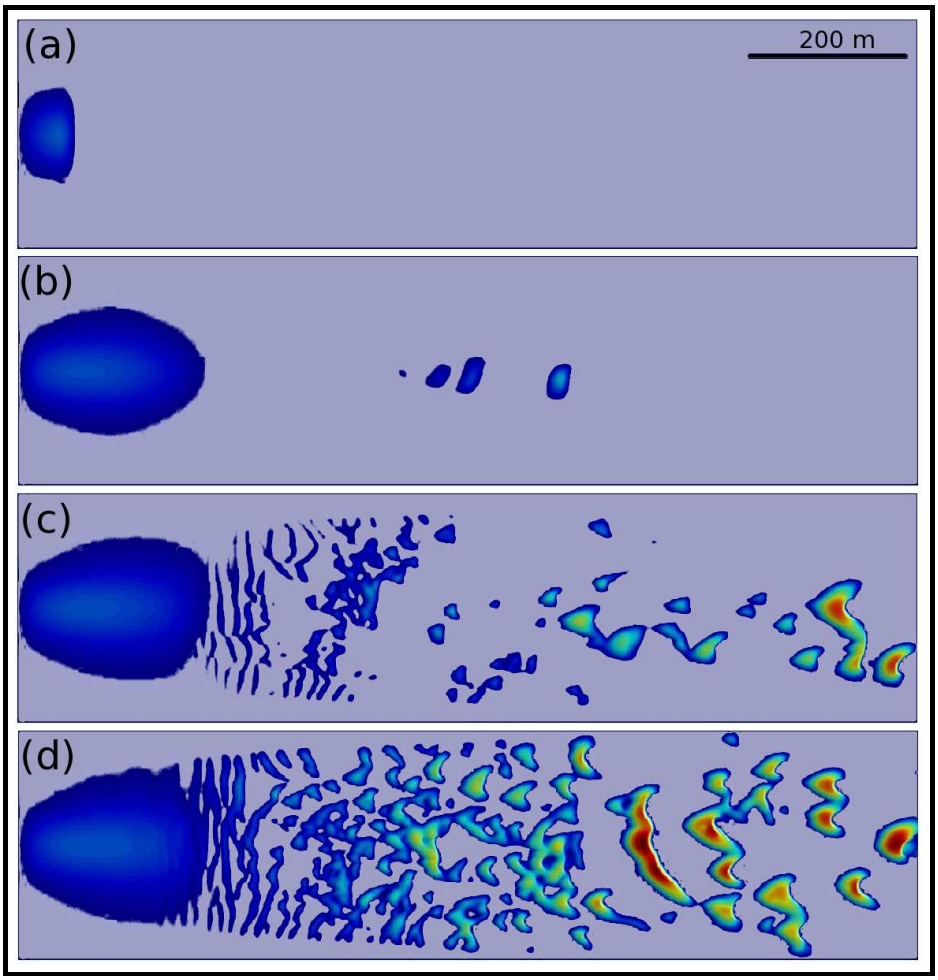

Figure 2.8: Snap shots of the birth and evolution of a barchan dune field from a beach. Wind blows from left to right. The small sand perturbation upwind the field (a), is unstable and ejects first some small bumps (b) and later transversal sand strips that become barchan dunes, (c) and (d). Gray represents the rocky ground while colors represent the sand height, blue $\sim$ 1 m high, and red $\sim$ 3 m high.

Figure 2.9: Real example of a rising dune field in Egypt. Wind blows from left to right. Both instabilities occur, first the transversal one that breaks the plane surface in transversal strips, and later the longitudinal one that breaks the transversal symmetry of the strips in bumps that evolve to barchan dunes.

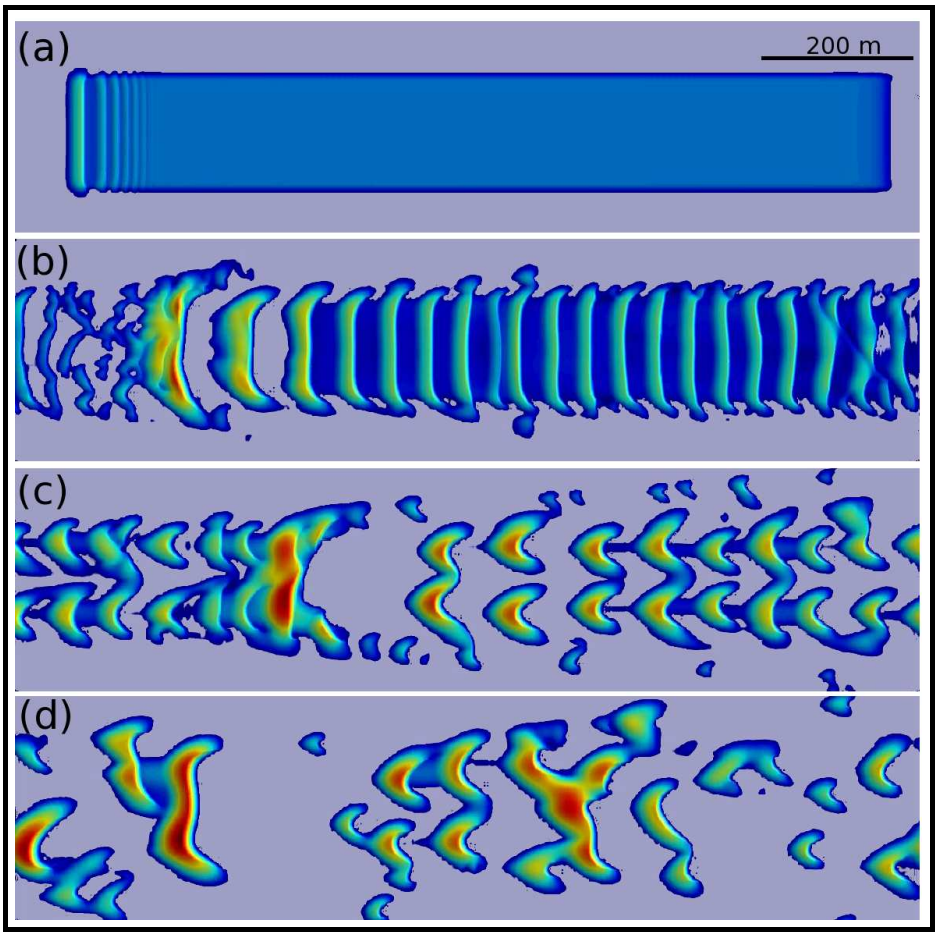

Figure 2.10: Snap shots of the dune field evolution from a uniform sand bed under periodic boundary conditions. Wind blows from left to right.

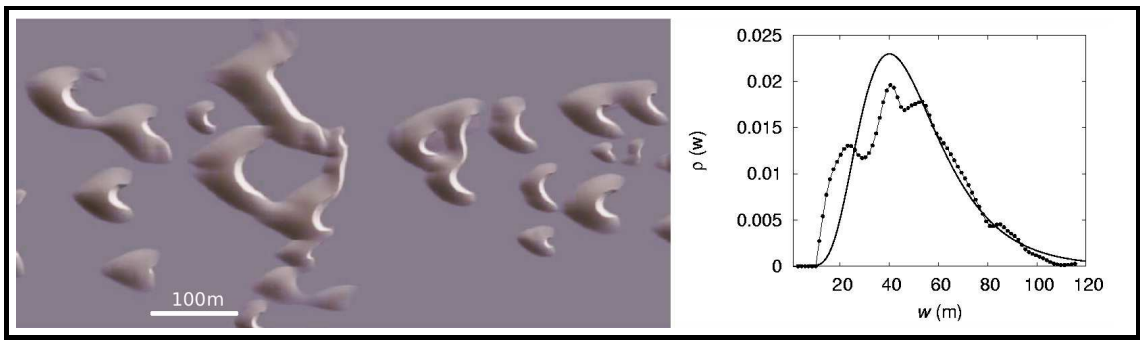

Figure 2.11: Snap shot of a simulated barchan dune field along with its dune width distribution function (dots) and the lognormal fit (line).

Birth of barchan dune fields: Periodic boundary conditions

We perform periodic boundary condition simulations starting with an uniform sand bed over a non-erodible surface in the center of the field, as illustrated in Fig. 2.10a.

After wind starts to blow, transversal instabilities appear over the sand bed propagating

downwind until the whole bed is fragmented into transversal dunes (Fig. 2.10b). Once the sand between the dunes is completely eroded and the rocky substrate exposed, transversal dunes become unstable and split into two rows of barchan dunes that after leaving the field re-emerge at the beginning due to the periodic boundaries (Fig. 2.10c). This feedback leads to collisions between barchan dunes which besides the flux exchange between them acts as a size selection mechanism that leads to an apparent equilibrium size distribution (Fig. 2.10d).

Figure 2.11 shows a snap shot of the simulated dune field and the dune width distribution averaged over different time realizations along with a lognormal fit. The simulated field is quite realistic and qualitatively reproduce the main features of a real one (see for example Fig. 2.2) like the clusters of colliding dunes and the alternate localizations of consecutive barchans. Furthermore, the size distribution has the correct trend for high sizes although it fails at small and middle sizes. There is an over representation of small sizes in the field due to the small simulated field scale with only ~ 30 dunes at each time realization, instead of ~ 1500 dunes in the real ones. Although this hypothesis can be tested using a larger field, it requires prohivitive CPU time in order to get a statistic as good as the measured one.

2.3 Binary collisions

To understand physically the dune size distribution one must take into account the dynamical processes that govern the growth of single dunes. The intrinsic instability of barchan dunes under an incoming sand flux leads to an increase of the largest dunes in the field whereas the smaller ones shrink until disappear [(Hersen et al., 2004; Hersen and Douady, 2005)]. Hence, the mean size of the dunes grows with the distance from the beginning of a field. Nevertheless, in many dune fields the sizes saturate. Two mechanisms have been proposed to avoid unlimited dune growth: instability of large dunes due to changing wind directions (Elbelrhiti et al., 2005) and collisions between dunes (Schwämmle and Herrmann, 2003; Duran et al., 2005; Hersen and Douady, 2005).

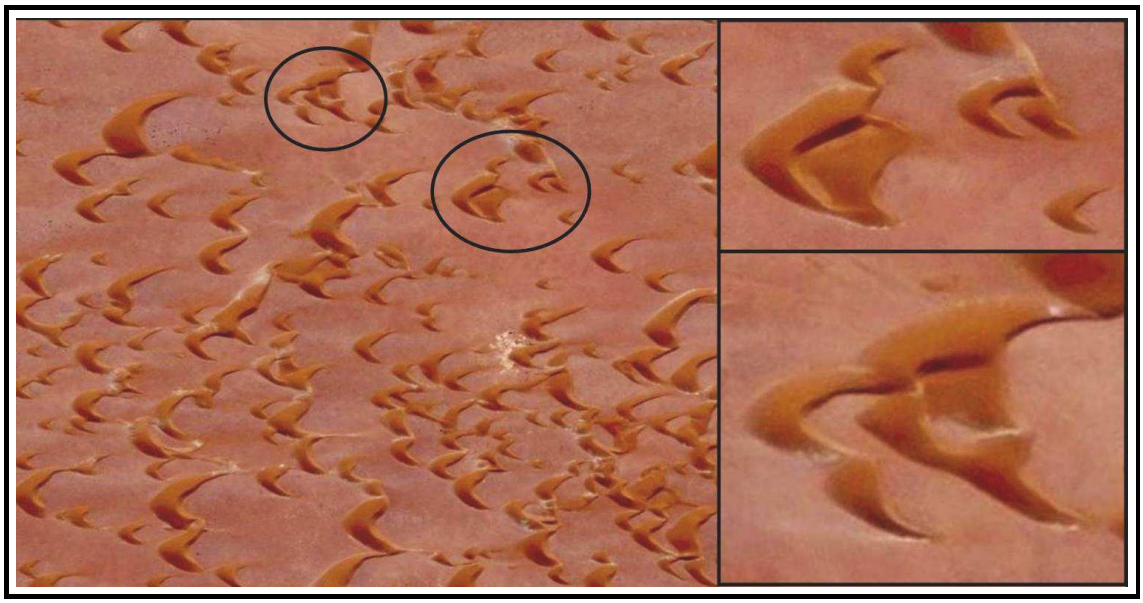

Figure 2.12: Collisions between barchan dunes are ubiquitous in a dune field. Here are some examples of collisions in a Maroccan dune field.

The spontaneous fragmentation of a dune when wind velocity fluctuates in strength and direction involves a higher degree of complexity in numerical simulations. Therefore, in this section we concentrate only on the dynamics of collisions between two dunes.

Collisions are ubiquitous in dune fields (see Fig. 2.12) due to the relatively broad range of different velocities which obey in general $v \sim 1/w$ for single dunes (Hersen, 2005). Due to the dependence of their velocity on their size, the dune that collides onto a second one must be smaller than the latter. This process has been observed several times (Besler, 1997; Besler, 2002) but was not understood until the last years. The large temporal scales of such a process makes it difficult to observe the final state after such a collision. Simulations using DUNE model are carried out to understand what happens if two dunes collide with each other and different results are obtained depending on the relative volume difference between the interacting dunes (Duran et al., 2005). The three different final situations of coalescence, solitary wave behavior and breeding provide mechanisms to redistribute the dune sizes and thus to avoid continuous growth of the dunes in a dune field.

Through the simulations of dune collisions with lateral shift we extract a general rule and make a fit of the resulting volumes. These new rules are implemented into a model for the evolution of a simplified dune field where dunes only collide with each other. From this model we found that collisions as a mechanism of redistribution of sand is capable of selecting a characteristic dune size. In fact, dune sizes in such a scenario follow a Gaussian distribution.

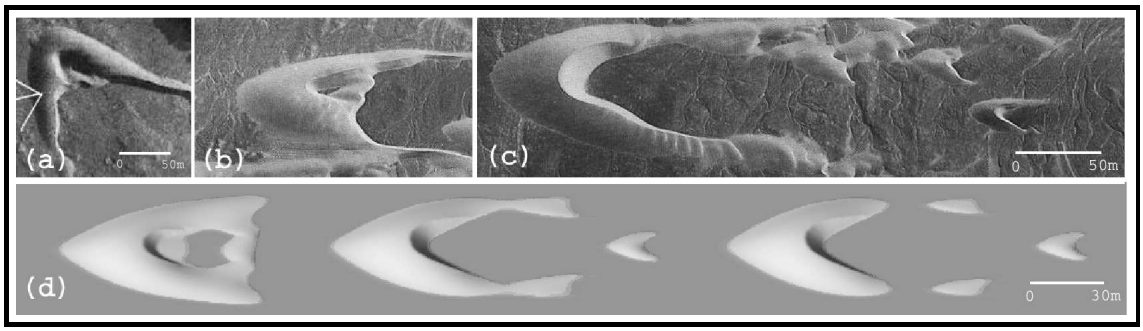

Figure 2.13: Examples of the breeding process in two barchan fields, Namibia (a) and Peru (b), (c), and in numerical simulations (d).

2.3.1 Collision dynamics

Up to now modeling mainly focused on single dunes or dune patterns without regarding the mechanisms of dune interactions. Recently, Besler found small barchans at the downwind side of big ones and concluded that barchan dunes could behave like solitons (Besler, 1997; Besler, 2002). This means that they would behave like solutions of non-linear equations, for example those describing waves in shallow water, which propagate through each other without changing their shape (Lamb, 1980). As an example see Fig. 2.13. In (a) and (b) a small barchan is apparently ejected from the main dune, whereas, in (c) small dunes emerge from the horns. Note the similarity with the snapshots of a collision simulation depicted in (Fig. 2.13b). Similar occurrences can be found in experiments with sub-aqueous barchans (Endo and Taniguchi, 2004). Nevertheless, most researchers believe that if a small barchan hits a bigger one, it will be completely absorbed. This is motivated by the fact that a sand formation cannot cross the slip face of a dune without being destroyed. Therefore, the description of barchan dunes as solitons has found very little support up to now, until Schwämmle et al. found that dunes can behave as solitary waves under certain conditions (Schwämmle and Herrmann, 2003). They show that, due to mass exchange, a big barchan colliding with a smaller one placed behind, may decrease its height until it becomes smaller, and therefore, faster, than the previous one, and leaves. Meanwhile the initially smaller dune increases its height, becoming bigger and slower, in such a way that it looks as if the smaller dune crosses the big one. This situation was referred by analogy as solitary wave behavior despite the big differences with real water waves (Livingstone et al., 2005; Schwämmle and Herrmann, 2005b). Katsuki et al. (Katsuki et al., 2005) have also obtained solitary wave behavior for coaxial and offset collisions of two sub-aqueous barchans.

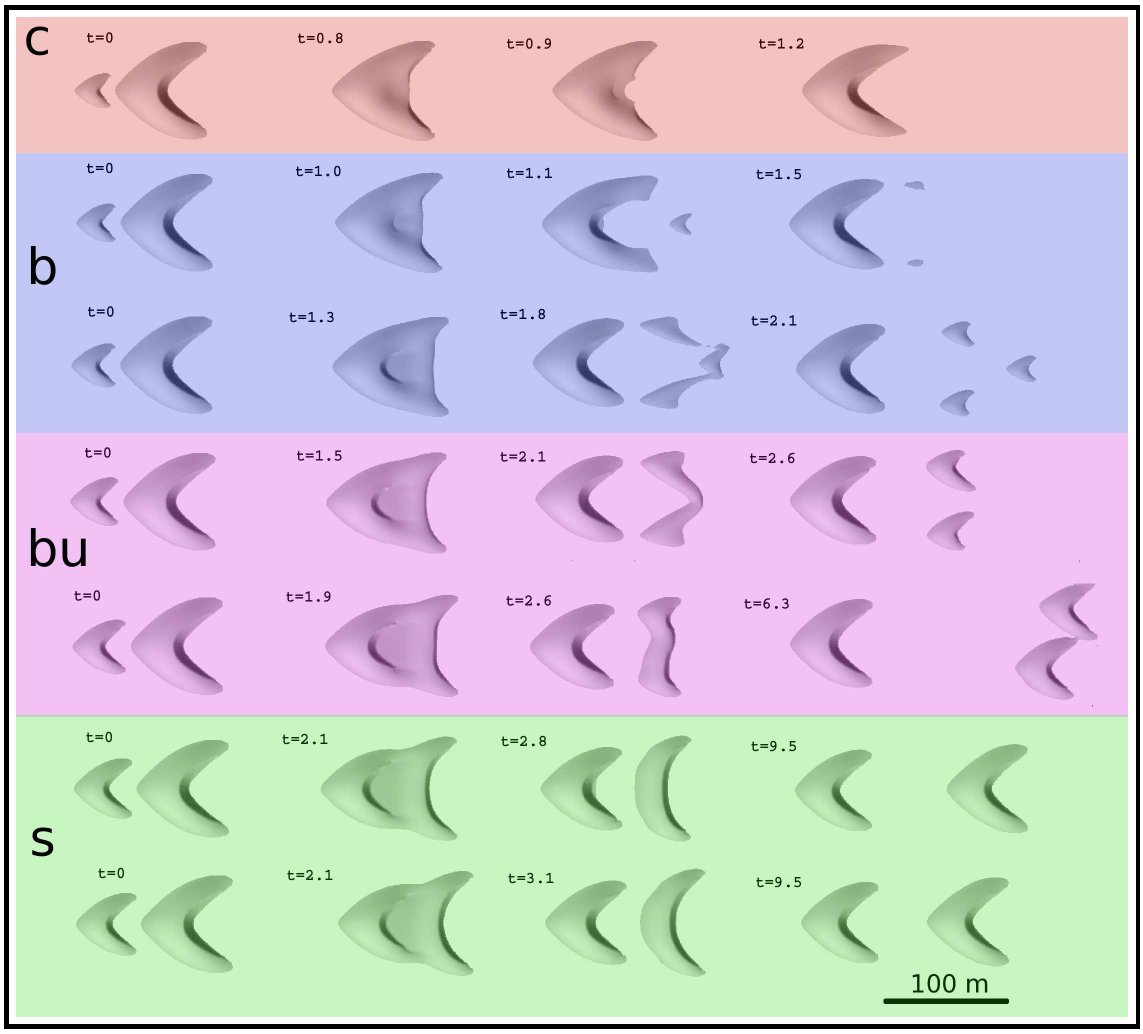

Figure 2.14: Snap shots of the time evolution (from left to right) of different situations during the collision of two barchans for zero lateral offset and volume ratios: $r_i = 0.06$, 0.08, 0.12, 0.17 and 0.3. The volume ratio increases from top to bottom. Depending on the volume ratio, coalescence (c), breeding (b), budding (bu) and solitary wave behavior (s) take place. Wind blows from left to right. The time (t) is in years, taking into account that wind blows continuously during all the year.

Simulations of the DUNE model are carried out to obtain the outcome of collisions between two dunes for different initial lateral offsets θ_i and volume ratios r_i keeping the volume of the larger barchan constant at 6000 m^3. We define the relative lateral offset between two dunes as $\theta \equiv \frac{Y-y}{W/2}$, where Y and y are the coordinates of the geographic center of the large and the small dune in the lateral direction transverse to their movement, respectively. Besides, the volume ratio is defined as $r \equiv \frac{v}{V}$, where V is the volume of the large barchan and v the one of the small one. The strength of the wind blowing into the system is fixed to a shear velocity of 0.5 m/s. Open boundary conditions are used with an influx of 20 m^2/yr, equal to the big barchan equilibrium outflux.

In order to take into account the lack of scale invariance of barchans, we repeat the simulations for a different size of the big barchan, with initial volume $V = 70\,000$ m^3. The same

general picture was observed. Figures 2.14, 2.15, 2.16 2.17 illustrate different temporal stages of the collision process for different volume ratios and increasing offsets, starting from zero.

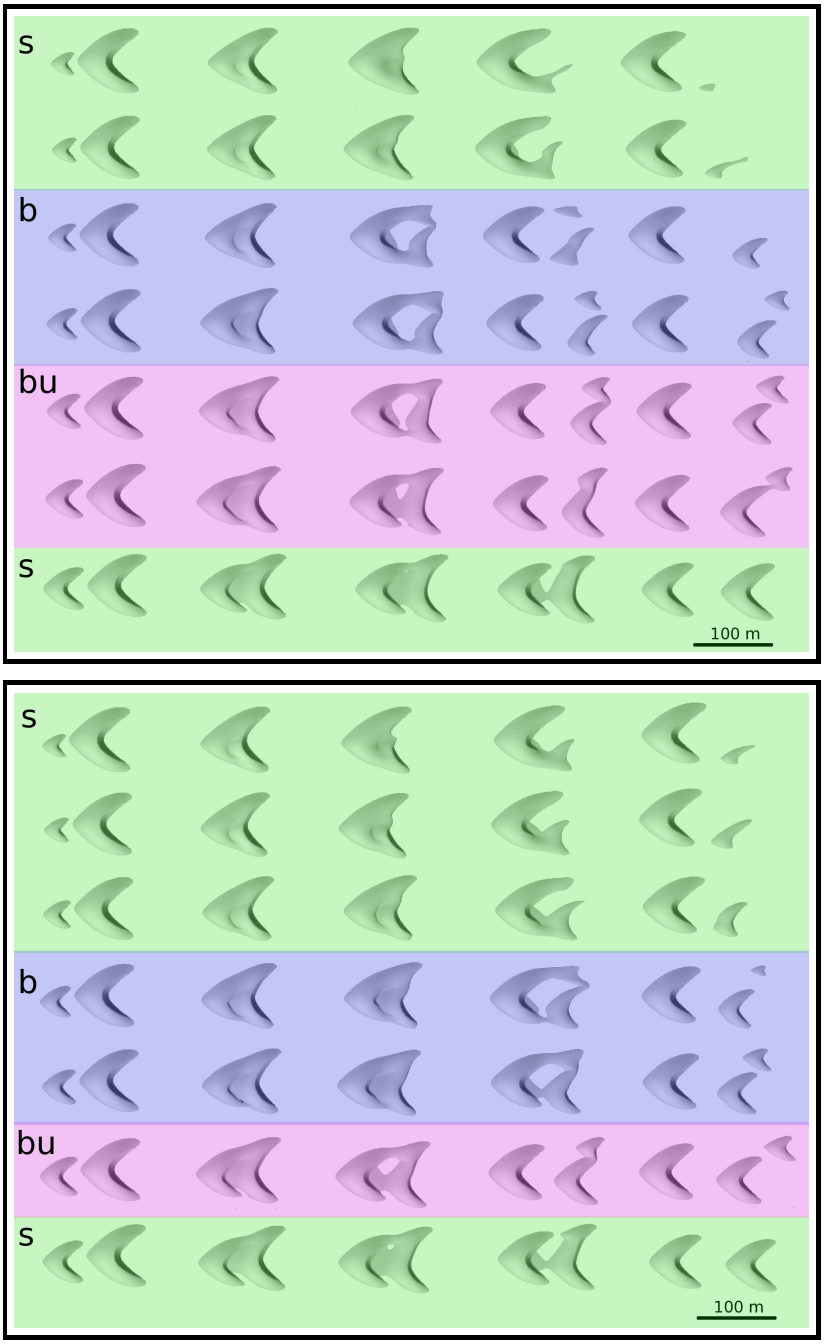

Figure 2.15: Snap shots of the time evolution of different situations during the collision of two barchans. In top window collisions with $\theta_i = 0.1$ are depicted, while the bottom window represents collisions with $\theta_i = 0.2$. The volume ratio in both figures increases from top to bottom and are the same as depicted in Fig. 2.14. Letters and colors distinguish the different results after collision.

The smaller barchan at some point bumps onto the larger one. This leads to a hybrid state where the two dunes melt into a complex pattern. Depending only on the initial relative

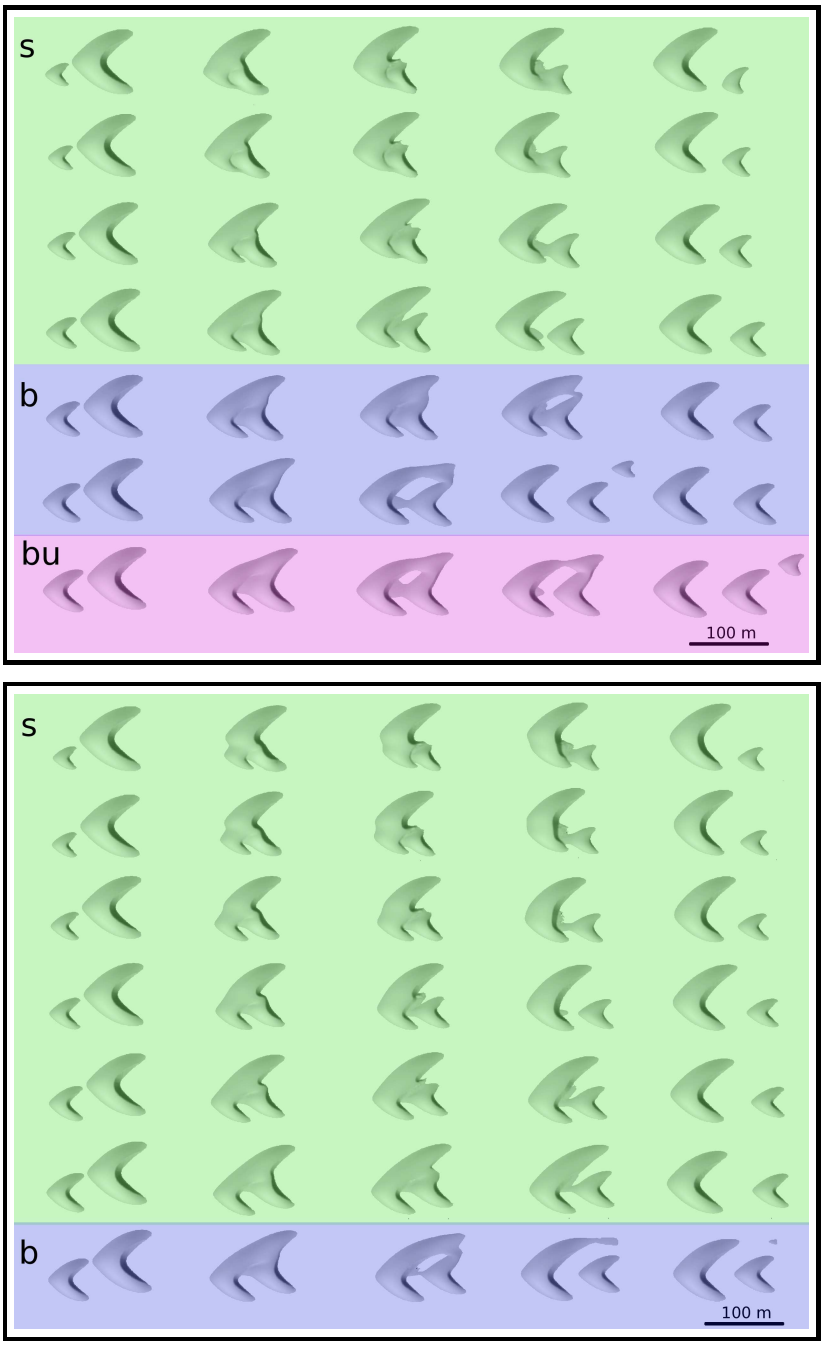

Figure 2.16: Snap shots of the time evolution of different situations during the collision of two barchans. Top window shows collisions with $\theta_i = 0.4$ while bottom window shows collisions with $\theta_i = 0.6$ where only breeding (b) and solitary wave behavior (s) appear.

sizes r_i and lateral offset θ_i of the two dunes, four different situations can emerge after collision: coalescence (Fig. 2.14 c) where only one dune reamins, breeding (Fig. 2.14 b) and budding (Fig. 2.14 bu) where two dunes leave the larger one, and solitary wave behavior (Fig. 2.14 s) where the number of dunes remains two after the collision.

The evolution of the hybrid state can be understood as the result of a competition between two processes. The first one is the overlapping of both dunes at the beginning of the

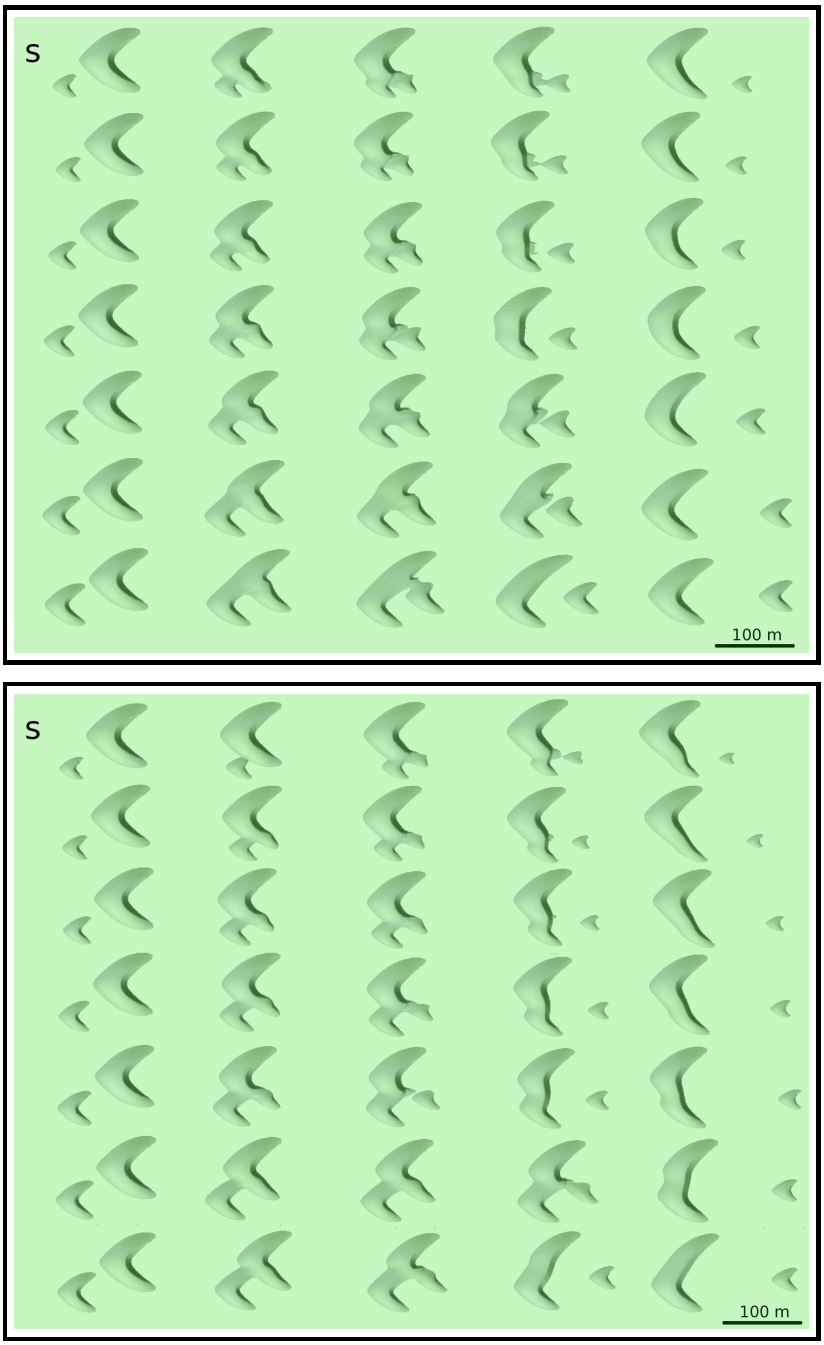

Figure 2.17: Snap shots of the time evolution of different situations during the collision of two barchans. Collisions with offset $\theta_i = 0.8$ and $\theta_i = 1.0$ are shown at top and bottom respectively. In both cases only solitary wave behavior (s) occurs.

collision that can eventually lead to coalescence (Fig. 2.18, upper part). The second one is the effective mass exchange between the dunes due to the changes induced in the wind shear stress due to the approaching of both dunes. In the hybrid state the wind shear stress over the windward side of the bigger dune is reduced and thus, crest erosion is enhanced. Besides, the wind shear stress over the lee side of the smaller dune is also reduced but enhancing crest deposition. Thus, the smaller dune may gain enough sand to become bigger than the one in front and therefore also becomes slower. In this way, the previous

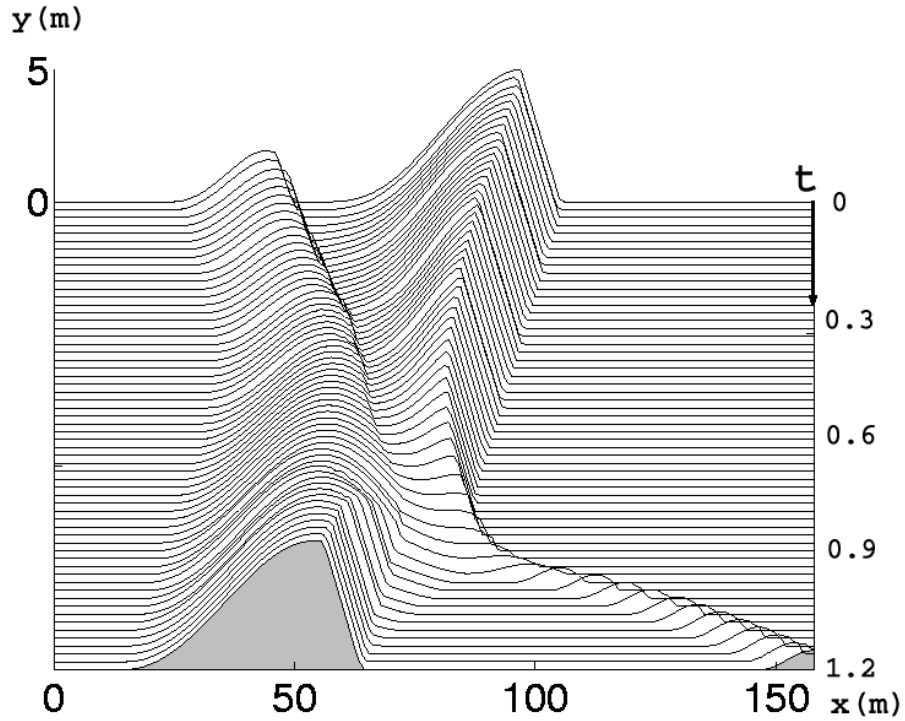

Figure 2.18: Time evolution of the central slice of the 'breeding' collision represented in the figure 2.14b, top. Initially the small dune climbing on the bigger one, and finally their mass exchange leading to their separation. The time (t) is in month.

bigger dune can actually become the smaller one and its velocity sufficiently large to leave the hybrid state. In this case the dunes separate again (Fig. 2.18, bottom).

The collision process is crucially affected by the separation bubble, i.e. the region after the brink and between the horns at which flow separation occurs. After the separation at the brink, the flow streamlines reattach smoothly near the line segment whose end points are the horns. There, sand transport continues again. However, inside the separation bubble the flow is strongly reduced and, for simplicity, we set the flux to zero. Hence, the upwind dune will absorb that part of the downwind dune inside its separation bubble (Fig. 2.14b, 2.14bu and 2.14s).

The morphological phase diagram of binary collisions is schematically showed in Figure 2.19 in terms of the final volume ratio as a function of the initial volume ratio and lateral offset. In order to include breeding and budding cases where more than one dune leaves the hybrid state the final volume ratio is defined as ratio between the volume of the total outgoing dunes and that of the remaining one.

For small relative volume and lateral offset both dunes coalesce to a single one. In this case the relative velocity is high and hence the overlapping is faster than their mass exchange. Small dunes have a short slip face which disappears while climbing up the bigger one. This reduces the mass exchange and leads to a complete absorption of very small barchans (red zone in Fig. 2.19 and Fig. 2.14c).

For a larger r_i and θ_i the slip face survives for longer time, mass exchange becomes

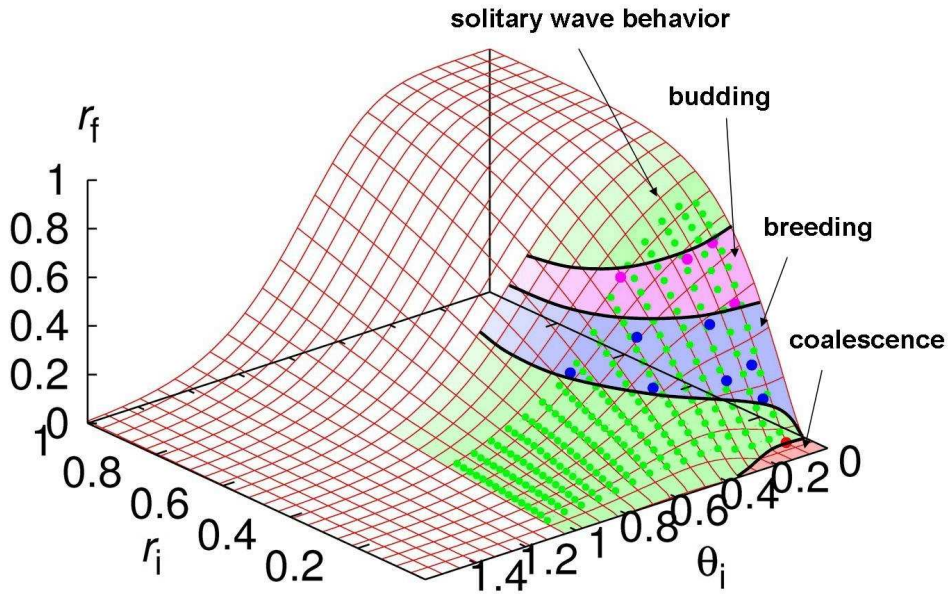

Figure 2.19: Sketch of the morphological phase diagram for binary collisions. The volume ratio r_f after the collision is plotted as a function of the initial offset θ_i and the initial volume ratio r_i. Dots represent simulation results.

relevant, and a small barchan is ejected from the central part of the dune between horns in what we call solitary wave behavior (lower green zone in Fig. 2.19 and upper green zone (s) in Figs. 2.15, 2.16 and 2.17). For a given range of the lateral offset, the perturbation of the big dune shape, due to the overlapping of the small dune behind, also propagates over the horns since there is no slip face. At the end of one or both horns, depending on the offset, a small dune is ejected. This phenomenon of double ejection, the ejection of one main dune from the center and another one from the horn, we call 'breeding' (blue zone in Fig. 2.19 and Figs. 2.14(b), 2.15(b) and 2.16(b)). Collisions in this regime shows a qualitative similarity with the barchan field shown in Figure 2.13.

As the initial volume ratio increases, a smaller relative velocity favors the mass exchange and reduces the overlapping process, leading to the complete separation of both dunes. Nevertheless, the leaving dune lacks the central part of its windward side and cannot reach the stable barchan shape. Therefore, it splits into two new dunes, a phenomenon we call 'budding' (pink zone in Fig. 2.19 and Figs. 2.14(bu) and 2.15(bu) and top of Fig. 2.16(bu)). A similar phenomena was reported in experiments with sub-aqueous barchans (Endo and Taniguchi, 2004).

For a larger volume ratio and small lateral offset, the instability of the dune in front disappears and both dunes develop into barchans. Then, we observe again solitary wave behavior as is shown in Fig. 2.14(s) and the lower (s) in Fig. 2.15 (upper green zone in Fig. 2.19). In that case the dunes move with similar velocity and the mass exchange is the main process of the evolution of the hybrid state. The overlapping of both dunes is very small now and the emerging dune looses merely a small fraction of its tail. Effectively, during both regimes of solitary wave behavior, as depicted in green in Fig. 2.19,

it looks as if the smaller dune just crosses the bigger one while in reality due to mass exchange the two heaps barely touch each other. The differences with real solitary waves was pointed by Livingstone et al. (Livingstone et al., 2005) and discussed by Schwämmle et al. (Schwämmle and Herrmann, 2005b). The analogy is based on the initial and final state of the colliding dunes, and not on the specific mechanism of interaction, which is very different from the real solitary waves as shown in Figure 2.18.

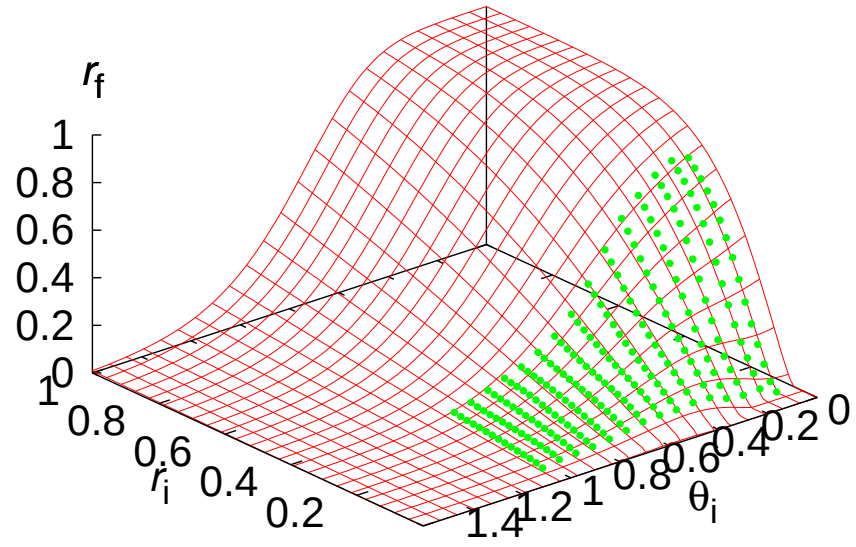

Figure 2.20: Volume ratio r_f after the collision as a function of the initial offset θ_i and the initial volume ratio r_i. Dots show the measured values obtained from the simulations.

The volume ratio r_f after a collision can be approximately expressed by the phenomenological equation,

$$r_f(\theta_i, r_i) \approx \left(1 - \exp\left(-A(\theta_i)(r_i - r_0(\theta_i))^{4/3}\right)\right) \tag{2.3}$$

valid for $r_i > r_0$. This condition takes into account that there is a minimal incoming dune of relative size r_0 below which no dune comes out, i.e a coalescence occurs (red zone in Fig. 2.19). The coalescence threshold r_0 is a function of the initial lateral offset θ_i, and is given by,

$$r_0(\theta_i) \approx 0.12\ \exp(-(\theta_i/0.4)^2) - 0.05 \tag{2.4}$$

This equation also defines a maximum offset $\theta_i \sim 0.4$ above which no coalescence occurs.

On the other hand, the term $A(\theta_i)$ represents the sensibility of the final volume ratio r_f to the initial offset θ_i,

$$A(\theta_i) \approx 10 \exp(-(\theta_i/0.36)^{1.3}) \tag{2.5}$$

Figure 2.20 illustrates the shape of $r_f(r_i, \theta_i)$ compared to the measurements (dots) obtained from the simulations with DUNE. We analyzed simulations with different offsets θ_i for seven different values of r_i.

Additionally, the lateral positions of both dunes change after the collision. No simple rule could be found and thus we do not consider the final offset.

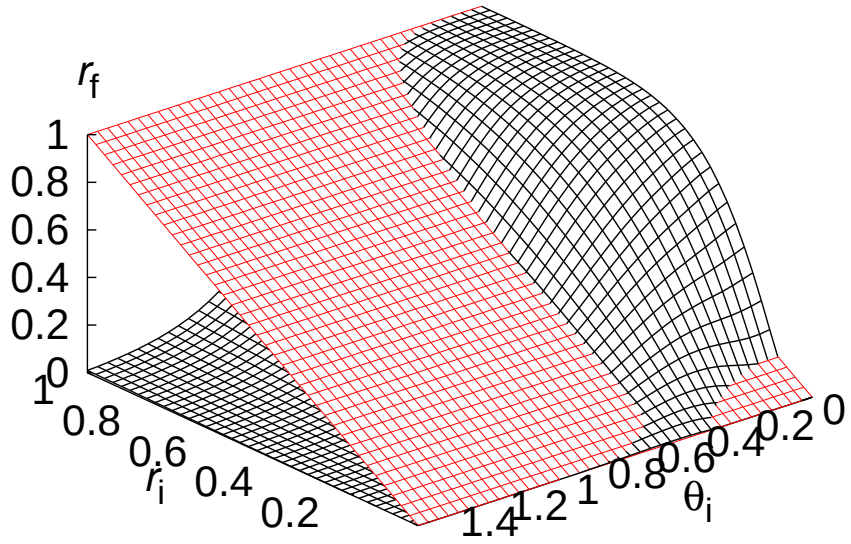

Figure 2.21: Volume ratio r_f after the collision as a function of the initial offset θ_i and the initial volume ratio r_i. The plane $r_f = r_i$ is also plotted in order to show the regions of phase space where the total sand volume is redistributed between both dunes after collision ($r_f > r_i$) or is accumulated by the bigger one ($r_f < r_i$).

The morphological phase diagram crucially influences the evolution of the number of dunes in a barchan field. In the coalescence region the number of dunes decreases by one, whereas two dunes in the 'breeding-budding' region appear, and the number of dunes increases by one. Finally, in the solitary waves region a small dune seems to cross the bigger one and the number of them remains constant.

The collision process also changes the volume distribution of the dunes in a barchan field. Figure 2.20 shows the volume ratio after the collision as a function of the initial volume ratio and lateral offset, along with a plot of the plane $r_f = r_i$. Since their sizes are not constant in time, due to the permanent exchange of sand between the dunes and its intrinsic instability (Hersen et al., 2004), we use the volumes of the dunes immediately before and after they leave the hybrid state. As a result of the interaction, the relative volume strongly increases for offsets less than about 0.8 and most of the initial volume ratios, $r_f > r_i$. In this case the collision process redistributes the initial mass making both dunes more similar, giving rise to a size selection mechanism in barchan fields (Hersen et al., 2004). Whereas for offsets higher than 0.8 and $r_f < r_i$, the bigger dune before collision increases its size further taking mass from the smaller dune.

2.3.2 Dune size distribution driven by the collision dynamics

We consider now the simplest approach to a dune field model, namely, a system that consists of a large number of dunes, characterized only by their width, which interact exclusively through collisions between them. We study the evolution of the dune size distribution $N(w)$ in the entire field in order to check if the macroscopic behavior of the system approaches an absorbent state.

We use two kinds of initializations for the system. In the first the size of the initial dunes (their width) is uniformely distributed between 0 and some w_{max}. The second one generates all dunes with sizes differing only slightly from some previously chosen width w_{char} (strongly peaked distribution). The initial number of dunes is 1000 in our simulations. Other sufficiently large numbers provide the same macroscopic behavior of the system. During a simulation very small dunes are removed from the dune field. In order to simulate an entire dune field, we consider annealed interactions among the dunes. A new mutual lateral distance (offset) is tossed before each collision.

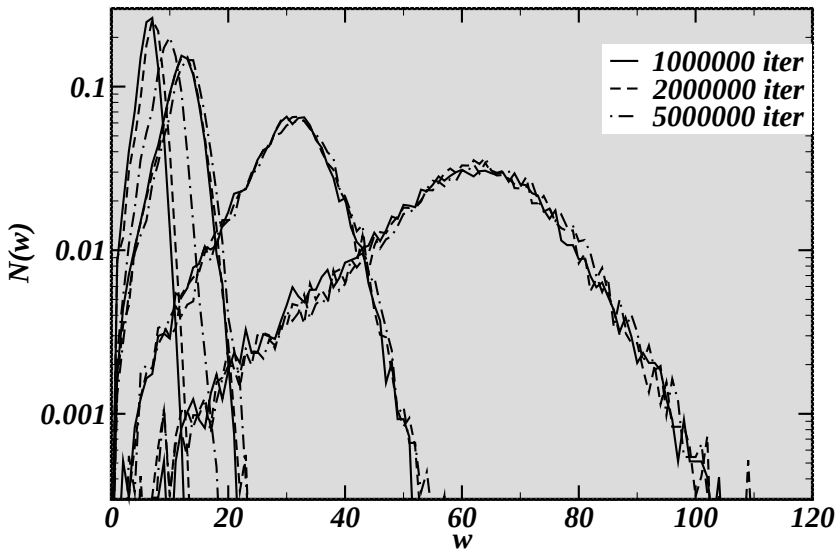

Figure 2.22: Histogram of the size distribution at different times. The field is initialized with a distribution strongly peaked around $w_{char} = 10, 20, 50, 100$ (from the left to the right). The figure shows that the final state is reached very fast (after about 100 collisions per dune) and a Gaussian size distribution is obtained.

For each collision two dunes are taken randomly from the field to collide. This is repeated every iteration as many times as the number of dunes in the field. If the second dune is larger than the first one, no interaction takes place. No new dunes are generated but the ones with size $w < 1$ are removed.

The outcome of a collision between the larger dune (width W) and the smaller one (width w) is, for simplicity, assumed to depend only on the relative mutual lateral distance, the

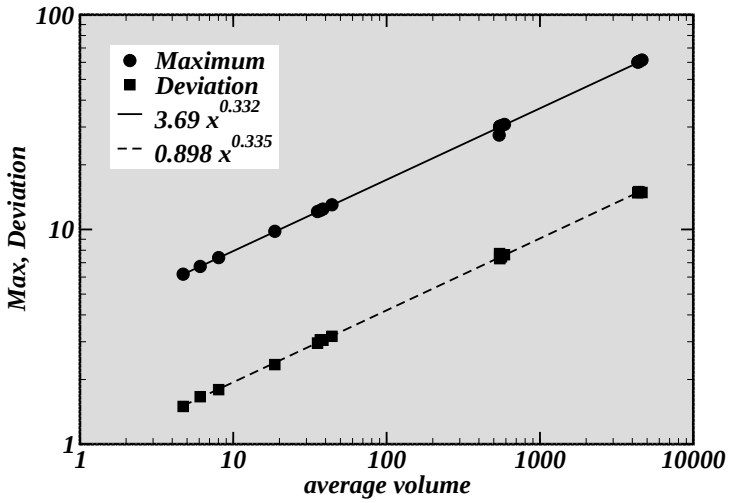

Figure 2.23: Half of the points (circles and squares) of the figure correspond to the simulations where the initialization was with a strongly peaked distribution. The other points (diamonds and stars) correspond to an initialization with an uniform distribution ($w_{max} = 10, 20, 50, 100$ from left to the right). The peak of the size distributions (circles and diamonds) as well as their deviation (squares and stars) increases with a power law of exponent $1/3$.

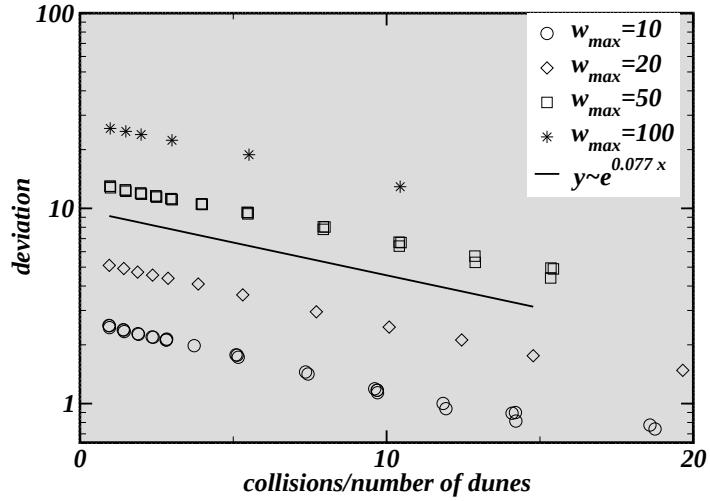

Figure 2.24: Evolution of the standard deviation of the size distribution with the number of collisions per dune. The points correspond to an initialization with an uniform distribution ($w_{max} = 10, 20, 50, 100$). At the beginning the deviation follows an exponential decay with a characteristic 'time' of about 12 collisions per dune (line).

random offset θ_i and the volume ratio $r_i = w^3/W^3$. The new volume ratio, r_f, is cast, according to the measurements presented above, through Eq. (2.3), and the conservation of the total volume of the two dunes, $V_{tot} = c(w^3 + W^3)$. As already mentioned above, Eq. (2.3) includes only solitary wave behavior and coalescence. We neglect here the creation of new small dunes by breeding. We choose the offset between the two dunes to be a random number distributed uniformly in the interval $[0, 0.8]$ at each collision. The limit of the maximum offset of 0.8 is due to the fact that the size of dunes colliding with an offset larger than the distance to the horns of the larger one generally is not altered.

The histograms in Fig. 2.22 show that dune sizes converge toward an absorbent state with a stable Gaussian–like distribution which peak around some width $\bar{w}$. The total mass of all dunes is conserved with the exception of a negligible amount due to the small dunes removed from the field. The convergence from the initial distribution to the Gaussian one is found to be a relaxation process with a characteristic time $t_c \sim 10$ *collisions per dune* which arises from the evolution of the standard deviation of the actual size distribution showed in Fig. 2.24.

The average volume $\bar{V}$ is a crucial quantity that determines the absorbent state of the simulations independent from the initial distribution of sizes. Figure 2.23 shows a reciprocal cubic increase of $\bar{w}$ versus $\bar{V}$. The distributions also become broader for larger $\bar{w}$ as observed in both figures. We calculate the root mean square deviation σ in the corresponding histograms. This deviation follows the same simple law as $\bar{w}$ versus $\bar{V}$. Therefore, the size distribution $N(w)$ only depends on the average volume of the field $\bar{V}$, namely

$$N(w) = \frac{1}{\sqrt{2\pi}\,\sigma} \exp -(w - \bar{w})^2/(2\,\sigma^2). \tag{2.6}$$

where $\sigma = a_s\,\bar{w}$, $\bar{w} \approx (\bar{V}/c)^{1/3}$ and $a_s \approx 0.24$ results from the fit.

We found that dune collisions could play a crucial role in selecting a characteristic size and in stabilizing the size distribution of a barchan dune field as mentioned in (Hersen and Douady, 2005). The simple model presented here certainly does not resamble real dune behavior. Especially the fact of neglecting the sand flux and the absence of a dependence of the dune interaction on geographic dune coordinates hinder us from providing a general picture of a dune field.

2.4 Effective model

Calculations of very large dune fields are still difficult because of high computational costs. The DUNE model reproduces the dune evolution at the scale of sand motion and thus is extremely expensive in terms of running time for large dune field simulations. One way out would be to consider a simplified 'coarse-grain' dune model (where sand dunes instead of sand grains are the basic objects) an effective model containing the main features of dune movement and interaction. For that purpose we use the collision rules obtained in the previous section on a larger scale together with the rules for the motion and evolution of barchan dunes developed in Chapter 1 based on the flux balance and mass conservation on a dune.

We consider a barchan dune field with constant unidirectional wind. The model describes a dune field of length (wind direction) x_{max}, $x = [0, x_{max}]$, and width y_{max}, $y = [0, y_{max}]$, fed by small barchans entering into the field (consider a beach giving rise to small dunes as shown in Fig. 2.8). The width w_0 of the incoming dunes is constant and they enter into the field at a rate ν, equal to the number of incoming dunes per time step. Their y-position is randomly distributed. We summarize the simulation parameters of the model in the table 2.1.

Each dune is characterized by its width w and its coordinates in the field, x and y. In each iteration the dunes change their size and position due to sand flux and collisions. New dunes are generated and others disappear. A detailed description of the algorithms working on the dunes during each iteration is provided below:

Sand flux: First the dunes of the field are arranged in the order of increasing x-positions. Then, the influx of the field is set to 0 and thus yields the input of the first dune counted in the above described order. The dune outflux determines the volume al-

Table 2.1: Parameters of the simplified dune field model

dune parameters	
proportionality constant of the dune outflux-influx relationship:	$a = 0.45$
offset of linear relation between outflux and influx:	$b = 0.1$
relation between volume and width:	$c \approx 0.017$
dune velocity constant:	$\alpha \approx 50$
fixed model parameters	
time step:	$\Delta t = 0.001$ yr
Maximum number of iterations:	$T = 10^6 \equiv 10^3$ yrs
field width:	$y_{max} = 3$ km
field length:	$x_{max} = 20$ km
saturated flux:	$Q = 300$ m^2/yr
dune field influx:	$q_{f,in} = 0$
model parameters	
incoming dune's rate	ν
size of incoming dunes	w_0

teration and thus the dune's new width. The flow field is updated at the corresponding position of the dune. The normalized outflux q_{out}/Q of the dune, given by (Eq. (1.75)), determines the width of its horns, $w_h = (1/2)w\, q_{out}/Q$.

The horns define the part of the dune at which the sand leaves with nearly the intensity of the saturated flux Q. The remaining part of the dune is dominated by the dune's slip face where almost no sand leaves. In this simplified picture the sand flux out of a dune is Q through the horns and zero in between. In the limit case $w_h > w/2$ we set $w_h = w/2$.

The dune width evolves in time according to Eq. (1.78), namely

$$w^2(t + \Delta t) = w^2(t) + \frac{2Q\Delta}{3c}\Delta t. \tag{2.7}$$

Meanwhile, the dune moves forward a distance Δx that results from the integration of the dune velocity-width relationship given by Eq: (1.72), yielding

$$\Delta x = \frac{3c\alpha}{\Delta}(w(t + \Delta t) - w(t)), \tag{2.8}$$

where $\Delta \equiv q_{in}/Q - q_{out}/Q = (1 - a)q_{in}/Q - b$ giving the flux balance on the dune for a given normalized influx q_{in}/Q.

The updated flux field corresponds to the influx of the next dune. This dune again updates the flux field by changing the flux at the corresponding x-position by the outflux through the horns while simultaneously changing its size or being eliminated from the field.

In order to resume the entire algorithm of the computation of the flux and corresponding dune size and dune position changes see Fig. 2.25.

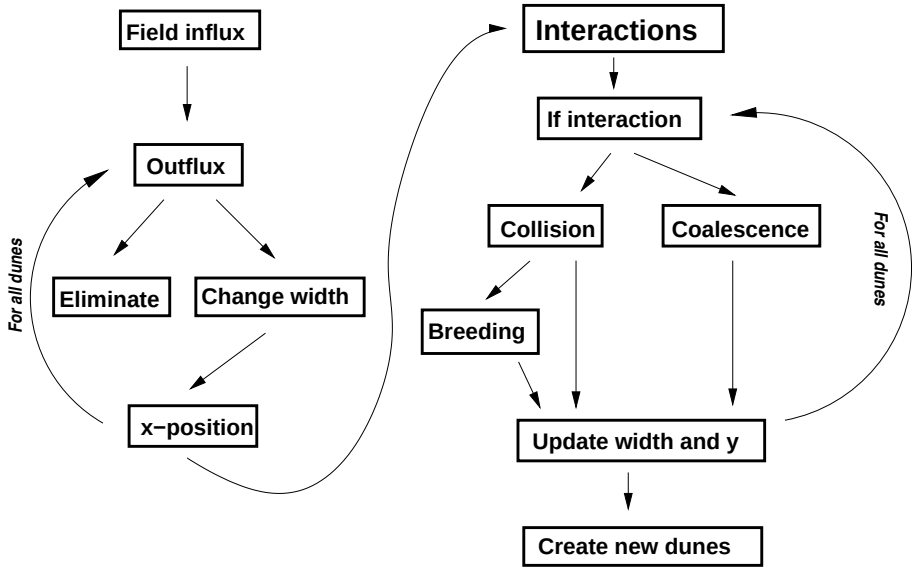

Figure 2.25: Illustration of the set of operations on the dune field executed in each time step.

Collisions: After updating all dunes according to the actual sand flux of the field at their position, we look if their new positions and sizes lead to collisions or coalescence. First, we check if a dune overtook another one and if they additionally overlap in their lateral extension. In this case, the collision rule, derived in section 2.13, is applied. In order to avoid an accumulation of several dunes of same size and similar position which correspond in reality to one, they are merged into one (coalescence) under the following conditions: they did not collide, their sizes do not differ more than one meter, their mutual distance in wind direction falls below the distance they move in an iteration and their lateral overlap exceeds 90%.

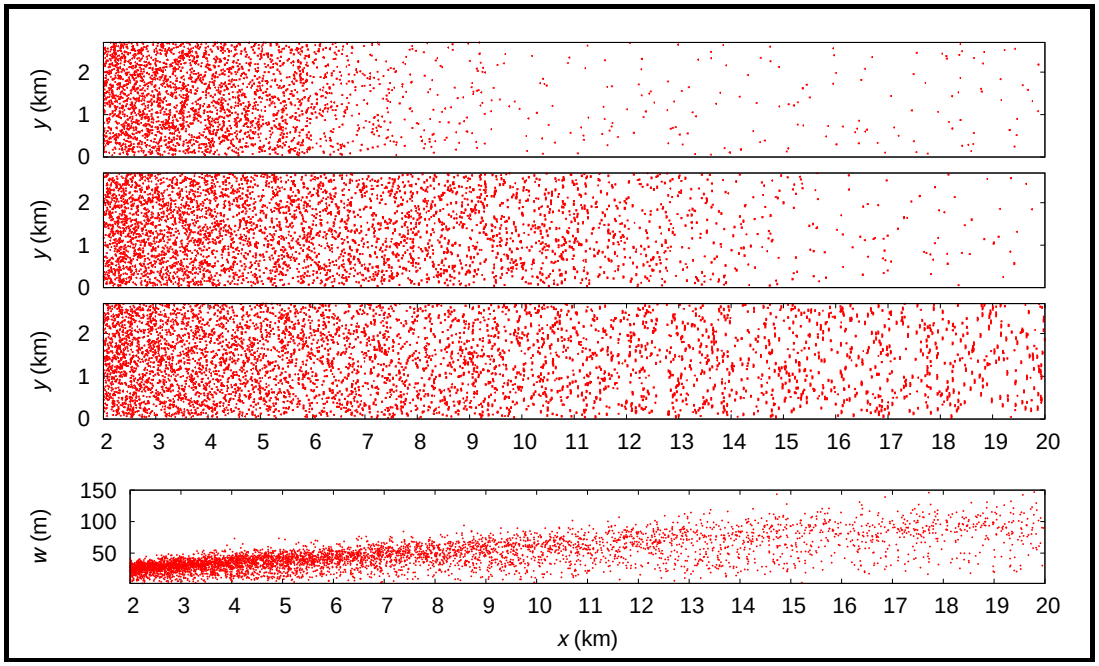

Figure 2.26: Top, three characteristic stages of the evolution of a dune field. Dunes move from left to right and are represented by the 'width line', i.e. a line centered in center of mass of the dune and with a width equal to the dune width. Bottom, dune width w as function of its distance downwind.

Results

We perform simulations for different dune input rates ν and sizes w_0. Since the incoming dunes are randomly distributed along the input boundary $x = 0$ we use the density ρ_0 of the incoming dunes instead of the input rate ν. From the definition, n dunes of width w_0 uniformly distributed in an area $A = y_{max}\Delta X$ has a surface density $\rho_0 \equiv (n\, w_0^2)/(y_{max}\Delta X)$ where y_{max} is the field width and $\Delta X = v\,\Delta t$ is the distance covered by the dunes of velocity $v = \alpha Q/w_0$ (Eq. (1.72)) during a time interval Δt equal to one time step. Since by definition the input rate is $\nu/\Delta t$, the dune density becomes

$$\rho_0 = \nu \frac{w_0^3}{\alpha Q y_{max}} \tag{2.9}$$

where the unknowns are given in table 2.1.

Figure 2.26 (top window) shows the evolution of a typical dune field with a high density ($\rho_0 = 0.42$) of about 2 m high incoming dunes ($w_0 = 20$ m). The dune field invades the whole simulated area and finally reaches a stationary spatial dune distribution. In general, along the downwind propagation of the dune field, the spatial distribution is not uniform, dunes become progressively sparce, and at the same time the dune size increases (Fig. 2.26, bottom). This 'coarsening' process is a direct consequence of the flux balance and apparently contradicts the measurements of real dune fields. However, at the scale where measured fields are clearly uniform, i.e. less than 4 km, simulated dune fields are also uniform.

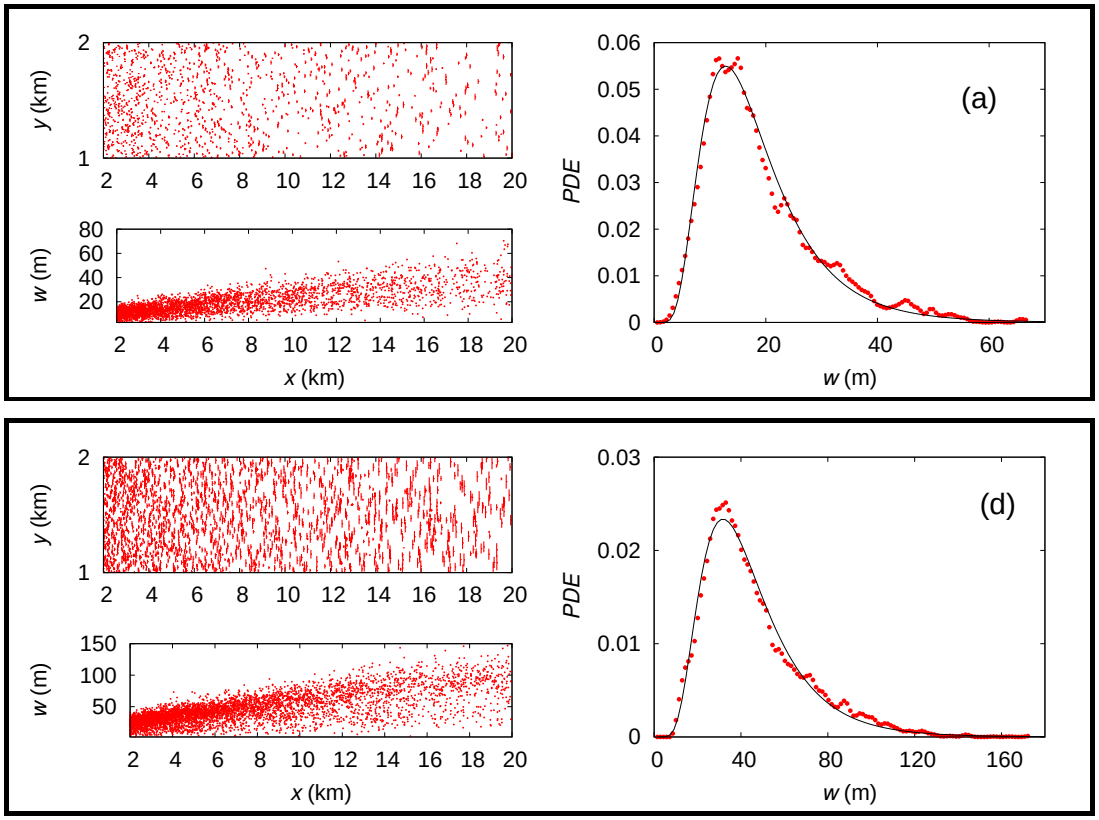

Figure 2.27: Dune width distribution of two simulated dune fields together with a snap shot of the field in the stationary state (top left) and the downwind dune size distribution (bottom left). In the distribution function, dots are measured points and the line is the lognormal fit. The boundary conditions are: (a) $w_0 = 10$ m, $\rho_0 = 0.18$, and (b) $w_0 = 20$ m, $\rho_0 = 0.42$.

Furthermore, the dune width distribution of the simulated fields are also well described by lognormal distributions (Fig. 2.27) whose mean size and standard deviation only depend on the boundary conditions. The lognormality precludes an underlying multiplicative process in the selection of dune sizes. We already know that collisions act as an additive process that leads to a gaussian size distribution. Every time two dunes are in contact we select a random lateral offset between them and apply the collision rule independent of the previous condition. However, now, besides collision, the flux balance on a dune is an important player. Since the outflux of one dune becomes the influx of the next one, and both the outflux and the influx are proportional to each other, a change, for instance due to

collisions, in one dune influences through the flux, the size of all dunes placed downwind it. Therefore, dune collision and the flux balance together act as a multiplicative process behind the lognormal size distribution. In the next section we will continue developing this with an analytical approach.

Finally, a detailed comparison between the spatial distribution of simulated and real dune fields is beyond the simplicity of the model we use since real dune fields experience fluctuating winds, they propagate over an inhomogeneous terrain, and dune collision under real conditions are far more complex than ours. Nevertheless, at a statistical level dune field properties are apparentely determined by the basic elements introduced here.

2.5 Analytical 'Mean-field' approach

In section 2.4 we established that the size distribution in a dune field is determined by the competition between the sand flux balance and collisions. The first one leads to a sand accumulation and thus to an increase of size, while collisions between dunes induce, in most of cases but not in all of them, a redistribution of sand, and therefore a decrease of size.

In this section we introduce this competition into an analytical formulation describing the evolution of the dune size distribution function.

Main equation

From an analogy with the classical Boltzmann equation, a statistical description of a dune system can be made in terms of dune width distribution function $\rho(w,t)$ such that $\rho(w,t)dwdt$ is the number of dunes at time t with width between w and $w+dw$.

We consider a dune field in which dunes interchange sand through the wind and assume initially that no collisions take place between them. In time dt the dune width w will change to $w+dw$. Thus, following dunes conservation, the number of dunes $\rho(w,t)dwdt$ is equal to the number of dunes $\rho(w+dw,t+dt)dwdt$, that is to say,

$$\frac{\partial \rho}{\partial t} + \dot{w}\frac{\partial \rho}{\partial w} = 0 \tag{2.10}$$

If, however, collisions do occur between dunes there will be a net difference between the dunes number $\rho(w+dw,t+dt)dwdt$ and $\rho(w,t)dwdt$. This can be written as $\Omega(\rho)dwdt$ where $\Omega(\rho)$ is the collision operator. This gives the following equation describing the evolution of the dune's volume distribution function

$$\frac{\partial \rho}{\partial t} + \dot{w}\frac{\partial \rho}{\partial w} = \Omega(\rho) \tag{2.11}$$

The rate of width change $\dot{w}$ due to the flux balance on the dune, was deduced in the previous chapter (Eq. (1.78)) and reads

$$\dot{w} = \frac{Q\Delta}{3c\,w}, \tag{2.12}$$

where $\Delta \equiv (1-a)q_{in}/Q - b$ contains the information of the flux balance. A positive Δ leads to the dune growth which shrinks otherwise.

Collision term

In the simplest approach, the collision term is substituted by the phenomenological term that arises from the analysis of binary collision dynamics

$$\Omega(\rho) = \frac{\rho_c(w) - \rho(w,t)}{t_c} \tag{2.13}$$

where t_c is the characteristic relaxation time of $\rho(w)$ towards the equilibrium distribution $\rho_c(w)$ when only collisions are considered (i.e. when $\dot{w} = 0$). Taking into account only dunes collisions, we already found that the dune width is normal distributed with mean $\bar{w}$ and standard deviation $\sigma = a_s\bar{w}$, where $a_s \approx 0.24$.

Final equation

Based on the diffusion of the inter-dune sand flux we assume that the dune influx is common for all dunes. Thus, the flux balance term simply becomes $\langle\Delta\rangle \equiv (1-a)\langle q_{in}/Q\rangle - b$, where $\langle q_{in}/Q\rangle$ is the average interdune flux. In the following, we assume that the average flux balance in the dune field is positive i.e. $\langle\Delta\rangle > 0$ and therefore, $\langle q_{in}/Q\rangle > (1-a)/b \sim 0.18$.

Substituting the rate of width change $\dot{w}$ (Eq. (2.12)), the collision distribution ρ_c (Eq. (2.6)) and the collision operator (Eq. (2.13)), into Eq. (2.11), we obtain the equation for the evolution of the dune width distribution function

$$\frac{\partial\rho}{\partial t} + \frac{Q\,\langle\Delta\rangle}{3\,c\,w}\frac{\partial\rho}{\partial w} = \frac{1}{t_c}\left(\frac{1}{\sqrt{2\pi}\,a_s\bar{w}}\exp -(w/\bar{w}-1)^2/(2\,a_s^2) - \rho\right) \tag{2.14}$$

or, using dimensionless variables

$$\frac{\partial\rho}{\partial\tau} + \frac{1}{\omega}\frac{\partial\rho}{\partial\omega} = \frac{t_s}{t_c}\left(\frac{1}{\sqrt{2\pi}\,a_s\bar{w}}\exp -(\omega-1)^2/(2\,a_s^2) - \rho\right) \tag{2.15}$$

where $\omega \equiv w/\bar{w}$ and $\tau \equiv t/t_s$ are the dimensionless width and time respectively. The dimensionless width ω is defined using the characteristic width $\bar{w}$ introduced by the collision dynamics. This characteristic width $\bar{w}$ also defines the characteristic time t_s of size change due to the flux balance, namely

$$t_s \equiv \frac{3c}{\langle\Delta\rangle}\frac{\bar{w}^2}{Q}, \tag{2.16}$$

already introduced in Chapter 1 (Eq. (1.80)).

2.5.1 Stationary dune's width distribution

We are interested in the stationary solutions of Eq. (2.15) which satisfy the equation

$$\frac{\partial\rho}{\partial\omega} = p\,\omega\left(\frac{1}{\sqrt{2\pi}\,a_s\bar{w}}\exp -(\omega-1)^2/(2\,a_s^2) - \rho(\omega)\right) \tag{2.17}$$

where the parameter $p \equiv t_s/t_c$ is the ratio of the two characteristic times of the problem.

Equation (2.17) represents a balance between the two main processes that determine the changes in dune size, the sand flux balance and collisions. This competition is encoded in the ratio p. When collisions dominate in the selection of dunes sizes, $t_c \ll t_s$ and consequently the distribution converges to $\rho_c(w)$. When the opposite occurs, the sand

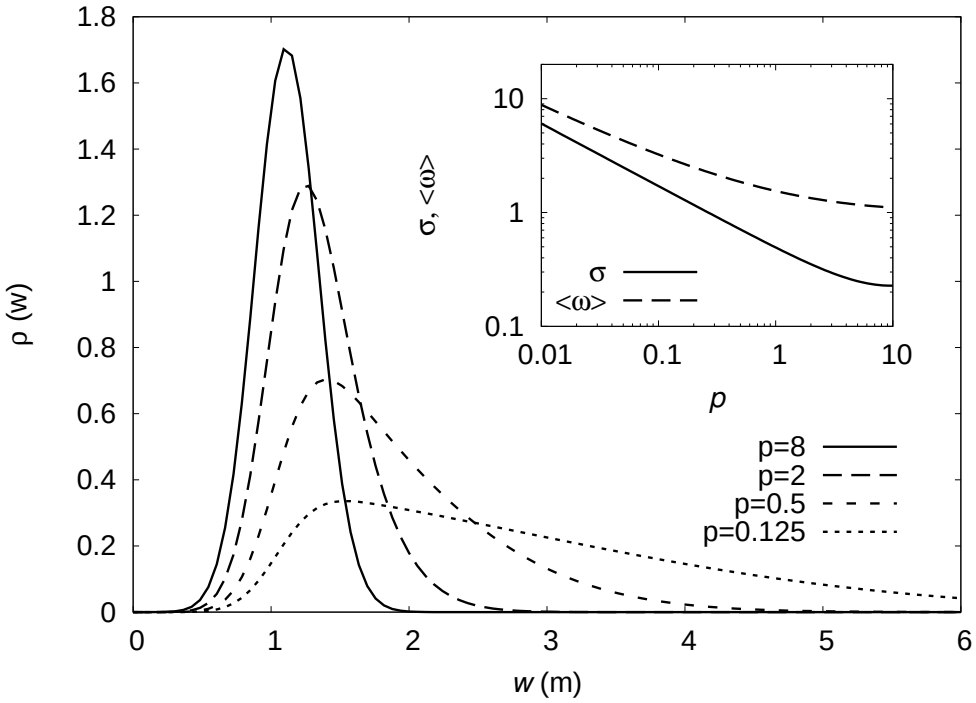

Figure 2.28: Analytical distribution $\rho(w)$ for different values of p. Inset: dimensionless mean $\langle\omega\rangle$ and deviation σ as function of p.

flux balance is the relevant process and $\rho(w)$ deviates from the gaussian distribution $\rho_c(w)$ converging toward an uniform distribution for large t_c compared to t_s.

Equation (2.17) with the boundary condition $\rho(0) = 0$ has the solution

$$\begin{aligned}\rho(\omega) &= \frac{p}{2\bar{w}A^{3/2}}\exp\left[-\frac{p}{2}\left(\omega^2-\frac{1}{A}\right)\right]\left(erf\left(\frac{1}{\sqrt{2A}\,a_s}\right)-erf\left(\frac{1-A\omega}{\sqrt{2A}\,a_s}\right)\right)\\ &\quad+\frac{a_s\,p}{\sqrt{2\pi}\bar{w}A}\left(\exp\left[-\frac{1+p\,a_s^2\omega^2}{2\,a_s^2}\right]-\exp\left[-\frac{(\omega-1)^2}{2\,a_s^2}\right]\right)\end{aligned} \tag{2.18}$$

where $A \equiv 1 - p\,a_s^2$ and $erf(x)$ is the error function defined as

$$erf(x) \equiv \int_0^x dx' \exp -x'^2. \tag{2.19}$$

In order to simplify the solution we assume that $A \sim 1$, i.e. $p \ll a_s^{-2} \approx 20$. In this case Eq. (2.18) reduces to,

$$\rho(\omega) \approx \frac{p}{2\bar{w}}\exp\left[-\frac{p}{2}(\omega^2-1)\right]\left(erf\left(\frac{1}{\sqrt{2}\,a_s}\right)-erf\left(\frac{1-\omega}{\sqrt{2}\,a_s}\right)\right), \tag{2.20}$$

which once normalized becomes

$$\rho(\omega) = \frac{\sqrt{p}}{2\,\bar{w}M}\exp\left[-\frac{p}{2}\left(\omega^2-1\right)\right]\left(erf\left(\frac{1}{\sqrt{2}a_s}\right)-erf\left(\frac{1-\omega}{\sqrt{2}a_s}\right)\right) \tag{2.21}$$

where the normalization constant M is equal to

$$M = \frac{\sqrt{p}}{2}\int_0^\infty d\omega \exp\left[-\frac{p}{2}(\omega^2-1)\right]\left(erf\left(\frac{1}{\sqrt{2}a}\right) - erf\left(\frac{1-\omega}{\sqrt{2}a}\right)\right) \tag{2.22}$$

Figure 2.28 depicts the analytical size distribution ρ for different values of p, while the inset shows the first two moments of the distribution: the dimensionless mean $\langle\omega\rangle$ and the dimensionless standard deviation σ, as functions of p. As was already shown above, for high values of p, collisions are predominant and the distribution converges to a gaussian with dimensionless mean $\langle\omega\rangle = 1$ and dimensionless standard deviation $\sigma = a_s$. While the distribution is increasingly uniform for small p values when flux balance is the relevant mechanism for size change.

In the range $p < 10$, the dimensionless mean of the distribution is approximately given by

$$\langle\omega\rangle \approx 0.8/\sqrt{p} + 0.7 \tag{2.23}$$

while the dimesionless deviation is given by

$$\sigma \approx 0.5/\sqrt{p} + 0.013p^{0.85} \approx 0.5/\sqrt{p} \tag{2.24}$$

where the second approximation is valid for $p < 5$.

2.5.2 Comparisons

We use a dimensional version $\rho(w)$ of the analytical distribution given by 2.21 to fit the measurements in the dune field of Morocco, i.e.

$$\rho(w) = \frac{\sqrt{p}}{2\,\bar{w}M}\exp\left[-\frac{p}{2}\left(\frac{w^2}{\bar{w}^2}-1\right)\right]\left(erf\left(\frac{1}{\sqrt{2}a_s}\right) - erf\left(\frac{1-(w/\bar{w})}{\sqrt{2}a_s}\right)\right) \tag{2.25}$$

Figure 2.29 shows the fit of the measurement data or, equivalentely, to the lognormal distribution, using the analytical distribution Eq. (2.25) with two parameters: p and $\bar{w}$. Based on it, we can conclude that the analytical solution $\rho(w)$ in the selected range of p and $\bar{w}$ can be well approximated by the lognormal distribution function (Eq. (2.1)) having the first two moments fully determined by the ratio $p \equiv t_s/t_c$ and the characteristic width $\bar{w}$ through Eqs. (2.23) and (2.24). In a dimensional from, both the moments, the standard deviation S and the mean $\langle w\rangle$, are given by

$$S \approx \frac{\bar{w}}{2}\sqrt{\frac{t_c}{t_s}} \tag{2.26}$$

$$\langle w\rangle \approx 1.6\,S + 0.7\,\bar{w} \tag{2.27}$$

within the range $t_c > 0.2t_s$.

In other words, S^2 is a measure of the strength of sand flux balance in comparison with collision mechanism for the dune size selection. Therefore, through the analytical model

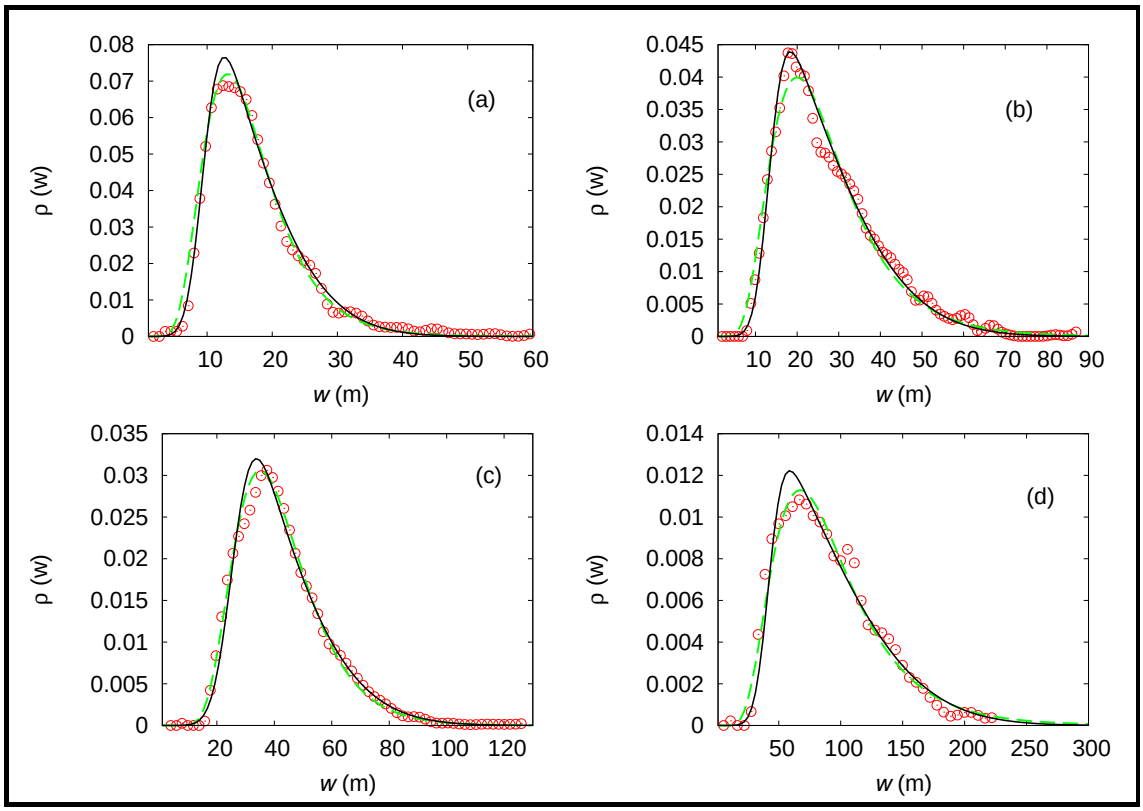

Figure 2.29: Comparison between the measured dune width distribution (dots), the log-normal fit (dashed line) and the analytical distribution (full line). The labels indicate the measured dune fields as presented in Fig. 2.5.

for the dune size distribution we arrive to a physical interpretation of the distribution parameters.

It is important to remark that, although the obtained distribution is not a lognormal function, it can be used, based on the similarities between both (Fig. 2.29), to uncover the physical origin of the lognormal parameters in real dune size distributions, one of our main questions in this chapter.

2.6 Scaling relations on a barchan dune field

While entire dune fields have been recently studied (Hersen et al., 2004; Elbelrhiti and Claudin, 2006), a global theoretical picture relating simultaneously dune field properties, features of local neighborhoods of single dunes and boundary conditions is still an open question, as recently mentioned in Ref. (Elbelrhiti and Claudin, 2006).

In this section we will present the main results from the different theoretical approaches developed in this Chapter.

From the analytical approach there is a new physical connection between the standard deviation of the lognormal dune size distribution and the ratio t_s/t_c of the characteristic time t_s of size change due to the flux balance and the relaxation time t_c due to collisions (Eq. (2.27)). The time t_s is defined in Eq. (2.16) while, from section 2.13, $t_c \approx n\,\tau_c$ where $n \sim 10$ and τ_c is the mean collision time between two neighboring dunes. However, by definition, τ_c is the mean time that one dune takes to reach the dune in front and thus, to cover a distance equal to the inter-dune spacing $\bar{L}$,

$$\tau_c \equiv \bar{L}/\langle v_r \rangle \tag{2.28}$$

where $\langle v_r \rangle$ is the average relative velocity between any two dunes. By using the lognormal size distribution, $\langle v_r \rangle$ is found to be proportional to the relative lognormal deviation $S/\langle w \rangle$,

$$\langle v_r \rangle \approx \frac{\langle v \rangle}{\sqrt{\pi}} \frac{S}{\langle w \rangle} \tag{2.29}$$

for a small σ-parameter of the lognormal, defined by Eq. (2.1), i.e. $\sigma < 0.5$. This range covers the experimental values arising from the fit. Besides, $\langle v \rangle = \alpha Q \langle 1/w \rangle$ is the average dune velocity in the field. Using again the lognormal distribution in the first approximation yields to

$$\langle v \rangle \approx \alpha Q / \langle w \rangle. \tag{2.30}$$

Substituting into Eq. (2.28), the relaxation time t_c, which characterizes the relevance of collisions in the size selection process, is given by

$$t_c \approx \frac{\sqrt{\pi}\, n}{\alpha\, Q} \frac{\bar{L} \langle w \rangle^2}{S}. \tag{2.31}$$

To get an idea of the time scales we are dealing with, under real conditions in Morocco, $t_c \sim 350$ yrs.

Therefore, collisions are important whenever dunes are closer, i.e. small $\bar{L}$, or the range of sizes is wider, i.e. large relative deviation $S/\langle w \rangle$, because in this case the relative dune velocity is also large. When dunes sizes are similar, there are few collisions and they are not as relevant in size selection as the flux balance. However, in this case, from Eq. (2.27), the deviation increases and the allowed size range is broad again. This feedback leads to an equilibrium between both processes and a selection of a relative deviation expressed by the equation

$$\left(\frac{S}{\langle w \rangle} \right)^3 \approx A \frac{\bar{L}}{\langle w \rangle} \tag{2.32}$$

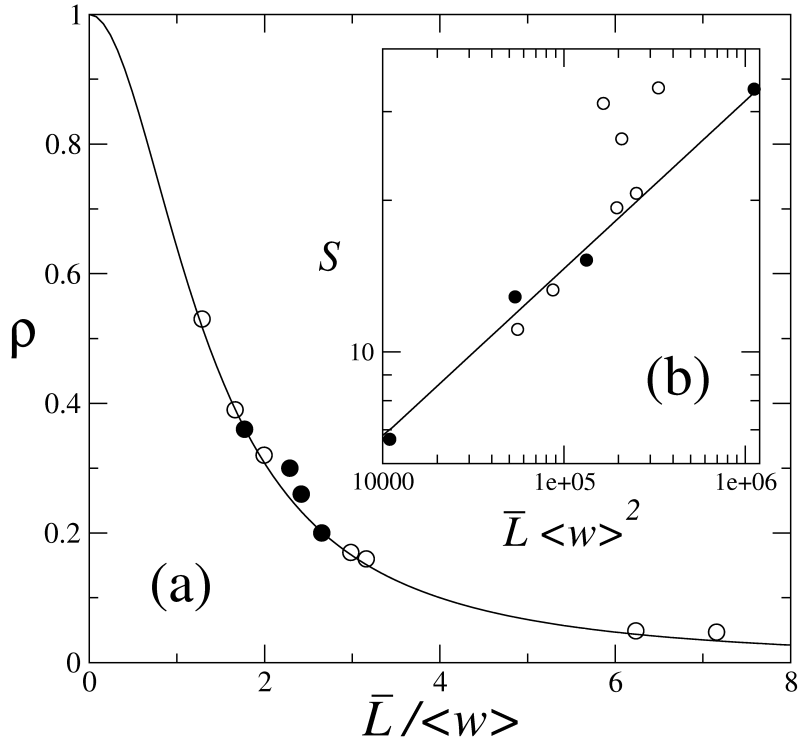

Figure 2.30: **(a)** Dune density ρ as a function of the relative inter-dune spacing $\bar{L}/\langle w\rangle$. In **(b)** one sees the dependence between S and $\bar{L}\langle w\rangle^2$ as a power law $x^{1/3}$. From this fit one obtains the constant of proportionality $A = 0.03$. For both cases one plots results of the real dune fields in Fig. 2.5 (•), of simulated dune fields (○) and the fit when both are taken into account (solid lines). The deviation of three simulated dune fields in (b) is related to high density profiles (see text).

which arises after the substitution of Eqs. (2.16) and (2.31) into Eq. (2.27). The constant A, defined as

$$A \equiv \frac{\sqrt{\pi}}{12}\frac{n\langle\Delta\rangle}{c\,\alpha} \tag{2.33}$$

contains the main parameters of barchan dune field, which are all given except the average inter-dune balance term $\langle\Delta\rangle$.

From Eq. (2.32), the relative broadness, i.e. $S/\langle w\rangle$ depends exclusively on the relative inter-dune spacing $\bar{L}/\langle w\rangle$. Through collisions, the dunes size distribution is related to their spatial distribution. Figure 2.30b illustrates this cubic scaling using real and simulated dune fields. Here, there are three simulated points that deviate from the constitutive relation because of their large density that results in frequent superposition of dunes, which should be considered as a single dune. This leads then to an underestimation of the average width and free-space distance which naturally explains why such points are deviated to the left in Fig. 2.30b.

Using Eq. (2.32) to fit real and simulated data (Fig. 2.30b) it is possible to calculate the average inter-dune balance term $\langle\Delta\rangle$ from Eq. (2.33), which gives $\langle\Delta\rangle \approx 0.017$. Based on the definition $\langle\Delta\rangle \equiv (1-a)\langle q_{in}/Q\rangle - b$ and the values of $a \approx 0.45$ and $b \approx 0.1$, one can then estimate the average normalized influx inside a dune field as $\langle q_{in}/Q\rangle \approx 1.17\, q_c/Q$.

Therefore, the average influx is not only apparently constant for the analyzed dune fields but also very close to the equilibrium influx $q_c/Q \approx 0.18$ at which dune outflux equals dune influx. Using this average influx and under Moroccan conditions the characteristic time for size change due to flux balance is $t_s \sim 400$ yrs, in the same range of the collision relaxation time t_c.

The relative inter-dune spacing also determines the dune field density ρ. From the definition of density $\rho \sim N\langle w\rangle^2/(N\langle w\rangle^2 + A_L)$ with N symbolizing the number of dunes and A_L being the free total area between dunes, and taking into account that A_L scales with $\bar{L}^2$, independently on the width w, one writes

$$\rho = \frac{1}{1 + \gamma \left(\bar{L}/\langle w\rangle\right)^2}, \tag{2.34}$$

where $\gamma \sim 0.6$ is a constant determined from Fig. 2.30a.

An important consequence from the combination of Eqs. (2.32) and (2.34) is that the statistical standard deviation S of the size distribution increases with the density, which is a spatial property characterizing the dune field. This connection between dunes density and the relative broadness of the size distribution will be very important in order to determine it from the general conditions at which a dune field is subject to, i.e. the boundary conditions.

2.6.1 Effects of the boundary conditions

Having a first picture of how the field properties relate with each other, we finally address the open question of why different dune fields have different densities and characteristic dune sizes. From the analysis of the simulated fields in Section 2.4, we found that the density and average width are, in fact, attached to the boundary conditions, namely the input density ρ_0 of dunes and the corresponding width w_0, determining the input of dunes into the field.

For the simulated dune fields, Fig. 2.31a shows that the average width follows the relation

$$\langle w\rangle = \left(\bar{W}\rho_0 w_0\right)^{1/2}, \tag{2.35}$$

where $\bar{W} \sim 225$ m is a threshold length determining whether the mean dune size in the field is lower or higher than the size of incoming dunes. In the ideal case without any interactions, the dunes entering into the field remain equal and the mean size is just their size w_0. Hewever, due to interactions, the incoming dunes change their size during their evolution through the dune field, and thus modifying the mean dune size in the field.

In this context, when incoming dunes are smaller than the product $\bar{W}\rho_0$, their density is high enough to enhance the sand exchange through flux balance and they will grow, increasing the mean dune size. Otherwise, if the incoming dunes are larger than $\bar{W}\rho_0$, then their density is too small compared to their size and there is not enough sand exchange between them. In this case they will shrink further inside the dune field, decreasing the mean dune size.

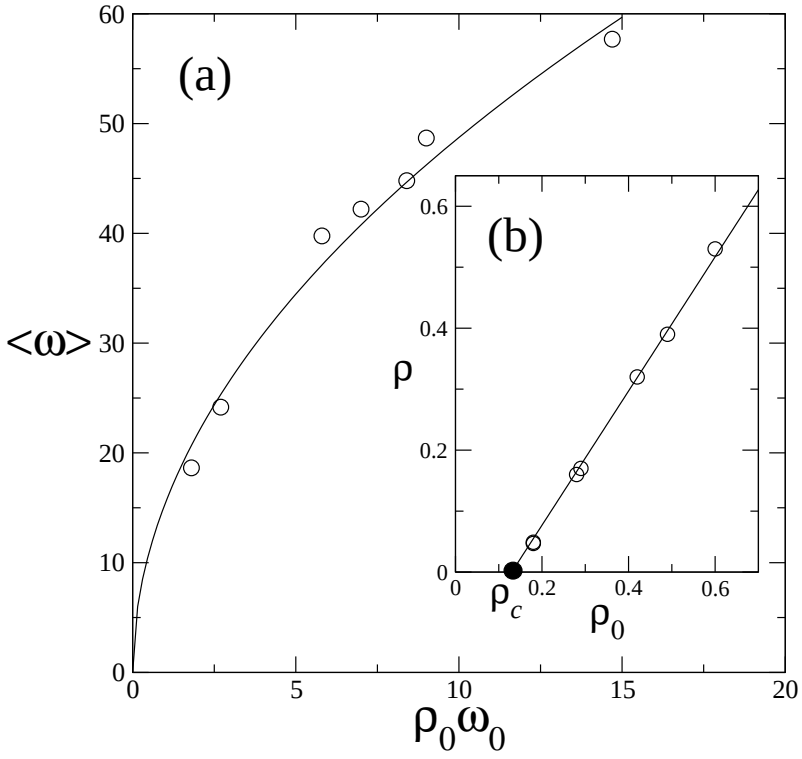

Figure 2.31: **(a)** The average width $\langle w \rangle$ as a function of the product between the boundary incoming dune density ρ_0 and the width w_0 of the incoming dunes at the boundary. **(b)** The final stationary density ρ of the dune field as function of the initial density ρ_0 at the boundary. Note that below ρ_c (black circle) no dune field formation can be attained.

Simultaneously, the dune density ρ in the field, plotted in Fig. 2.31b, scales with the initial density ρ_0 as

$$\rho = \rho_0 - \rho_c, \tag{2.36}$$

where $\rho_c \approx 0.12$ is a critical density below which the incoming dunes cannot sustain a growing process and are destroyed. Equation (2.36) can also be understood from the volume conservation: since the amount of sand blown into the field, encoded in ρ_0, has to be shared between the sand of the dunes, described by ρ, and the sand in the aerial layer, one expects that $\rho < \rho_0$ with the corresponding difference ρ_c denoting the density associated to the aerial sand flux.

Finally, through Eqs. (2.35), (2.36), (2.34) and (2.32), the boundary conditions w_0 and ρ_0 determine the main properties of dune fields, namely, the dune density ρ, the inter-dune spacing $\bar{L}$, the mean size $\langle w \rangle$ and its standard deviation S.

2.7 Conclusions

We have presented measures of dune size distributions and inter-dune spacing in four real dune fields in Morocco, finding that the size distribution is lognormal and the spatial distribution is uniform in all of them. The lognormality of size distribution precludes an underlying multiplicative process in the dune size selection, while the uniformity of spatial dune distribution gives strong evidence of dune collisions as a very important dynamical process.

In order to reproduce the morphology of dune fields we performed simulations using the DUNE model, by which we obtained quite realistic results. However, poor statistic prevents a better comparison with real dune fields, an important obstacle being the computational cost of large simulations. Nevertheless, these simulations confirmed the relevance of dune collisions in the whole field evolution.

The analysis of collisions of barchan dunes with lateral offset using the DUNE model showed that some regularity exists in the resulting sizes after the collisions. Some simple laws could be fit to resamble the outcome of such an interaction between two dunes. The resulting volumes can be understood to depend only on the initial offset and volume ratio. We applied these phenomenological rules to a simple model which investigates the effects of collisions on a dune field without considering the sand flux between them. The interesting point is that the distribution shows a Gaussian–like shape with respect to the one–dimensional extensions of the dunes, i.e. height, width and length, and not with respect to the volume as could have been expected. Therefore dune collisions are statistically an additive random process that leads to a well defined dune size.

A better approximation was obtained by including, besides binary collisions, flux exchange between dunes and their spatial evolution, into a ‘effective’ model for dune fields that treats dunes as single elements and therefore is by far more efficient than DUNE simulations. Dune field simulations using the ‘effective’ model show the measured lognormal size distribution and presents the competition between dune collisions and flux exchange as the multiplicative process behind it.

This competition was modelled following an analytical ‘mean-field’ approach using a master equation for the evolution of the dune size distribution function. The resulting analytical distribution, although not a lognormal, can be well approximated by it and gives a physical origin for the two lognormal parameters encoded in the first two moments of the distribution: the mean value and the standard deviation.

As a consequence, the standard deviation of the lognormal size distribution results from the balance between dune collision and flux exchange as dynamical processes that change the dune size. Since collisions are related to the spatial dune distribution, we found an equation relating the three main statistical and topological quantities of dune fields, namely the mean and standard deviation of the dune size distribution and also the characteristic space $\bar{L}$ separating neighboring dunes. Furthermore, using the results from the ‘effective’ model, we found that the condition at the dune field input boundary, namely the size of incoming dunes and their density, determines all statistical properties of the dune field.

In summary, although it has been assumed (Hersen et al., 2004) that $\bar{L}$ has rather well selected values within a dune field, here we gave clear evidence that it is a common feature in dune fields and additionally showed that the typical size distribution of dune fields is log-normal. By deriving also the relationship of these quantities with respect to the physical properties, namely density and collision time, and the density and width of dunes at the boundaries, we were able to provide a consistent picture of an entire dune field through a closed set of equations.

Chapter 3

Vegetation on dunes

Since pharaonic times mobile sand has been stabilized through plantations while conversely fields and woodland have been devastated by wind-driven erosion and coverage of sand (Fig. 3.1). This ancient fight between vegetation growth and aeolian surface mobility has evidently enormous impact on the economy of semi-arid regions, on coastal management and on global ecosystems. While empirical techniques have been systematically improved since dune fields in Aquitaine were fixed during the reign of Louis XIV and an entire specialty has developed in agronomy (Gilad et al., 2004; von Hardenberg et al., 2001; Tsoar, 1990), most approaches are just based on trial and error and there is still an astonishing lack of mathematical description and of quantitative predictability.

Figure 3.1: Illustration of the invasion of dunes onto fertile soils, showing the threat posed by dunes taken from the coastal area in northeastern Brasil.

In is this chapter we propose for the first time a set of differential equations of motion describing the aeolian transport on vegetated granular surfaces including the growth and destruction of the plants. Vegetation hinders sand mobility but also becomes its victim through erosion of the roots and coverage by sand. We start in Section 3.1 by introducing the parabolic dune and presenting measurements on the vegetation cover on some parabolic dunes in the Brazil coast. In Section 3.2 we present our model and use the new equations to calculate the morphological transition between barchans and parabolic

dunes. Furthermore, we introduce an index that determines the condition under which dune inactivation occurs. Finally we apply the model for a coastal system like a beach to study qualitatively the transition from a sandy to a vegetated landscape.

3.1 Parabolic dunes

Parabolic dunes are vegetated dunes that, when active, migrate along the prevailing wind direction. They arise under uni-directional wind and in places partially covered by plants and have a typical U shape with the 'nose' pointing downwind and the two arms pointing upwind, contrary to barchan dunes where the horns point downwind (Fig. 3.2). Vegetation covers most of the arms of parabolic dunes and a fraction of their nose which depends on the activation degree of the dune, i.e. how much the dune moves. An active parabolic dune has a sandy nose (Fig. 3.2) while an inactive one is almost totally covered by plants (Fig. 3.3). Plants are typically placed along the lee size of the dune, which is protected from wind erosion. On the contrary, the interior side exposed to the wind is devoid from vegetation. There, erosion is strong enough to prevent vegetation growth.

Figure 3.2: Active parabolic dunes (delineated in red) in Pecem along the Brasilean coast. These dunes are predominantely covered by grass (in dark). The arrow in the top left represents wind direction.

The migrating velocity of parabolic dunes is several times smaller than that of barchan dunes, and in general, they represent an intermediate morphologic state between fully active crescent dunes, like barchans, and fully inactive parabolic dunes. The activation degree of the parabolic dune is characterized by the vegetation cover pattern over it, which

Figure 3.3: Noses of marginally active parabolic dunes in Iquape along the Brasilean coast. These dunes are very old and can reach up to 50 m high. The vegetation that cover them consist mainly in trees and shrubs. Wind blows form right to left.

also gives information from the sand erosion and deposition pattern responsible from the motion of the dune.

3.1.1 Measurements and experimental method

Along the coast from Fortaleza to Canoa Quebrada, sand dunes are total or partially stabilized by vegetation. The climate change of the region, from semi-arid-sub-humid state to a wetter climate, amplifies the vegetation role as an active agent in the sandy landscape evolution.

In order to obtain information from the distribution of vegetation in real conditions, we went to Fortaleza during the rain season to measure the shape of some parabolic dunes and the vegetation over them. We measured the shape of seven parabolic dunes and some characteristic features of the vegetation that cover them (Fig. 3.4). These dunes are located in Iguape and Aquiraz, in the east of Fortaleza, and Pecem, Taiba and Paracuru, in the west.

By using satellite Landsat images and a topographic map we were able to select parabolic dunes with different degrees of inactivation and vegetation cover density. The top window in Fig. 3.4 shows three of the measured parabolic dunes in Aquiraz. The bottom window of Fig. 3.4 shows the other four dunes in order of activation. In general, the most active ones were located in Aquiraz and Taiba (showed in Fig. 3.4 top (a) and bottom (d), respectively), while those in Paracuru (Fig. 3.4 bottom (c) and (d)) were among the most inactive ones.

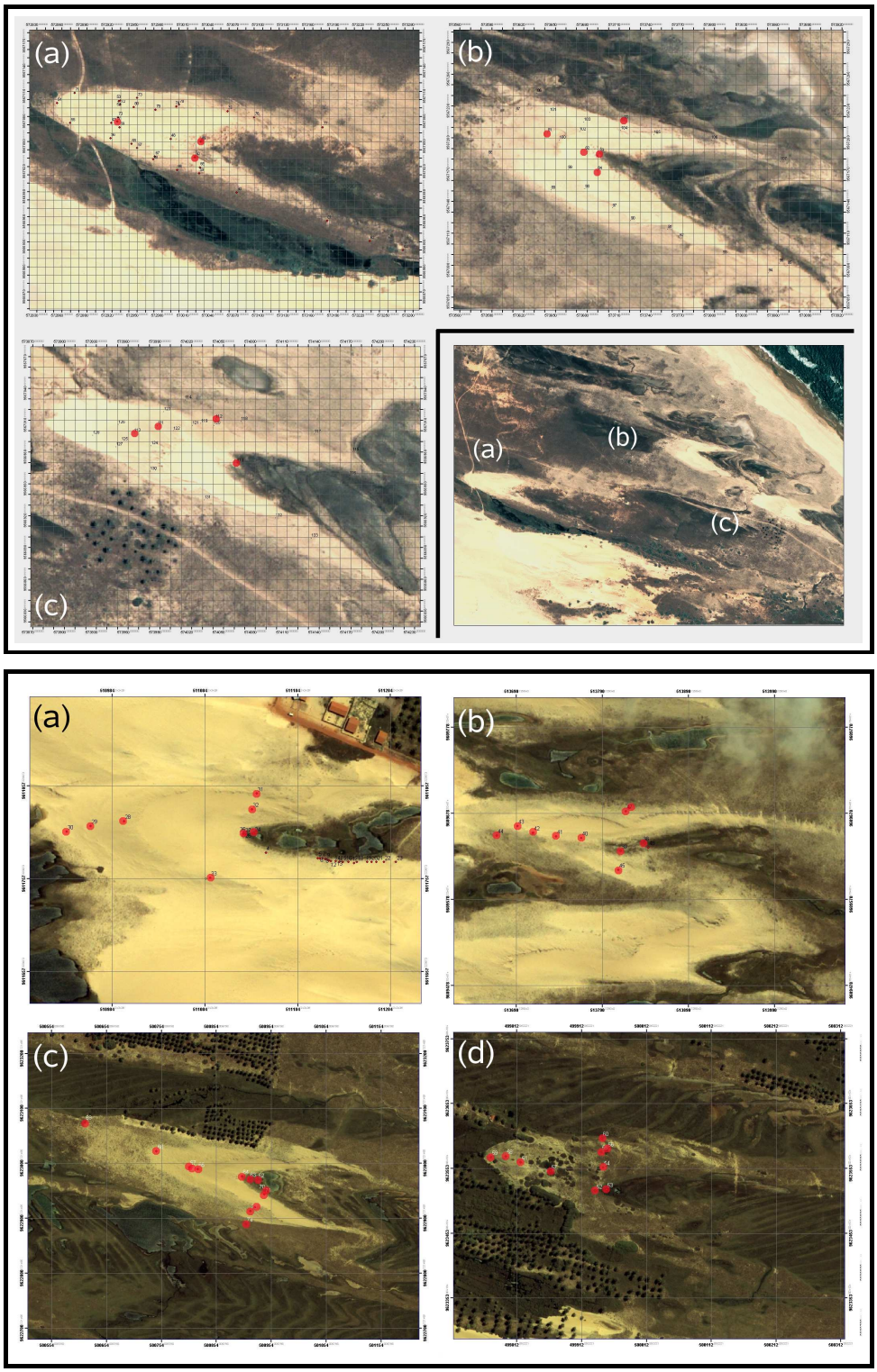

Figure 3.4: **Top:** three measured parabolic dunes in Aquiraz in order of activation, from the less active (a) to the most active (c). In (d) a view of the cluster from by these dunes. **Bottom:** the other four parabolic dunes from Taiba (a), Pecem (c) and Paracuru (c) and (d) in order of activation, the most active being (a) and the less active (d). Red dots indicate the location where vegetation was measured on each dune (see Fig. 3.6).

For all parabolic dunes we measure the geographical coordinates and height of the crest line, which includes the higher point, using a GPS devise with a internal barometer to measure height differences. We also measure some characteristic angles to compare with the sand repose angle and thus to define the avalanche face (slip face).

The vegetation cover over a dune is defined by the basal area density ρ_v, while the dynamical effect exerted by them on the wind, which is characterized by the drag force acting on plants, is determined by the frontal area density λ. Both densities, ρ_v and λ, are indirectly estimated from the number n_i, basal area a_{bi} and frontal area a_{fi} of each specie i of plants over a characteristic area A of the dune:

$$\rho_v \equiv \frac{A_b}{A} = \frac{1}{A}\sum_i n_i a_{bi} \tag{3.1}$$

$$\lambda \equiv \frac{A_f}{A} = \frac{1}{A}\sum_i n_i a_{fi} \tag{3.2}$$

where A_b and A_f are respectively the total basal and frontal plant area over the area A.

In these dunes mainly covered by grass we select five to ten points along the longitudinal and transversal main axes of the parabolic dune to measure the vegetation basal and frontal area density, inside a selected area of one square meter (red dots in Fig. 3.4). To do so we identify the species i of plant present in the dune counting the number of times n_i they appear in the study area $A = 1$ m^2 and measure their characteristic length, height and total leaf area (Fig. 3.5, left). The geographical coordinates of all points are recorded with a GPS and inserted in the digital dune map. Some species of the typical vegetation we found are shown in the right side of Fig. 3.5.

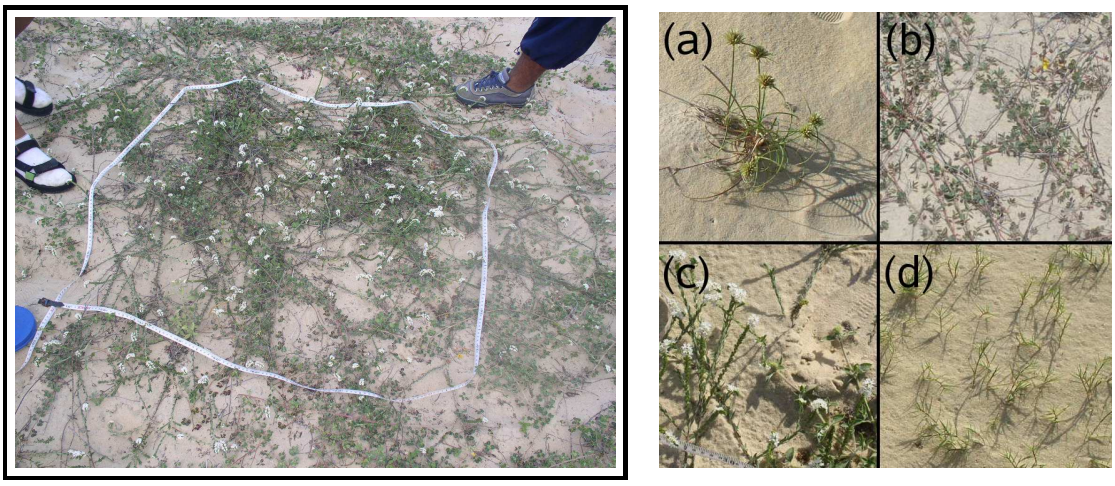

Figure 3.5: **Left:** example of the methodology used to measure the vegetation cover. **Right:** four typical species of plants found in the region where measurements were performed: cyperus maritimus (a), chamaecrista hispidula (b), heliotropium polyphyllum (c) and sporobolus virginicus (d).

In general, we found the same pattern in the distribution of vegetation in all measured parabolic dunes (Fig. 3.6). The area between the arms is totally covered by plants, which density reduces in the windward side where sand erosion is very strong and increases once again in the lee side, where most of the sand deposition occurs.

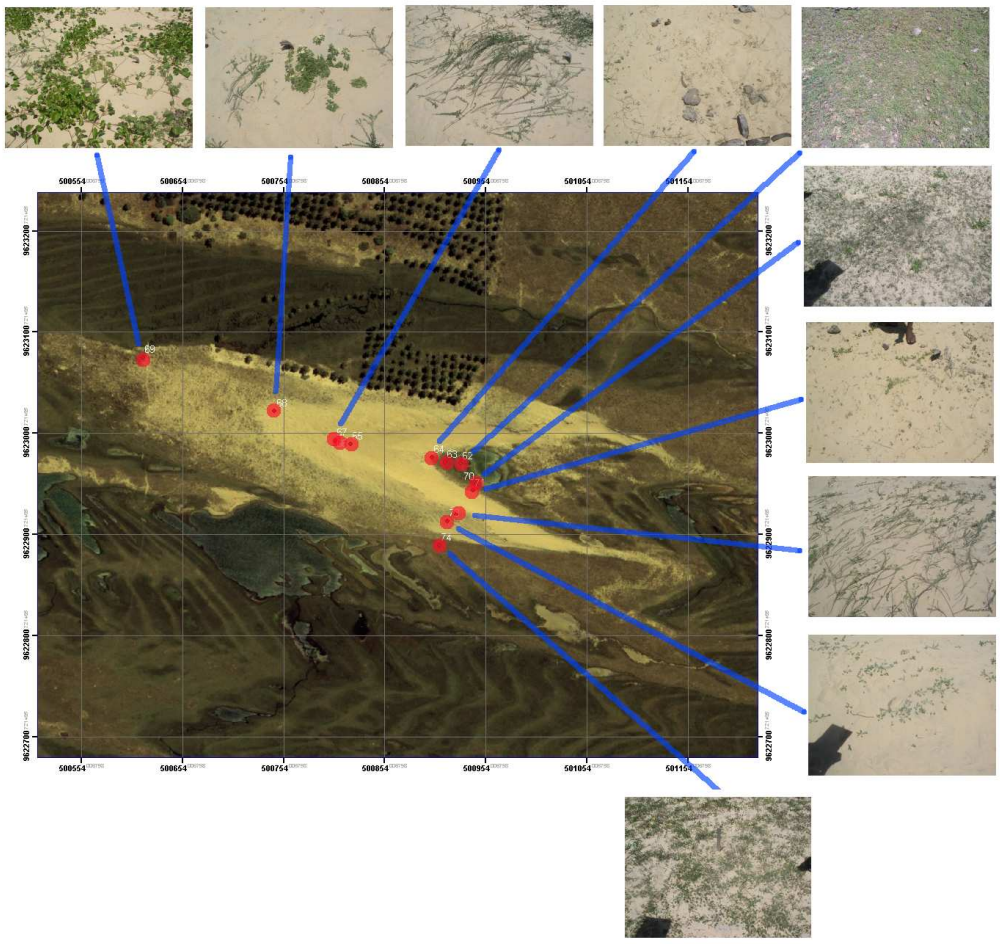

Figure 3.6: Satellite image of a typical measured parabolic dune with a close up to the vegetation growing in the different places over the dune. Red dots indicate the placed where vegetation data was collected.

Results

By using the collected vegetation data we were able to calculate, through Eqs. (3.1), the plant basal and frontal density at some particular points on the dunes. The first interesting result is that both densities are proportional each other (Fig. 3.7) with a proportionality constant $\sigma \sim 1.5$ with a low dispersion in spite of the different dunes and types of vegetation. Therefore, the plant basal density, also called cover density, ρ_v, can be used to characterize the interaction between vegtation and the wind strength, and, as shown below, will be very important for the modeling of the protective effect of vegetation against erosion.

In order to estimate the inactivation degree of the whole parabolic dune, based only on the plant cover density, we have to extend the sparse measured values of ρ_v to the full dune body. The grayscale of the satellite image (with a resolution 0.6 m/pixel) suggests that vegetation density should strongly contributes to the image darkness. Therefore, one crude approximation for the cover density in all the dune points is obtained by comparing

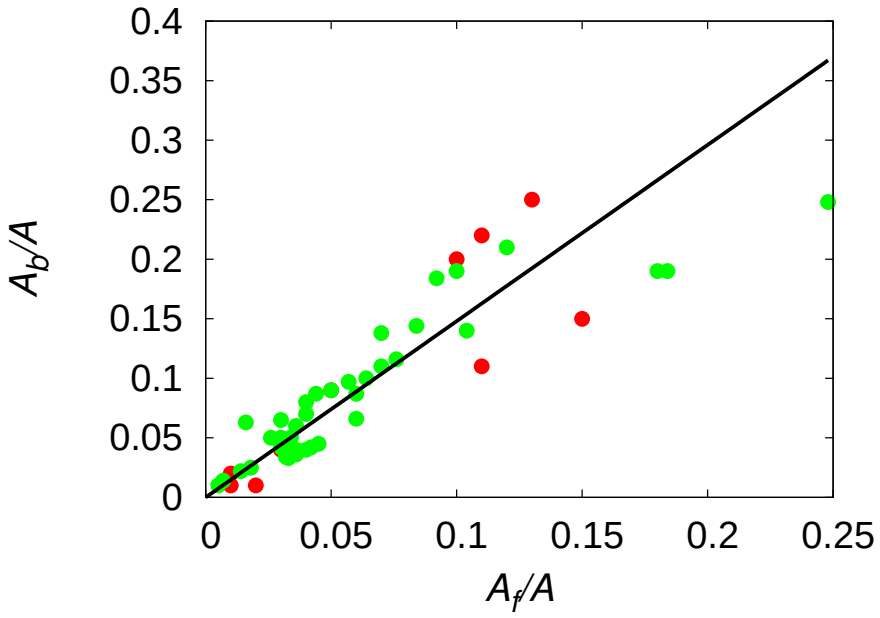

Figure 3.7: Proportionality between the basal density $\rho_v \equiv A_b/A$ and the frontal area density $\lambda \equiv A_f/A$. The proportionality constant of the fit (solid line) is $A_b/A_f = 1.48$. Each point represents a measured area in the dunes placed in Aquiraz, showed in Fig. 3.4 top, (red points) and the others dunes, Fig. 3.4 bottom,(green points).

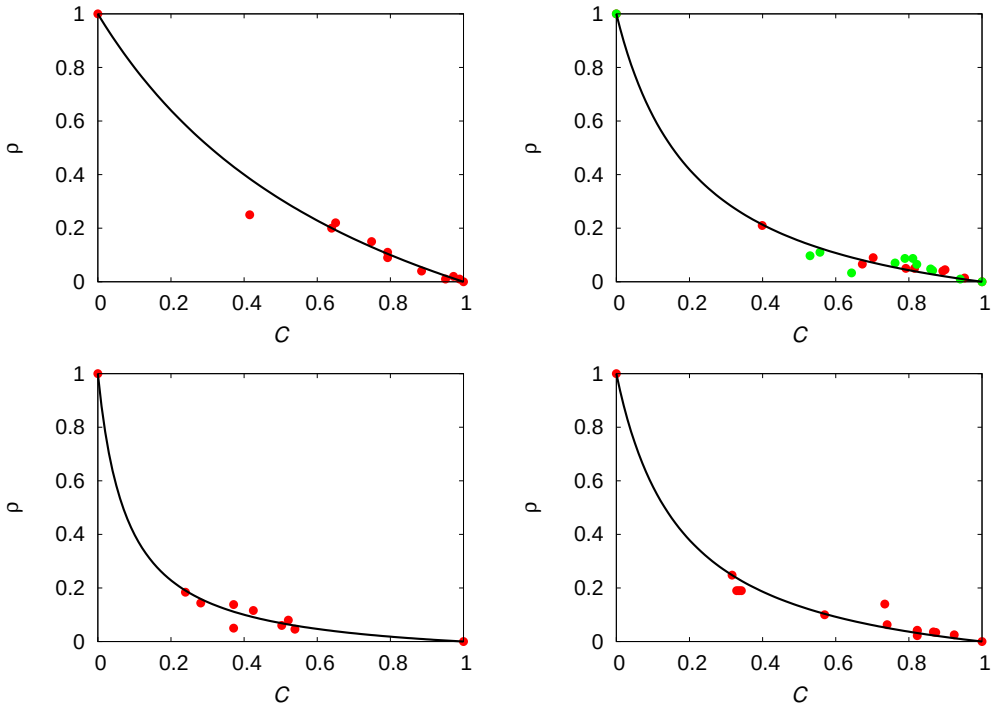

Figure 3.8: Relation between the vegetation cover density ρ_v and the normalized grayscale value C in the satellite image. Each point represents a measured area and different plots correspond to different images, which can contain one or more dunes.

the density cover ρ_v and the normalized image grayscale value C. This value is defined as

$$C \equiv \frac{c - C_{min}}{C_{max} - C_{min}} \tag{3.3}$$

where c is the grayscale value of a given point and C_{min} and C_{mac} are defined by the normalization conditions $\rho_v(C_{min}) = 1$ and $\rho_v(C_{max}) = 0$ respectively. These conditions are obtained from the analysis of those points in the image that one knows are either free of or fully covered by plants.

Figure 3.8 shows an apparent correlation between both ρ_v and C for each image. By assuming that the cover density decreases linearly when $C \to 1$ and that $\rho_v(C)$ is symmetric respect to the main diagonal, we propose the fitting curve

$$\rho_v(C) = a\frac{1 - C}{a + C} \tag{3.4}$$

where the fitting parameter a change for different images due to an alteration in the respective grayscale.

Equation (3.4) lead us to estimate the density cover of the whole parabolic dune. Figures 3.9 and 3.10 shows the resulting density cover calculated from the grayscale version of the images in Fig. 3.4. Blue represents free sand, while red represents total cover, and thus, total inactivation. With the help of the color-scale one easily identifies the zones where sand transport occurs. The windward side in the interior part of the arms is the most active section of the dune, as consequence of the erosion that prevents plants to grow. On the contrary, plants apparently can resist sand deposition and they accumulate clearly at the lee side and the crest of the dune.

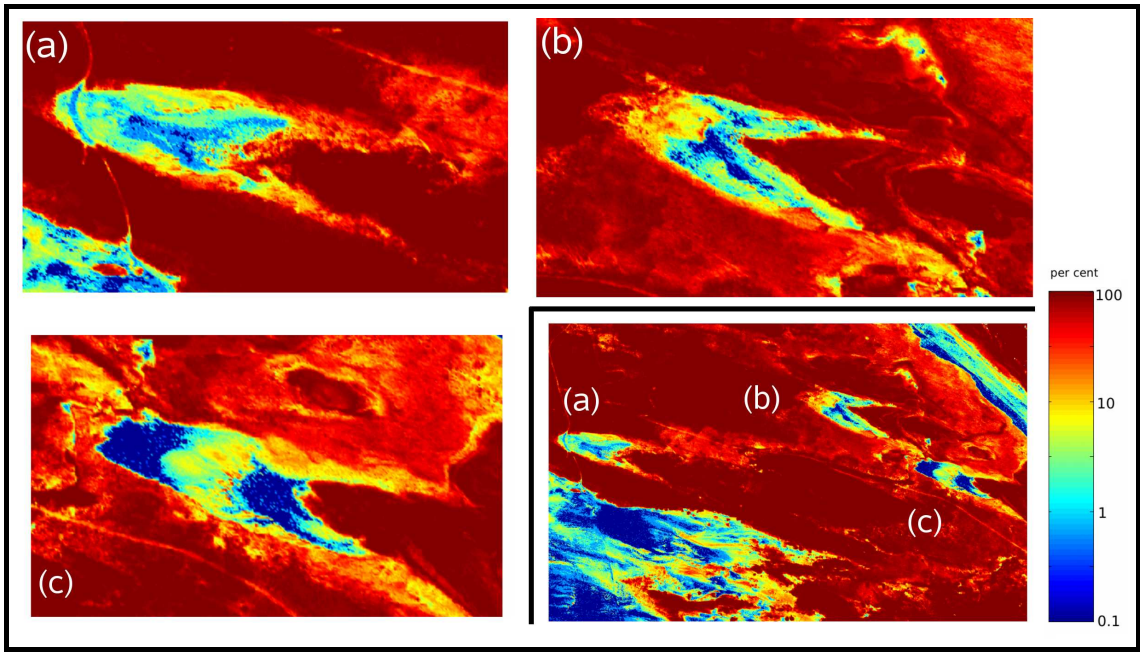

Figure 3.9: Vegetation cover density on the three parabolic dunes in Aquiraz, depicted in the top window of Fig. 3.4. Blue represent no cover $\rho_v = 0$ ($C = 1$) and red total cover $\rho_v = 1$ ($C = 0$). The logarithmic color scale is in percentage.

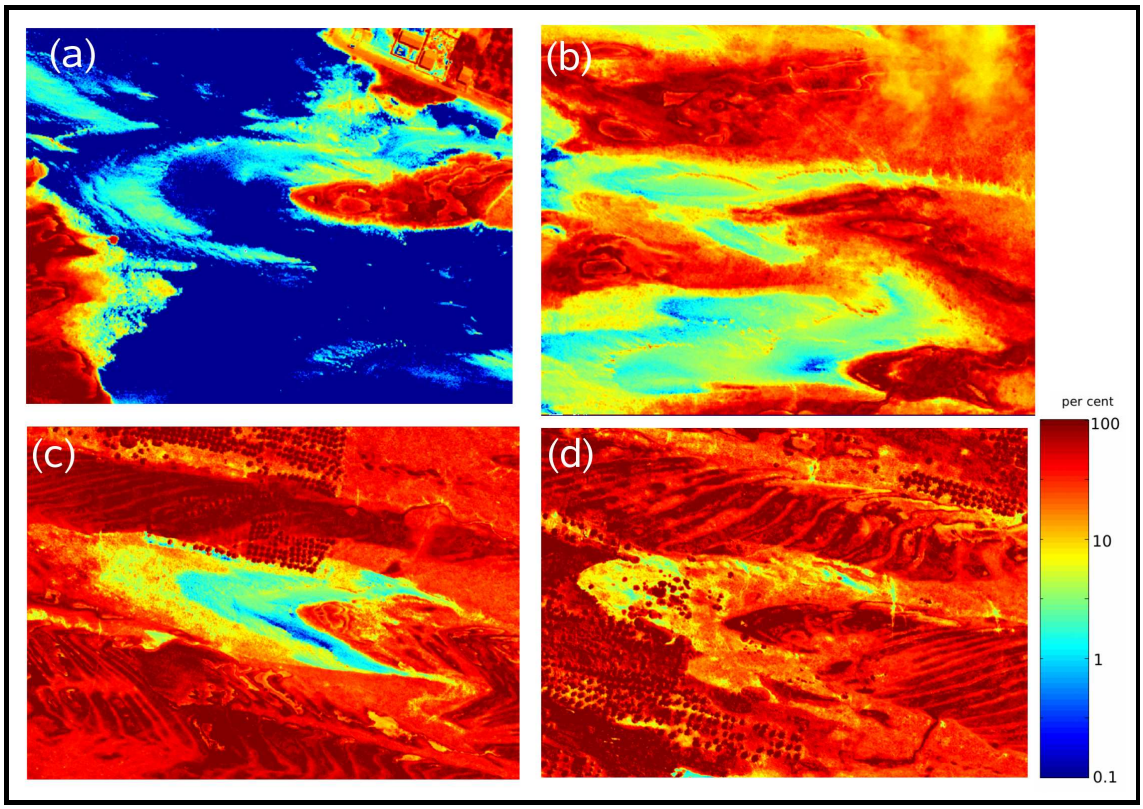

Figure 3.10: Vegetation cover density on the four studied parabolic dunes in Taiba (a), Pecem (b) and Paracuru (c) and (d), depicted in the same order in the bottom window of Fig. 3.4. Blue represent no cover $\rho_v = 0$ and red total cover $\rho_v = 1$. The logarithmic color scale is in percentage.

Another important conclusion is that the degree of activation of a dune apparently depends on its distance to the place where it was born. The three dunes in Aquiraz (Fig. 3.9) are deactivated according to their distance to the sea shore, the most active being the nearest to the sea (Fig. 3.9c). Similarly, the same occurs with the rest of the studied parabolic dunes.

In that way we can compare the empirical vegetation cover data with the result of our simulation to validate the distribution of vegetation over the dune. Through this we can estimate the degree of inactivation of the dune and reconstruct the previous dune history.

3.2 Vegetation against dune mobility

The sandy landscape is sculpted by an erosion-deposition cycle due to the interaction between the wind flow and the sand bed. The topography modifies the wind flow, which is accelerated uphill inducing erosion, and is retarded downhill, where sand is deposited, in a process that leads to dune formation and evolution. Here, vegetation plays a very important role by modifying the sand erosion-deposition pattern. Since plants locally slow down the wind, they can inhibit sand erosion, reducing the exposure of moist sand to the process of evaporation, as well as enhancing sand accretion (Fig. 3.11). Vegetation also traps particles of silt and clay suspended in the atmosphere which bind the surface sand grains and form a crust held together by cyanobacteria, algae and lichens (Danin, 1978; Danin, 1987). This algae crust not only becomes an important source of nutrients but enhances the sand moisture capacity, improving soil fertility (Zobeck and Fryrear, 1986), and reducing the saltation transport. All this provides a feedback mechanism that enhances vegetation growth (Tsoar, 1990; Tsoar, 2005).

Figure 3.11: Chamaecrista hispidula encroached over a dune present a barrier for sand transport. Ripples around are a sign of active saltation, while the pyramidal smooth surface after the plant represents the shelter area. Wind blows from left to right.

However, plants, as well, are affected by the sand dynamics. Since pure sand has no cohesion it is severely eroded by strong winds, denuding the roots of the plants and increasing the evaporation from deep layers. Although desert plants can resist to some degree nutrient deficiency, dryness, wind exposure, high temperatures and sand accretion, sand erosion often kills them (Danin, 1991; Hesp, 1991; Bowers, 1982). Thus, erosion

is the main limiting factor for vegetation growth on a sandy soil (Hesp, 1991; Bowers, 1982). Figure 3.12 shows the lateral side of a parabolic dune with dead vegetation on top of the internal side where sand transport occurs, and living vegetation outside.

The annual mean precipitation and the mean evapotranspiration are not determining factors for the development of vegetation, as occurs in fine soils like clay and silt (Tsoar, 1990; Tsoar, 2005), because, contrary to the popular belief, sand is an excellent medium for plant growth. Due to its coarse texture the rain penetrates at depths where it is protected from evaporation. Besides, sand does not need much water in order to have sufficient moisture to be above the wilting point (Tsoar, 1990; Danin, 1991). In areas devoid of strong sand erosion, perennial vegetation can be found with a mean annual rainfall of 50 mm, whereas many humid areas under high erosion rates are devoid of vegetation (Tsoar, 1990). As a result, there is a coupling between the evolution of the sand surface and the vegetation that grows over it, controlled by the competition between the reduction of sand transport rate due to plants and their capacity to survive sand erosion and accretion.

Figure 3.12: Crest of one arm of an active parabolic dune. In the interior side of the arm (left) sand is active and it erosion slowly uncovers the vegetation roots, killing them (dead plants are in dark). Outside the dune (right to the crest) vegetation survives sand accretion.

3.2.1 Vegetation model

The complex coupling between vegetation and aeolian sand transport involves two different time scales related, on one hand, to vegetation growth and erosion and deposition

processes that change the surface, and, on the other hand, to sand transport and wind flow. A significant change in vegetation or in sand surface can happen within some hours or even days. In contrast, the time scale of wind flow changes and saltation process is of the order of seconds, i.e. orders of magnitude faster. This separation of time scales leads to an enormous simplification because it decouples the different processes. Hence, we can use stationary solutions for the wind surface shear stress $\boldsymbol{\tau}$ and for the resulting sand flux $\mathbf{q}$, separately.

However, the evolution of the sand surface and the vegetation that grows over it remains coupled. Since plants locally slow down the wind, they can inhibit sand erosion as well as enhance sand accretion. This local slowdown of the wind shear stress represents the main dynamical effect of the vegetation over the wind field and consequently on the sand flux. The vegetation acts as a roughness element that absorbs part of the momentum transferred to the soil by the wind. As a result, the total surface shear stress $\tau \equiv |\boldsymbol{\tau}|$ can be divided into two components, a shear stress τ_v acting on the vegetation and a shear stress τ_s on the sand grains. When plants are randomly distributed and the effective shelter area for one plant is assumed to be proportional to its frontal area, the absorbed shear stress τ_v is proportional to the vegetation frontal area density λ times the undisturbed shear τ_s (Raupach, 1992; Raupach et al., 1993). Therefore, the fraction τ_s of total stress acting on sand grains is reduced to

$$\tau_s = \frac{\tau}{(1 - m\rho_v)(1 + m\beta\lambda)}\,, \tag{3.5}$$

where ρ_v is the vegetation cover density, β is the ratio of plant to surface drag coefficients, $\lambda = \rho_v/\sigma$ (see section 3.1) and σ the ratio of plant basal to frontal area. The term $(1 - m\rho_v)$ arises from the relation between the sandy and the total area. The constant m is a model parameter that accounts for the non-uniformity of the surface shear stress (Raupach et al., 1993; Wyatt and Nickling, 1997). If the plant frontal area density λ is zero there is no shear stress reduction. Otherwise, the reduction depends on the frontal area and on the plant drag coefficient encoded in β.

The time evolution of the sand surface height h is calculated using the conservation of mass,

$$\partial h/\partial t = -\nabla \cdot \mathbf{q}(\tau_s)\,, \tag{3.6}$$

defining the erosion rate $\partial h/\partial t$ in terms of the sand flux $\mathbf{q}$ resulting from a wind surface shear stress τ_s that includes the vegetation feedback.

In a simplified picture of vegetation growth, plants grow without changing shape, their effective height being proportional to their effective width. In that case, as was shown in section 3.1, their effective height h_v is a suitable property to characterize their geometry and their influence on sand transport since h_v is related with the vegetation cover density by $\rho_v = (h_v/H_v)^2$ (see Eq. 3.5).

Furthermore, in the absence of erosion or deposition, plants can grow until they reach a maximum height H_v, during a characteristic growth time t_v. Thus, the vegetation growth rate dh_v/dt is modelled by a simplified version of the Richards function (Richards, 1959) with an absolute growth rate $V_v \equiv H_v/t_v$ that does not depend on the plant size and a logistic saturation term: $dh_v/dt = V_v\,(1 - h_v/H_v)$. The characteristic growth rate V_v is determined by climatic or local conditions, such as watertable level and salinity, mean

annual precipitation, nutrient availability and soil evapotranspiration among others, that can enhance or inhibit the growth process (Danin, 1991; Hesp, 1991; Bowers, 1982). However, under small erosion or deposition, the sand surface changes and the vegetation needs time to adapt to it. This influence is modelled as a delay in the vegetation growth. Thus, the vegetation growth rate must include an additional term, yielding

$$dh_v/dt = V_v\,(1 - h_v/H_v) - |\partial h/\partial t| \tag{3.7}$$

where the first term on the right hand side represents the growth rate of the plant over a static surface, and the second term is the temporal change of the sand surface h. The relative strength of these two terms defines the ability of plants to survive surface changes.

This model for the interaction between plants and moving sand is closed by using the DUNE model described in detail in Chapter 1. Analytical calculations of the flow over a gentle hill yield an analytical expression for the topographically induced perturbation $\delta\boldsymbol{\tau}$ of the surface shear stress $\boldsymbol{\tau}_0$ on a flat bed (Weng et al., 1991), namely

$$\boldsymbol{\tau}(h) = \boldsymbol{\tau}_0 + \tau_0 \delta\boldsymbol{\tau}(h), \tag{3.8}$$

with $\tau_0 \equiv |\boldsymbol{\tau}_0|$, whereas the stationary sand flux $\mathbf{q}$ is given by the logistic equation

$$\nabla \cdot \mathbf{q} = q\,(1 - q/q_s)/l_s\,, \tag{3.9}$$

with $q \equiv |\mathbf{q}|$, $q_s \equiv |\mathbf{q}_s|$ and $\mathbf{q}_s(\tau)$ being the saturated sand flux, i.e. the maximum sand flux carried by the wind with a surface shear τ, and $l_s(\tau)$ is the characteristic length of saturation transients, called saturation length.

Given an initial sand surface, a surface shear stress τ_0 on a flat bed and a sand influx, the time evolution of the complete system is determined by the consecutive integration of the equations for $\tau(h)$, τ_s, $\mathbf{q}$, h and h_v.

3.2.2 Deactivation of barchan dunes

Migrating crescent dunes occupy about half of the total desert and coastal area under uni-modal wind condition (Wasson and Hyde, 1983), and they exist either as isolated barchan dunes in places with sparse sand or forming barchanoid ridges where sand is abundant (Fig. 3.13, top left). These migrating dunes can be deactivated by the invasion of vegetation, as seen in Fig. 3.13 (top), provided that there is a certain amount of rainfall and weak human interference (Tsoar, 1990; Tsoar, 2005). When the vegetation cover grows, barchans apparentely undergo a transformation into parabolic dunes with arms pointing upwind and partly colonized by plants (Fig. 3.13, top center-right), a metamorphosis that has been seen as the first step of dune inactivation (Hack, 1941; Anthonsen et al., 1996; Muckersie and Shepherd, 1995; Tsoar and Blumberg, 2002).

In the bottom of Fig. 3.13 one see the effect of growing vegetation on the mobility of a barchan that evolves under a constant uni-directional wind (Fig. 3.13a). Simulations where preformed using open boundary conditions with zero influx, since saltation does not occur on a totally vegetated ground. For the modeling of vegetation we use a ratio of

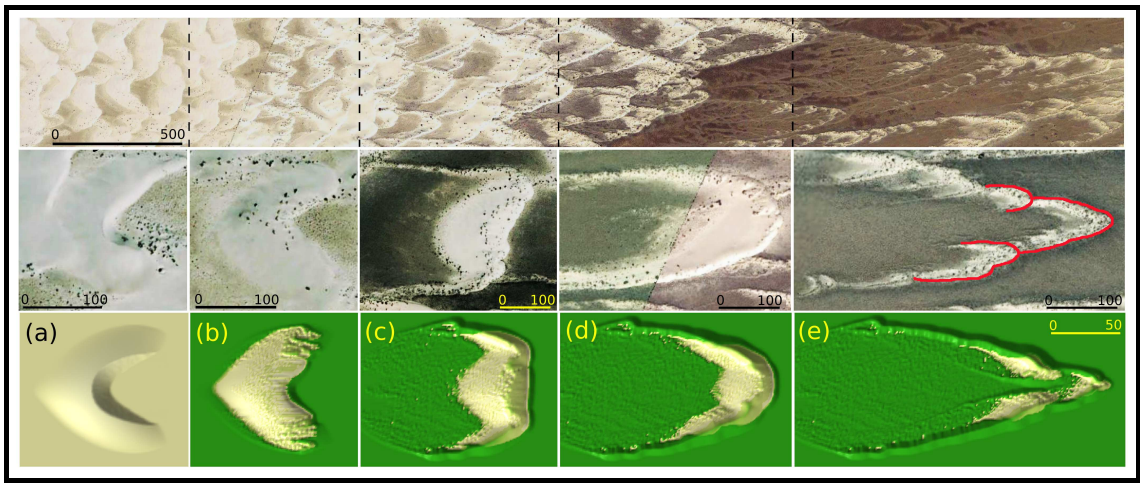

Figure 3.13: Deactivation of migrating dunes under the influence of vegetation. On top, a dune field in White Sand, New Mexico, that shows barchanoid ridges on the left, where vegetation is absent, developing towards a mixture of active and inactive parabolic dunes on the right (wind blows from left to right). Dark green regions indicate abundance of vegetation. This suggests a transition between both types of dunes when the vegetation cover increases. This transition is illustrated with various dune types found in the White Sand dune field (pictures in the middle), reinforcing the idea of their common evolution from a crescent dune. Satellite images taken from GoogleEarth. Below, same transition obtained by the numerical solution of a model that accounts for the coupling between sand transport and vegetation, with fixation index $\theta = 0.22$. The vegetation cover is represented in green.

plant to surface drag coefficients $\beta = 200$, which is an established value for a creosote community (Wyatt and Nickling, 1997), a maximum vegetation height $H_v = 1$ m, a ratio of plant basal to frontal area $\sigma = 1.5$, obtained from our Brazil data for grass, and $m = 0.16$, also from the creosote community (Wyatt and Nickling, 1997).

From Eq. 3.7 one concludes that plants will grow wherever $V_v > |\partial h/\partial t|$ even if under erosion conditions ($\partial h/\partial t < 0$) they cannot germinate due to the mobile sand surface. Therefore, we introduce an heterogeneous seeding by allowing plants to germinate only where no erosion occurs, establishing a competition for their survival with the mobile sand. Such a scenario could for instance be the consequence of the cessation of human activity (Tsoar and Blumberg, 2002), an increase of the annual precipitation or a reduction of the wind strength in a dune field (Anthonsen et al., 1996; R. and D., 1994), all of them stimulating conditions for vegetation growth.

Plants first invade locations with small enough erosion or deposition, like the horns, the crest and the surroundings of the dune. This vegetation reduces the strength of the wind and traps the sand which accumulates mainly where sand flux is the highest, i.e. at the crest. Consequently, the sand cannot reach the lee side anymore and deposits on the crest (Fig. 3.13b). This deposition kills the vegetation again. Thus the erosion/deposition rate at the crest is again lowered. This provides a cyclic mechanism for the vegetation growth on the crest.

As a result, the central part of the dune moves forward and two marginal ridges are left behind at the horns (Fig. 3.13c) in a process that leads to the stretching of the windward side and the formation of a parabolic dune (Fig. 3.13d). Finally, vegetation overcomes sand erosion even in the central part and the migration velocity of the parabolic dune dramatically drops about 80% indicating its inactivation (Fig. 3.13e). This process agrees well with a recent conceptual model based on field observations (Tsoar and Blumberg, 2002).

The transformation of barchans into parabolic dunes is determined by the initial barchan volume V, the undisturbed saturated sand flux $Q = |\mathbf{q}_s(\tau_0)|$, which encodes the wind strength in the flat bed, and the vegetation growth rate V_v. In fact, the stabilization process depends on the competition between sand transport and vegetation growth expressed by Eq.(3.7). This competition can be quantified by a dimensionless control parameter θ, which we call fixation index, defined as the ratio between the characteristic erosion rate on the initial barchan dune, which scales as Q to the volume defined characteristic length $V^{1/3}$ ratio (Eq. 3.6), and the vegetation growth rate,

$$\theta \equiv Q/(V^{1/3}V_v)\,. \tag{3.10}$$

After performing simulations for different V, Q and V_v, we find a common fixation index $\theta_c \approx 0.5$ beyond which vegetation fails to complete the inversion of the barchan dune already described in Fig. 3.13. As long as $\theta > \theta_c$ barchan dunes remain mobile, otherwise they are deactivated by plants.

This morphologic transition at θ_c is typified by the evolution of the normalized velocity v/v_0 of vegetated dunes for different initial conditions with v_0 as the initial barchan velocity (illustrative examples are shown in Fig. 3.14). They reveal a general pattern characterized for medium and high fixation indexes by a speedup preceeding a sharp decrease of the dune velocity at $t = t_s$ when inactivation occurs. The explicit condition for inactivation reads $v/v_0 < 0.2$. At $t < t_s$ the barchan evolves toward an active parabolic dune (Fig. 3.13a-d) that becomes inactive for larger times ($t > t_s$) (Fig. 3.13e). However, for fixation index larger than θ_c barchans remain mobile and thus t_s diverges.

Since the dune velocity v is proportional to the inverse of its height (Bagnold, 1941), the sharp speedup in Fig. 3.14 is a consequence of the height decrease due to the redistribution of sand in the elongated dune. This redistribution process is enhanced at high θ when vegetation is progressively weaker against sand erosion. At small fixation indexes however, vegetation overcomes sand deposition and dune movement is determined by the vegetation dying rate on the crest which results in a slower dune motion. In this regime the dune velocity oscillates due to the cyclic mechanism that controls the vegetation growth on the crest. The same mechanism is responsable for the short reactivation of the inactive parabolic dune represented by the occasional second peak in the dune velocity for $t > t_s$ (Fig. 3.14).

From the analysis of the inactivation time t_s as function of V, Q and V_v, we find that t_s scales with a characteristic dune migration time $t_m \equiv V^{2/3}/Q$ and obeys a power law in θ (Fig. 3.14, inset(a))

$$t_s \approx 0.17\, t_m/(\theta_c - \theta)\,, \tag{3.11}$$

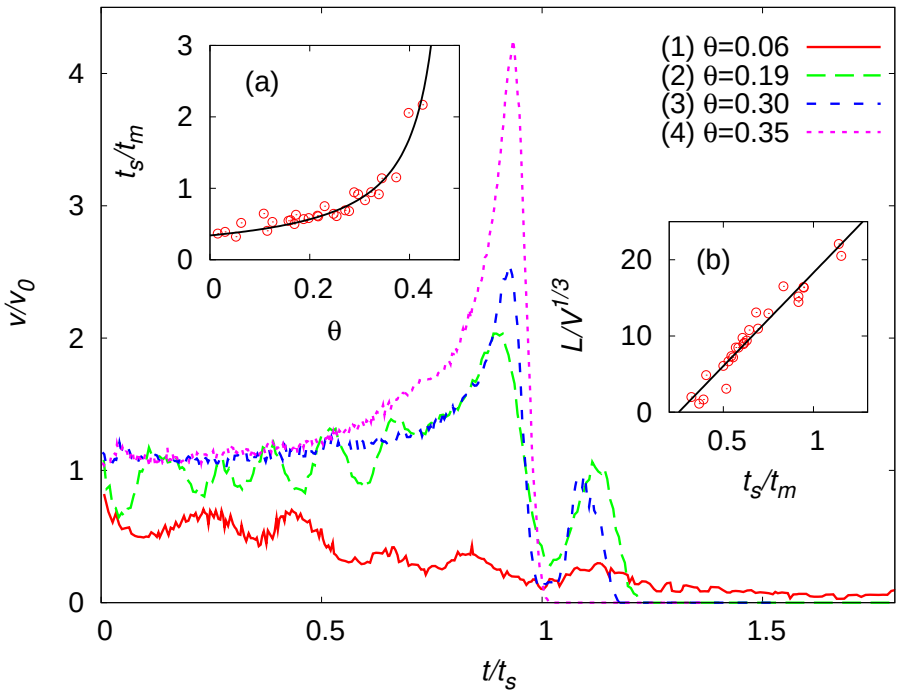

Figure 3.14: Evolution of the normalized dune velocity (v/v_0) for simulations with initial condition given by the parameters V (x10^3 m^3), Q (m^2/yr) and V_v (m/yr): **(1)** 200, 286 and 78, **(2)** 200, 286 and 26, **(3)** 44, 529 and 52, and **(4)** 200, 529 and 26. They represent fixation indexes $\theta = 0.06$, 0.19, 0.30 and 0.35, respectively. Inset (a): the normalized dune inactivation time t_s/t_m diverges when $\theta \to \theta_c$ (solid line). Inset (b): the normalized final parabolic dune length $L/V^{1/3}$ is proportional to t_s/t_m. Symbols indicate simulation results.

which discloses a transition between an inactive parabolic dune and a barchan dune remaining active.

The normalized final length of the parabolic dune $L/V^{1/3}$ also diverges near the transition point. The parabolic length depends linearly on the normalized inactivation time, $L/V^{1/3} \approx a\, t_s/t_m - r$, (Fig. 3.14, inset (b)) where $a \approx 24.5$ and $r \approx 6.2$, and thus scales as $L/V^{1/3} \sim (\theta_c - \theta)^{-1}$. Note that in the limit $\theta = 0$, the inactivation time is still proportional to t_m ($t_s \approx 0.34\, t_m$) and the dune moves a distance $L \approx 2\, V^{1/3}$. This is a consequence of the heterogeneous seeding assumed before. Since plants cannot grow in the dune windward side where erosion occurs, all this sand is stabilized only after crossing the crest. Thus, the dune moves a distance equivalent to its windward side length $\sim 2\, V^{1/3}$.

Figure 3.15 shows some examples of the L dependence on θ. For small θ, barchan dunes are quickly deactivated (Eq.3.11) and short parabolic dunes emerge (Fig. 3.15a). At large θ the amount of sand trapped by plants in the dune arms, which height scales as $V^{2/3}/L \sim V^{1/3}\,(\theta_c - \theta)$, is reduced. This leads to longer parabolic dunes whose 'noses' can experience successive splits before being finally deactivated (Fig. 3.15b and 3.15c).

The dependence of t_s on the properties of the initial barchan through θ and t_m leads us to characterize the mobility or activity of a vegetated dune only based on general field conditions. In particular, the condition $\theta < \theta_c$ for a migrating barchan to become inactive explicitely reads

$$Q < Q_c \equiv \theta_c V_v V^{1/3}, \tag{3.12}$$

which represents a size dependent upper limit for Q below which inactivation takes place, and thus stresses the leading role of the wind strength in the inactivation process. It also defines a minimum vegetation growth velocity $V_{vc} = \theta_c^{-1} Q/V^{1/3}$, also a function on dune size, and a minimum dune volume $V_c = (\theta_c^{-1} Q/V_v)^3$ above which barchan dunes are stabilized. Furthermore, the dune inactivation time as an explicit function of V achieves a

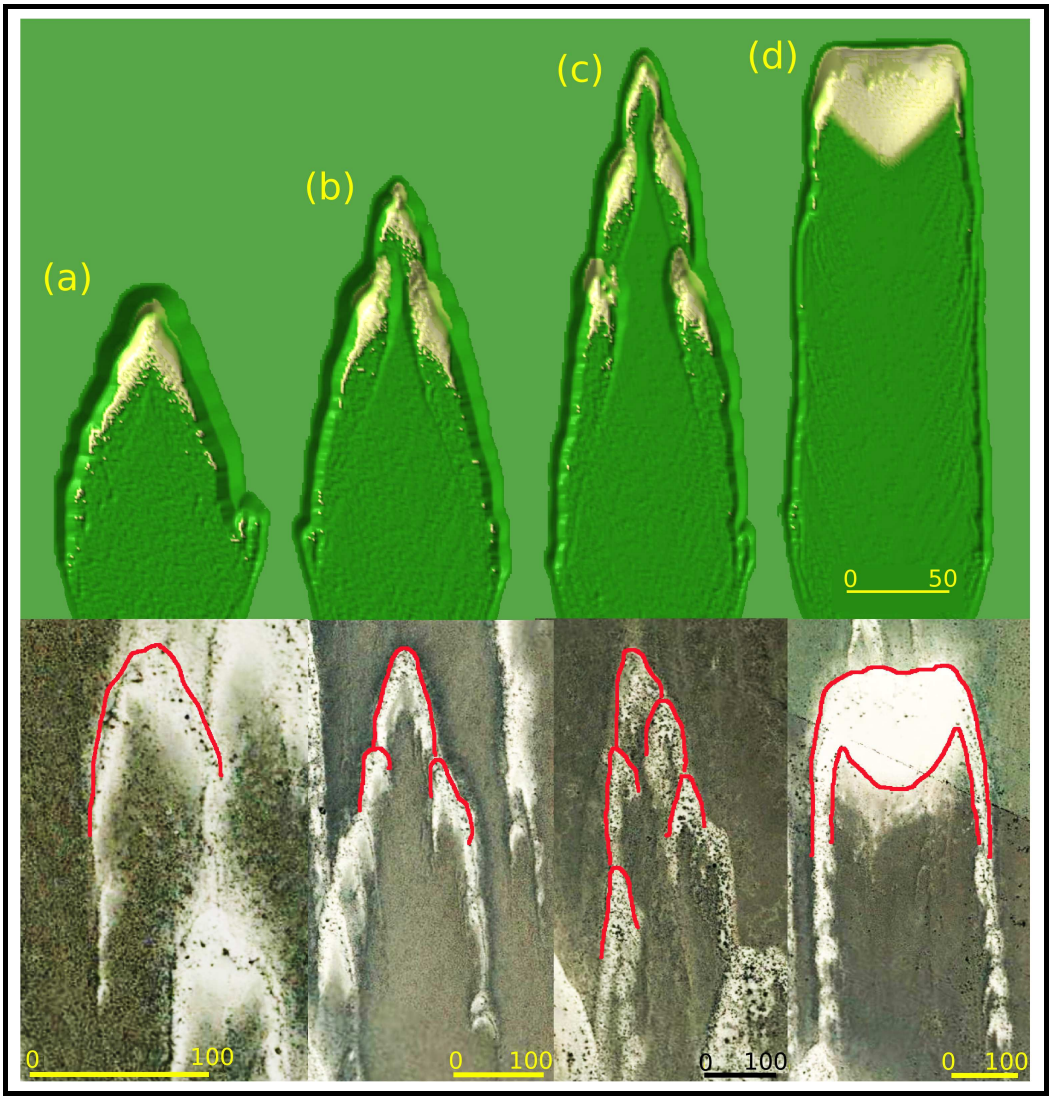

Figure 3.15: Examples of parabolic dune shapes at fixation indexes θ: (a) 0.16, (b) 0.22 and (c) 0.27. (d) is an example of an intermediate state at $\theta = 0.38$ where the dune still is barchan-like, in sharp contrast to the rest. Each figure is compared with real examples from White Sand, New Mexico. Note the similarities in the contour lines market in red. Satellite images taken from GoogleEarth.

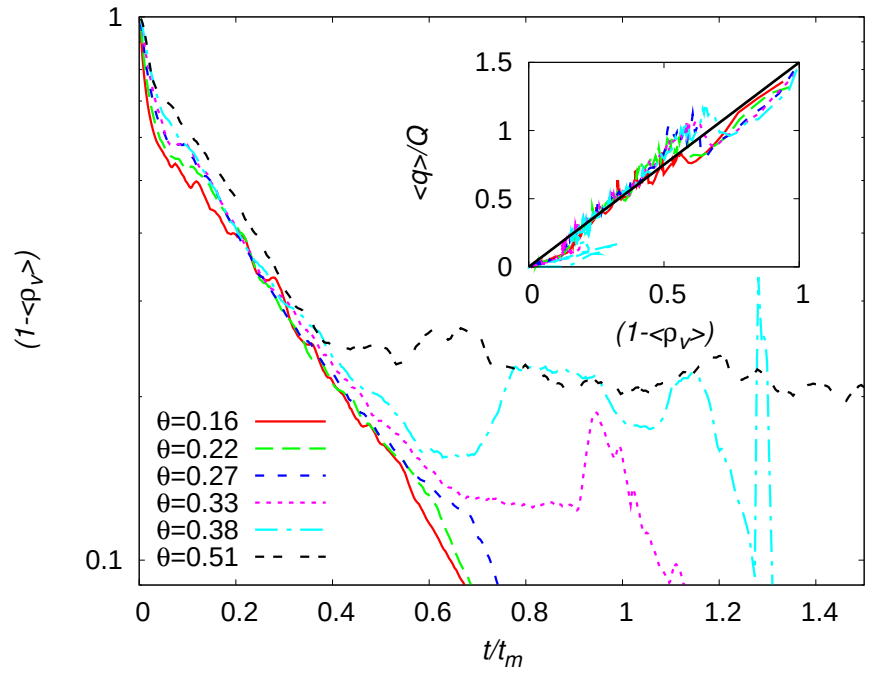

Figure 3.16: The fraction of available sand surface $1 - \langle \rho_v \rangle$, where $\langle \rho_v \rangle$ is the mean vegetation cover density, shows an exponential decay during the evolution of a vegetated barchan dune for small θ when time is normalized by t_m. Inset: proportionality between the mean sand flux $\langle q \rangle$, normalized by the saturated upwind value Q, and the fraction of active sand surface.

minimum for a dune volume $V_0 = (3/2)^3 V_c$. Therefore, dunes with $V < V_c$ will remain mobile, while dunes with volumes $V_0 > V_c$ will be the first to be stabilized. Large dunes however, will remain mobile for a time that scales with $t_m \propto V^{2/3}$.

The dynamics of dune stabilization is also characterized by the evolution of the mean vegetation cover density $\langle \rho_v \rangle$ (Fig. 3.16) and, in a minor way, by the mean sand flux $\langle q \rangle$ over the dune, which we find to be proportional to the fraction of available sand surface $1 - \langle \rho_v \rangle$ (Fig. 3.16, inset). For small θ the evolution follows the same trend, e.g. a rising vegetation cover and the resulting reduction of the mean sand flux (Lancaster and Baas, 1998), with t_m as the characteristic time. For larger θ, the vegetation cover reaches a plateau that extends until the dune stabilizes at $t \approx t_s$, after which vegetation cover rises again due to the inactivation of the dune. This plateau extends indefinitely at $\theta = \theta_c$, when t_s diverges, as a sign of actual sand mobility.

3.2.3 Coastal systems

In chapter 2 we showed how barchan dunes fields can arise from sandy beaches. In fact, the sand deposited by the sea in beaches is one of the main source of sand dunes, which explain the abundance of stabilization attempts in coastal system all around the world.

In order to study, at least qualitatively, the emergence and migration of a dune field from the coast in presence of vegetation, we perform numerical calculation on a plane surface where a constant sand influx was imposed. Concerning vegetation growth, we select a homogeneous seeding in the whole field except a small region around the input boundary, to mimic the absent of plants nearby the sea coats due to extreme salty water.

Figure 3.17 shows snapshots of the simulation results for different vegetation growth rate V_v under a constant sand flux Q. Initially, plants grow forming a barrier in front of the beach, represented by the input boundary $x = 0$, where incoming sand accumulates. Once vegetation start to grow over the sand surface accumulated on the barrier, plants become susceptible of being eroded by the wind and die. Therefore, sand overcomes the plants barrier and penetrates into inland (Fig. 3.17, first snapshot). It is at the inland where the competition between plants and sand mobility really starts. When vegetation growth rate is large enough, as in Fig. 3.17a and 3.17b, sand is not capable of forming sand dunes and just accumulates over the plants to be stabilized again by them. In this case a vegetated sand front slowly penetrates into inland.

For small vegetation growth rate, sand is not immediately deactivated and remains mobile.

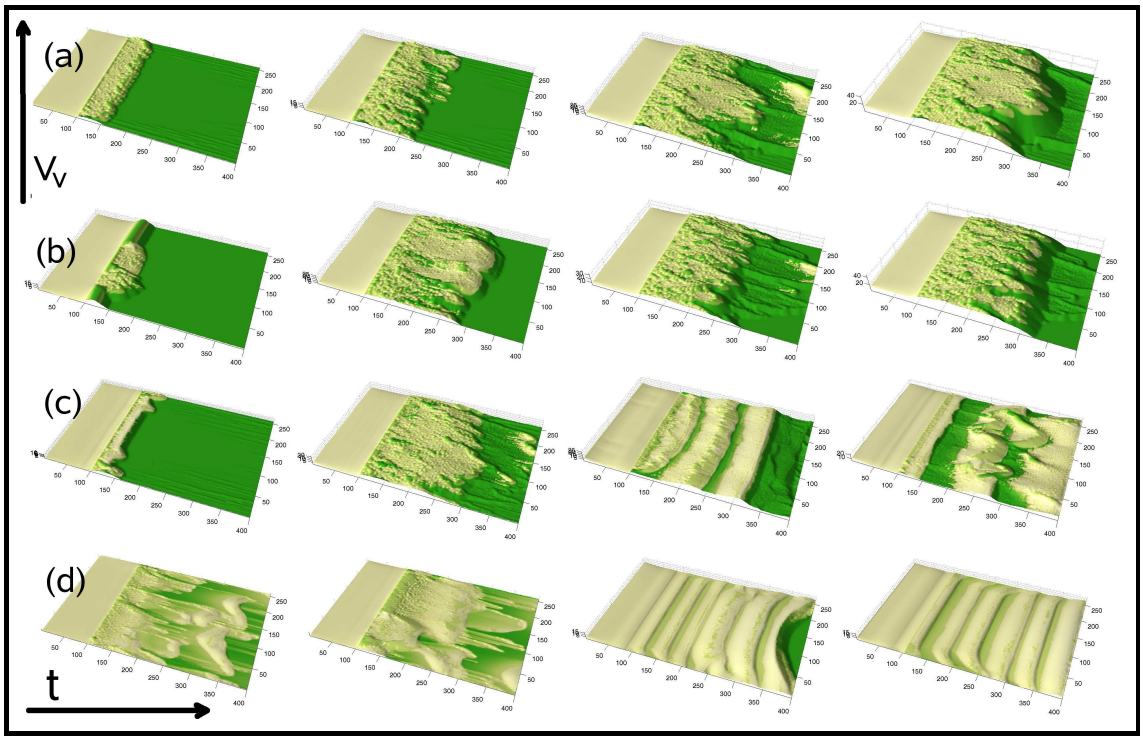

Figure 3.17: Different time evolutions of a sandy coast as a result of the competition between sand mobility and vegetation growth V_v. Green represents vegetation.

In this case, a transversal front of crescent dune, also called transversal dunes, is formed where vegetation is placed on top and in the basins inbetween (Fig. 3.17 c, third snapshot). Afterwards, the transversal front becomes unstable due to the vegetation cover, and it is splitted into barchanoids from which marginal active parabolic dunes clearly emerge (Fig. 3.17 c, last snapshots).

When V_v is even smaller, the transversal front is almost vegetation free and remains stable, although vegetation is still growing in the basins. In this case, sand dunes are not deactivated and remain mobile.

3.3 Conclusions

In this Chapter, we proposed a set of differential equations of motion describing the aeolian transport on vegetated granular surfaces including the growth and destruction of plants. Through them we calculated the morphological transition between active barchans and inactive parabolic dunes characterized by the divergence of the dune inactivation time t_s and its scaling with the barchan migration time t_m. We found that the fixation index θ, a dimensionless combination of barchan dune size, wind strength and vegetation growth velocity, determines from the very beginning the final outcome of the competition between vegetation growth and aeolian surface mobility. These predictions can be directly tested in the field and have implications on the economy of semi-arid regions on coastal management and on global ecosystems.

We have also presented measurements on real parabolic dunes in the coast of Brasil, concerning their shape and the vegetation cover on them. The vegetation cover over a dune was estimated indirectly by the number and size of plants in a characteristic area of the dune. To do so we identify the species of plant present in the dune and counting the number of times they appear in the study area and measure their characteristic length, height and total leaf area. By using the vegetation data we were able to calculate the plant cover density at the particular points on the dunes and compare it with the grayscale of the satellite image. Doing so we found a correlation between both the vegetation cover density and the image grayscale which lead us to estimate the density cover to the whole parabolic dune. In that way we now can compare the empirical vegetation cover data with the result of our simulations to validate the distribution of vegetation over the dune.

Through the procedure here described one can now estimate the degree of inactivation of a vegetated dune and reconstruct the previous dune history.

Conclusions

The results presented in this thesis, as well as the main problems addressed in it, can be divided into three parts: the results at the grain scale, those at the dune field scale and, finally, those comprising the inactivation of sand dunes driven by vegetation.

At the grain scale, we proposed a new equation for the saturated sand flux as a function of wind shear velocity. This is done by introducing a wind profile that includes the feedback effect of grain saltation and an expression for the roughness length including the saltation layer. The sand flux equation was validated using wind tunnel data and also includes, as particular cases, other transport equations depending on the relation between the two characteristic lengths of the model: the focal height of the perturbed wind profile and the height at which the wind drag replaces the momentum lost by the grains in bed collisions (Durán and Herrmann, 2006a).

Further, for the first time, the phenomenological parameters of the sand transport model were determined using scaling relations with the fluid density and viscosity, the gravity acceleration and the grain diameter, some of which were validated using wind tunnel measurements (Durán and Herrmann, 2006a). As was pointed out in the Introduction, these dependences are crucial for modeling of dunes in different physical conditions, like in the Mars atmosphere, or inside water or simply to study the effect of the grain diameter on the dune morphology. For instance, we successfully applied this model to the scaling problem of Marcian dunes (Parteli et al., 2006).

As a consequence of the linear scaling between their outflux and influx, the barchan dunes are intrinsically unstable and increase or decrease in volume depending only on their influx. Therefore, it is concluded that the dynamics at the dune field scale is central for the evolution of a single barchan dune.

At dune field scale, by measuring dune sizes and inter-dune spacings in real dune fields, we found that dune sizes follow lognormal distribution and inter-dune spacing is uniform along the field. The lognormality in the size distribution implies an underlying multiplicative process in the evolution of the dune sizes, while the uniform dune spacing gives insight into the spatial distribution of that process. In fact, for other dune fields, like static dune fields (e.g. longitudinal or star dune fields) larger dunes are surrounded by larger empty space, and thus, the inter-dune spacing scales with the dune size. The difference of the inter-dune spacing observed in these fields and in barchan ones is a consequence of the way sand is redistributed among the dunes. In static dune fields, since the dunes are on the average static, they change their size only by flux balance. Therefore, from mass conservation, a dune grows only if its neighboring dunes shrink. In barchan dune

fields, where dunes are mobile, the uniform inter-dune spacing is a clear sign of a richer internal dynamics where collisions play an important role. Consequently, small dunes are continuously emerging from larger ones, destroying any simple correlation between dune size and inter-dune distance, leading to a spatial uniformity. Furthermore, dune collisions are also important in the dune size selection. Statistically, they act over dune sizes as an additive random process that leads to gaussian size distributions (Durán et al., 2006a). When collisions are complemented with the flux balance in a dune field, a competition between these two processes arises, because the first process redistributes sand while the second accumulates it. This interaction acts as a multiplicative process in the evolution of barchan dune sizes accounting for the lognormal size distributions.

Through the competition between collisions and flux balance we also uncovered a crucial relation between the parameters of the size and the spatial distribution of the dunes. Following the dynamics of dune collisions in an analytical 'mean-field' approach, we found that the relative inter-dune spacing, i.e., the inter-dune spacing divided by the dune mean size, increases with the cube of the relative standard deviation of the lognormal distribution. Since the relative inter-dune spacing also determines the dune density in the field, the relative deviation of the size distribution in barchan dune fields is fully determined by the dune density, explaining why a sparse dune field also has a broad size distribution.

We also answered the question about the physical origin of the mean and deviation of the size distribution, as well as the inter-dune spacing. From our dune field simulations with a 'coarse-grain' model, we found that the statistical properties of the dune field only depend on the conditions at the incoming field boundary, i.e. the density and the size of the incoming dunes. The density of dunes in the field increases with the density of incoming dunes, showing a critical density that the incoming dunes must overcome to generate a dune field. When the incoming dunes are very sparse they will just be dispersed by the wind and no dune field will emerge. In turn, the mean dune size in the field is determined by both, the size and the density of the incoming dunes. Here, we also found a threshold size that is proportional to the density of the incoming dunes and determines how the mean dune size relates to the incoming dune size. When the incoming dunes have a size below this threshold, they will increase in average their size during the evolution of the field, and when the incoming dune size is above this threshold, the dunes entering into the field will in average shrink (Durán et al., 2006b).

Concerning the role of **vegetation growth against sand mobility**, we have proposed a set of differential equations of motion describing the aeolian transport on vegetated granular surfaces including the growth and destruction of plants. Through them we calculated the morphological transition between active barchans and inactive parabolic dunes, a process that describes the dune inactivation. The model is further validated by comparing the simulated parabolic dunes with the real ones on the coast of Brazil, finding crucial similarities in the morphology of the dune, the places where vegetation grows and the spatial distribution of the available sand surface.

The inactivation of barchan dunes is characterized by an order parameter named fixation index θ. It is a dimensionless combination of the barchan dune size, the wind strength and the vegetation growth velocity. Further, we showed that, when the fixation index approaches a critical value θ_c, the duration of dune inactivation diverges as $(\theta_c - \theta)^{-1}$.

Therefore, for a fixation index less than the critical value, active dunes will be deactivated by vegetation growth within a finite time. Otherwise, they will overcome the vegetation cover by remaining active. The fixation index θ only depends on the general conditions at which vegetated dunes evolve and not on the time evolution itself. Therefore it determines the final outcome of the competition between vegetation growth and aeolian surface mobility (Durán and Herrmann, 2006b).

We also found that the distance travelled by the dune during the inactivation period also diverges with the fixation index. This distance can be understood as a penetration depth into the coast for coastal dunes and thus can provide a good estimation of the area affected by dune motion during the inactivation process.

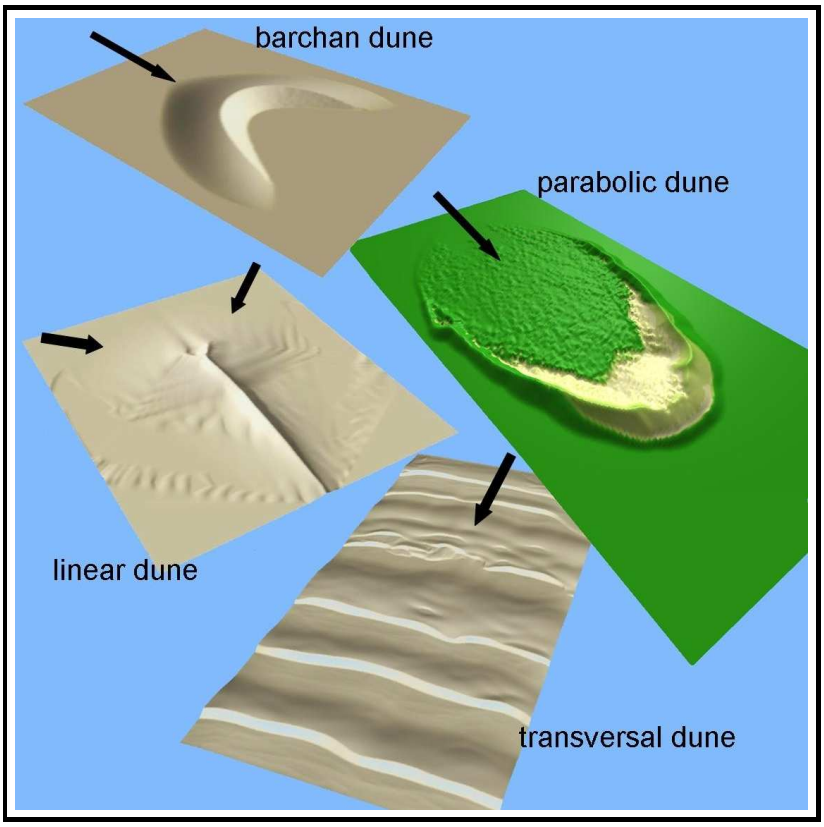

Figure 3.18: Examples of different simulated sand dune shapes including the wind arrows.

Outlook

In this thesis we improved upon an existing dune model to go beyond the study of isolated barchan dunes to the complex cooperative dynamics in dune fields and their interaction with vegetation. However, as always in science, new answers raise new questions, pushing our knowledge further.

For instance, we have explained the dune size and spacing selection mechanisms in dune fields in terms of the incoming dunes at the boundary, but the processes that govern the

conditions at the boundary are still unknown. It is important to note that the barchan dune fields only account for less than 20 % of total sand seas. The rest are mainly transversal dune, longitudinal dune and star dune fields. Although the DUNE model used gives a fairly realistic description of the main dune types (Fig. 3.18), there exists no model for their behavior in dune fields and, more important, detailed model for the complex superposition of different dune patterns commonly found in real situations also has not been developed so far.

The general conditions under which a typical dune pattern emerges depends on the wind velocity which fluctuates both in direction and strength. However, a complete description bridging dune patterns and wind regimes is still lacking. Under which conditions are these patterns stable? Is there a sort of competition between different dune patterns in the selection process? Recently these questions were put in the general framework of non-linear dynamics (Baas, 2002). Sand surface under wind energy becomes a self-organized system where selected dune patterns emerge at different scales. This raises more questions concerning the phase space of such systems and the underlying dynamical transitions.

Further questions arise in coastal geomorphology, where it is known that vegetation plays a very important role as an agent that controls dune morphology. We already uncovered the detailed mechanism by which vegetation reshapes a barchan dune landscape. However, an experimental verification of the predictions of our model, as well as a test for the reliability of the fixation index introduced are important and needs to be done. The model also needs to be generalized to include more complex situations like the influence of new kind of plants, the water table, and the seasonal changes on the wind blow and vegetation growth rates.

The ultimate goal in coastal management concerns the long term predictions of coastal geomorphology. How can we estimate the degree of inactivation of a coastal dune and reconstruct the previous and future dune history? Our work provides a new direction and methodology to address these important issues and will inspire further research in this important field.

Bibliography

Almeida, M., Andrade, J., and Herrmann, H. (2006). Aeolian transport layer. *Phys. Rev. Lett.*, 96:018001.

Anderson, R. S. (1991). Wind modification and bed response during saltation of sand in air. *Acta Mechanica (Suppl.)*, 1:21–51.

Anderson, R. S. and Haff, P. K. (1988). Simulation of eolian saltation. *Science*, 241:820.

Andreotti, B. (2004). A two-species model of aeolian sand transport. *J. Fluid Mech.*, 510:47–70.

Andreotti, B., Claudin, P., and Douady, S. (2002a). Selection of dune shapes and velocities part 1: Dynamics of sand, wind and barchans. *Eur. Phys. J. B*, 28:321–339.

Andreotti, B., Claudin, P., and Douady, S. (2002b). Selection of dune shapes and velocities; part 2:a two-dimensional modelling. *Eur. Phys. J. B*, 28:315–319.

Anthonsen, K., Clemmensen, L., and Jensen, J. H. (1996). Evolution of a dune from crescentic to parabolic from in response to a short-term climatic changes-rabjergmile, skagen-odde, denmark. *Geomorphology*, 17:63–77.

Ash, J. E. and Wasson, R. (1983). Vegetation and sand mobility in the australian desert dunefield. *Zeitschrift für Geomorphologie N.F., Supplementbande*, 45:7–25.

Baas, A. C. W. (2002). Chaos, fractals and self-organization in coastal geomorphology: simulating dune landscapes in vegetated environments. *Geomorphology*, 48:309–328.

Bagnold, R. A. (1941). *The physics of blown sand and desert dunes.* Methuen, London.

Besler, H. (1992). *Geomorphology der ariden Gebiete*. Wiss. Buchges., Darmstadt.

Besler, H. (1997). Eine Wanderdüne als Soliton? *Physikalische Bläetter.*, 10:983.

Besler, H. (2002). Complex barchans in the libyan desert: dune traps or overtaking solitons? *Zeitschrift für Geomorphologie N.F.*, 126:59–74.

Bouchaud, J. P. (1998). A phenomenological model for avalanches and surface flows. In H. J. Herrmann, J-P Hovi, and S. Luding, editor, *Physics of dry granular media*. NATO-ASI Series, Kluwer academic publishers, Dordrecht.

Bouchaud, J. P., Cates, M. E., Ravi Prakash, J., and Edwards, S. F. (1994). Hysteresis and metastability in a continuum sandpile model. *J. Phys. France I*, 4:1383.

Bowers, J. (1982). The plant ecology of inland dunes in western north-america. *Journal of Arid Environments*, 5:199–220.

Brookfield, T. S. and Ahlbrandt, M. E. (1983). *Eolian Sediments and Processes*. Elsevier, Amsterdam.

Chepil, W. S. (1958). The use of evenly spaced hemispheres to evaluate aerodynamic forces on a soil surface. *Trans. Am. Geophys. Union*, 39(397–403).

Coursin, A. (1964). Observations et expériences faites en avril et mai 1956 sur les barkhans du Souehel el Abiodh (région est de Port-Étienne). *Bulletin de l' I. F. A. N.*, 22A, no. 3:989–1022.

Danin, A. (1978). Plant species diversity and plant succession in a sandy area in northern negev. *Flora*, 167:409–422.

Danin, A. (1987). Impact of man on biological components of desert ecosystems in israel. In *Proceedings of the Annual Meeting of the Israeli Botany Society, Beer Sheva*, pages 6–7.

Danin, A. (1991). Plant adaptation in desert dunes. *Journal of of Arid Environments*, 21:193–212.

Durán, O. and Herrmann, H. J. (2006a). Modelling of saturated sand flux. *J. Stat. Mech.*, page P07011.

Durán, O. and Herrmann, H. J. (2006b). Vegetation against dune mobility. *Phys. Rev. Lett.*, 97:188001.

Duran, O., Schwämmle, V., and Herrmann, H. (2005). Breeding and solitary wave behavior of dunes. *Phys. Rev. E*, 72:021308.

Durán, O., Schwämmle, V., and Herrmann, H. J. (2006a). Barchan dune's size distribution induced by collisions. *submitted to Geophys. Res. Lett.*

Durán, O., Schwämmle, V., Lind, P. G., and Herrmann, H. J. (2006b). A closed description of barchan dune fields. *submitted to Phys. Rev. Lett.*

Elbelrhiti, H. Andreotti, B. and Claudin, P. (2006). Barchan dune corridors: field characterization and investigation of control parameters. *cond-mat/0609120*. submitted to Geomorphology.

Elbelrhiti, H., Claudin, P., and Andreotti, B. (2005). Field evidence for surface-wave induced instability of sand dunes. *Nature*, 437:04058.

Endo, N. and Taniguchi, K. (2004). Obsevation of the whole process of interaction between barchans by flume experiments. *Geophysical Research Letters*, 34:L12503.

Finkel, H. J. (1959). The barchans of southern Peru. *Journal of Geology*, 67:614–647.

Fisher, P. F. and Galdies, P. (1988). A computer model for barchan-dune movement. *Computer and Geosciences*, 14-2:229–253.

Friedman, G. M. and Sanders, J. E. (1978). *Principles of sedimentology*. Wiley, New York.

Fryberger, S. G. (1979). Dune forms and wind regime. In McKee, E., editor, *A study of global sand seas. U.S. Geological Survey, Professional Paper*, pages 137–169.

Gilad, E., von Hardenberg, J., Provenzale, A., Shachak, M., and Meron, E. (2004). Ecosystem engineers: From pattern formation to habitat creation. *Phys. Rev. Lett.*, 93:098105.

Hack, J. T. (1941). Dunes of the western navajo country. *Geographical Review*, 31:240–263.

Hastenrath, S. (1967). The barchans of the Arequipa region, southern Peru. *Zeitschrift für Geomorphologie*, 11:300–331.

Hastenrath, S. (1987). The barchan dunes of southern Peru revisited. *Zeitschrift für Geomorphologie*, 31-2:167–178.

Hersen, P. (2004). On the crescentic shape of barchan dune. *Eur. Phys. J. B*, 37:507–514.

Hersen, P. (2005). Flow effects on the morphology and dynamics of aeolian and subaqueous barchan dunes. *J. Geophys. Res.*, 110:F04S07.

Hersen, P., Andersen, K., Elbelrhiti, H., Andreotti, B., Claudin, P., and Douady, S. (2004). Corridors of barchan dunes: stability and size selection. *Phys. Rev. E*, 69:011304.

Hersen, P. and Douady, S. (2005). Collision of barchan dunes as a mechanism of size regulation. *Geophys. Res. Lett.*, 32:L21403.

Hersen, P., Douady, S., and Andreotti, B. (2002). Relevant lengthscale of barchan dunes. *Phys. Rev. Lett.*, 89:264301.

Hesp, P. (1991). Ecological process and plant adaptations on coastal dunes. *Journal of Arid Environments*, 21:165–191.

Hesp, P. (1996). Flow dynamics in a trough blowout. *Boundary-Layer Meteorology*, 77:305–330.

Hesp, P. A. and Hastings, K. (1998). Width, height and slope relationships and aerodynamic maintenance of barchans. *Geomorphology*, 22:193–204.

Howard, A. D. and Morton, J. B. (1978). Sand transport model of barchan dune equilibrium. *Sedimentology*, 25:307–338.

Hunt, J. C. R., Leibovich, S., and Richards, K. J. (1988). Turbulent wind flow over smooth hills. *qjrms*, 114:1435–1470.

Iversen, J. D. and Rasmussen, K. R. (1999). The effect of wind speed and bed slope on the sand transport. *Sedimentology*, 46:723–731.

Jackson, P. S. and Hunt, J. C. R. (1975). Turbulent wind flow over a low hill. *qjrms*, 101:929.

Jäkel, D. (1980). Die Bildung von Barchanen in Faya-Largeau/Rep. du Tchad. *Zeitschrift für Geomorphologie N.F.*, 24:141–159.

Jimenez, J. A. and Madsen, O. S. (2003). A simple formula to estimate settling velocity of natural sediments. *J. Waterway, Port, Coastal Ocean Eng.*, 129:70–78.

Jimenez, J. A., Maia, L. P., Serra, J., and Morais, J. (1999). Aeolian dune migration along the Ceará coast, north–eastern brazil. *Sedimentology*, 46:689–701.

Katsuki, A., Nishimori, H., Endo, N., and Taniguchi, K. (2005). Collision dynamics of two barchan dunes simulated by a simple model. *J. Phys. Soc. Jpn*, 74:538.

Kawamura, R. (1951). Study of sand movement by wind. *Phys. Sci. Res. Inst. of Tokyo University*, 5:92–112.

Kind, R. J. (1976). A critical examination of the requirements for model simulation of wind-induced erosion/deposition phenomena such as snow drifting. *Atmos. Environ.*, 10:219–227.

Kocurek, G. (1996). Desert aeolian systems. In Reading, H. G., editor, *Sedimentary Environments: Processes, Facies and Stratigraphy*, pages 125–153, Oxford. Blackwell Science Ltd. 3rd Edition.

Kroy, K., Sauermann, G., and Herrmann, H. J. (2002). Minimal model for sand dunes. *Phys. Rev. L.*, 68:54301.

Lamb, G. L. (1980). *Elements of Soliton Theory*. Wiley.

Lancaster, N. (1988). Development of linear dunes in the southwestern kalahari, southern africa. *Journal of Arid Environments*, 14:233–244.

Lancaster, N. (1995). *Geomorphology of desert dunes*. Routledge, London.

Lancaster, N. and Baas, A. (1998). Influence of vegetation cover on sand transport by wind: Field studies at owens lake, california. *Earth Surf. Proc. and Landforms*, 23:69–82.

Lettau, K. and Lettau, H. (1969). Bulk transport of sand by the barchans of the Pampa de La Joya in southern Peru. *Zeitschrift für Geomorphologie N.F.*, 13-2:182–195.

Lettau, K. and Lettau, H. (1978). Experimental and micrometeorological field studies of dune migration. In Lettau, H. H. and Lettau, K., editors, *Exploring the world's driest climate*, pages 110–147. Madison, Center for Climatic Research, Univ. Wisconsin.

Lima, A. R., Sauermann, G., Kroy, K., and Herrmann, H. J. (2002). A model for dune fields. *Physica A*, 310:487–500.

Livingstone, I., Wiggs, G., and Baddock, M. (2005). Barchan dunes: why they cannot be treated as 'solitons' or 'solitary waves'. *Earth Surf. Process. Landforms*, 30:255–257.

McEwan, I. K. and Willetts, B. B. (1991). Numerical model of the saltation cloud. *Acta Mechanica (Suppl.)*, 1:53–66.

McEwan, I. K. and Willetts, B. B. (1994). On the prediction of bed-load sand transport rate in air. *Sedimentology*, 41:1241–1251.

Momiji, H. and Warren, A. (2000). Relations of sand trapping efficiency and migration speed of transverse dunes to wind velocity. *Earth Surface Processes and Landforms*, 25:1069–1084.

Muckersie, C. and Shepherd, M. J. (1995). Dune phases as time-transgressive phenomena, manawatu, new zealand. *Quaternary International*, 26:61–67.

Nalpanis, P., Hunt, J. C. R., and Barrett, C. F. (1993). Saltating particles over flat beds. 251:661–685.

Nickling, W. G. (1986). *Aeolian Geomorphology*. Allen and Unwin, London.

Nishimori, H., Yamasaki, M., and Andersen, K. H. (1999). A simple model for the various pattern dynamics of dunes. *Int. J. of Modern Physics B*, 12:257–272.

Oulehri, T. (1992). *Etude géodynamique des migrations de sables éoliens dans la région de Laâyoune (Nord du Sahara marocain)*. PhD thesis, l'Universite Paris 6, Paris. no. 92-12.

Owen, P. R. (1964). Saltation of uniformed sand grains in air. *J. Fluid. Mech.*, 20:225–242.

Parteli, E. R., Durán, O., and Herrmann, H. J. (2006). The minimal size of barchan dunes. *accepted in Phys. Rev. E*.

Peixoto, G. L. and Oort, A. H. (1992). *Physics of Climate*. Springer.

Pye, K. (1982). Morphological development of coastal dunes in a humid tropical environment, cape bedford and cape flattery, north queensland. *Geografiska Annaler*, 64A:213–227.

Pye, K. and Tsoar, H. (1990). *Aeolian sand and sand dunes*. Unwin Hyman, London.

R., G. D. and D., S. L. (1994). Eolian-climatic threshold and sand dunes at the handford site, south-central washington, usa. *Journal of Arid Environments*, 28:95–116.

Rasmussen, K. R. Iversen, J. D. and Rautahemio, P. (1996). Saltation and wind flow interaction in a variable slope wind tunnel. *Geomorphology*, 17:19–28.

Rasmussen, K. R. and Sørensen, M. (2005). Saltation and wind flow interaction in a variable slope wind tunnel. In *Proceedings of Powders and Grains*, pages 967–971.

Raupach, M. R. (1992). Drag and drag partition on rough surfaces. *Boundary-Layer Meteorology*, 60:375–395.

Raupach, M. R., Gillette, D. A., and Leys, J. F. (1993). The effect of roughness elements on wind erosion threshold. *Journal of Geophysical Research*, 98:3023–3029.

Richards, F. J. (1959). A flexible growth function for empirical use. *Journal of Experimental Botany*, 10:290–300.

Rioual, F., Valance, A., and Bideau, D. (2000). Experimental study of the collision process of a grain on a two–dimensional granular bed. *Phys. Rev. E*, 62:2450–2459.

Sauermann, G. (2001). *Modeling of Wind Blown Sand and Desert Dunes*. PhD thesis, University of Stuttgart.

Sauermann, G., Andrade, J. S., Maia, L., Costa, U., Araújo, A., and Herrmann, H. J. (2003). Wind velocity and sand transport on a barchan dune. *Geomorphology*, 1325:1–11.

Sauermann, G., Kroy, K., and Herrmann, H. J. (2001). A continuum saltation model for sand dunes. *Phys. Rev. E*, 64:31305.

Sauermann, G., Rognon, P., Poliakov, A., and Herrmann, H. J. (2000). The shape of the barchan dunes of southern Morocco. *Geomorphology*, 36:47–62.

Schwämmle, V. and Herrmann, H. (2003). Solitary wave behaviour of dunes. *Nature*, 426:619.

Schwämmle, V. and Herrmann, H. (2005a). A model of barchan dunes including lateral shear stress. *Eur. Phys. J. E*, 16:57–65.

Schwämmle, V. and Herrmann, H. (2005b). Reply to the discussion on 'barchan dunes: why they cannot be treated as "solitons" or "solitary waves"'. *Earth Surf. Process. Landforms*, 30:517.

Shields, A. (1936). Applications of similarity principles and turbulence research to bed–load movement. Technical Report Publ. No. 167, California Inst. Technol. Hydrodynamics Lab. Translation of: Mitteilungen der preussischen Versuchsanstalt für Wasserbau und Schiffsbau. W. P. Ott and J. C. van Wehelen (translators).

Slattery, M. C. (1990). Barchan migration on the Kuiseb river delta, Namibia. *South African Geographical Journal*, 72:5–10.

Sørensen, M. (1991). An analytic model of wind-blown sand transport. *Acta Mechanica (Suppl.)*, 1:67–81.

Sørensen, M. (2004). On the rate of aeolian sand transport. *Geomorphology*, 59:53–62.

Stam, J. M. T. (1997). On the modelling of two-dimensional aeolian dunes. *Sedimentology*, 44:127–141.

Tsoar, H. (1990). The ecological background, deterioration and reclamation of desert dune sand. *Agriculture, Ecosystems and Environment*, 33:147–170.

Tsoar, H. (2005). Sand dunes mobility and stability in relation to climate. *Physica A*, 357:50–56.

Tsoar, H. and Blumberg, D. G. (2002). Formation of parabolic dunes from barchan and transverse dunes along israel's mediterranean coast. *Earth Surface Processes and Landforms*, 27:1147–1161.

Ungar, J. E. and Haff, P. K. (1987). Steady state saltation in air. *Sedimentology*, 34:289–299.

van Boxel, J. H., Arens, S. M., and van Dijk, P. M. (1999). Aeolian processes across transverse dunes i: Modelling the air flow. *Earth Surf. Process. Landforms*, 24:255–270.

van Dijk, P. M., Arens, S. M., and van Boxel, J. H. (1999). Aeolian processes across transverse dunes ii: Modelling the sediment transport and profile development. *Earth Surf. Process. Landforms*, 24:319–333.

von Hardenberg, J., Meron, E., Shachak, M., and Zarmi, Y. (2001). Diversity of vegetation patterns and desertification. *Phys. Rev. Lett.*, 87:198101.

Wasson, R. J. and Hyde, R. (1983). Factors determining desert dune types. *Nature*, 304:337–339.

Weng, W. S., Hunt, J. C. R., Carruthers, D. J., Warren, A., Wiggs, G. F. S., Livingstone, I., and Castro, I. (1991). Air flow and sand transport over sand–dunes. *Acta Mechanica (Suppl.)*, 2:1–22.

Werner, B. T. (1990). A steady-state model of wind blown sand transport. *J. Geol.*, 98:1–17.

White, B. R. (1979). Soil transport by winds on mars. *J. Geophys. Res.*, 84:4643–4651.

Wilson, I. (1972). Aeolian bedforms–their development an origins. *Sedimentology*, 19:173–210.

Wippermann, F. K. and Gross, G. (1986). The wind-induced shaping and migration of an isolated dune: A numerical experiment. *Boundary Layer Meteorology*, 36:319–334.

Wyatt, V. E. and Nickling, W. G. (1997). Drag and shear stress partitioning in sparce desert creosote communities. *Canadian Journal of Earth Sciences*, **34:1486–1498.**

Zeman, O. and Jensen, N. O. (1988). Progress report on modeling permanent form sand dunes. *Risø National Laboratory*, M-2738.

Zingg, A. W. (1953). Wind tunnel studies of the movement of sedimentary material. In *5th Hydraulic Conference Bull*, volume 34, pages 111–134.

Zobeck, T. M. and Fryrear, D. W. (1986). Chemical and physical characteristics of windblown sediments ii: Chemical characteristics and total soil and nutrient discharge. *Trnas. Am. Soc. Agri. Eng.*, 29:1037–1041.

Acknowledgment

First, I would like to thank Prof. Dr. Hans Herrmann who gave me the opportunity to work at the ICP, and who offered me such an interesting subject.

Next, I am indebted to Prof. Dr. M. Fähnle who accepted to referee this thesis.

I want to express my gratitude to P. Lind for many usefull discussions and stimulation, to V. Schwämmle, V. Schatz and E. Parteli for valuable remarks and support, and Dr. B. Biswal for the critical reading of the manuscript.

Finally, I thank all members of ICP, Stuttgart, who indirectly supported this work by an excellent working atmosphere, system administration, and a programming library.